Growth and characterization of antimony-based Quantum Dots in GaP matrix for nanomemories

vorgelegt von

M. Sc. Physik

Elisa Maddalena Sala

geb. in Bergamo

Von der Fakultät II - Mathematik und Naturwissenschaften
der Technischen Universität Berlin
zur Erlangung des akademischen Grades

Doktor der Naturwissenschaften
Dr. rer. nat.

genehmigte Dissertation

Promotionsausschuss:

Vorsitzender:	Prof. Dr. rer. nat. Holger Stark
Berichter/ Gutachter:	Prof. Dr. phil. nat. Dieter Bimberg
Berichter/ Gutachter:	Prof. Dr. rer. nat. Xavier Wallart

Tag der wissenschaftlichen Aussprache: 17. Mai 2018

Berlin 2018

"In the realm of ideas, everything depends on enthusiasm... in the real world all rests on perseverance."

J. W. von Goethe

To my family

Abstract

Self-assembled Quantum Dots (QDs) have recently attracted great attention for enabling a novel type of non-volatile electronic nanomemory, the QD-Flash. Such a memory architecture represents the ultimate memory cell, exhibiting endurance and fast access times ($\sim$ns). To ensure non-volatile operation, the storage time for carriers has to be of the order of 10 years (or longer) at room temperature, which mainly depends on the depth of the localization potential provided by QDs, but also on their capture cross-section. By choosing an appropriate III/V material combination for QDs and matrix, surpassing the non-volatility limit of 10 years is feasible: type-II antimony-based QDs showing hole confinement are very suitable for such application, leading to a higher carrier localization energy and an increased carrier storage capacity for single QD, with respect to type-I heterostructures. Retention times of more than 10 years for holes in InGaSb/AlP/GaP QDs have been predicted, making thus such QDs promising candidates for the QD-Flash.

This work aims to demonstrate the Metalorganic Chemical Vapor Epitaxy (MOVPE) of InGaSb/AlP/GaP QDs and their use as storage units for the future QD-Flash. The storage time of such QDs is improved by one order of magnitude compared to the previous value for $In_{0.5}Ga_{0.5}As$/GaP QDs. InGaSb QDs are embedded in GaP n^+p-diodes, where an additional AlP barrier is employed, and are electrically characterized. A localization energy $E_{loc} = (1.15 \pm 0.02)$ eV for holes captured in QDs is measured by using the Deep-Level Transient Spectroscopy (DLTS) technique.

This work investigates growth strategies in order to tune the QD structural and optical properties for maximum hole retention times in QDs. A growth interruption (GRI) after deposition of InGaSb and an Sb-flush prior to the QD growth are found to be very effective. By using an Sb-flush, the surface diffusion is controlled leading to more homogeneous QDs and to reduction of defect formation. Taking advantage of a ripening process during GRI, the QD size is increased and the luminescence remarkably improved. The use of antimony in QD growth is found to decrease the associated QD capture cross-section by one order of magnitude with respect to the one of $In_{0.5}Ga_{0.5}As$/GaP QDs/GaP QDs, i.e. from $(8 \pm 5)\cdot10^{-10}$ to $(9 \pm 5)\cdot10^{-11}$ cm^2. This is the first time that engineering of the QD capture cross-section has been utilized to increase hole retention times in QDs. It leads to a hole storage time of almost 1 hour at room temperature, which is to date the record for MOVPE-grown QDs. Such material combination for QDs and matrix represents therefore an excellent candidate for the future QD-Flash.

Kurzfassung

Selbst-organisierte Quantenpunkte (QPe) haben zuletzt wegen einer neuen Art von nicht flüchtigen Speichern, dem QD-Flash, großes Interesse geweckt. Diese Speicherarchitektur entspricht einer ultimativen Speicherzelle, die gute Speicherzeit und schnelle Zugriffszeit aufweist. Für nicht flüchtige Arbeitsweise muss die Speicherzeit bei Raumtemperatur in der Größenordnung von 10 Jahren und länger liegen, was hauptsächlich von der Tiefe des Lokalisierungspotentials aber auch vom Einfangsquerschnitt der QPe abhängt. Durch Wahl einer geeigneten Materialkombination für Quantenpunkte und Matrix ist es möglich, die Grenze für nicht flüchtiges Speichern zu überschreiten. Typ-II Antimon-basierte Quantenpunkte, die Lokalisierung von Löchern aufweisen, sind die besten Kandidaten für dieses neuartige Speicherkonzept. Das hat den Vorteil, dass die Lokalisierungsenergie pro QP größer ist als in Typ-I Heterostrukturen. Speicherzeiten von mehr als 10 Jahren für Löcher in InGaSb/AlP/GaP QPen wurden bereits vorhergesagt und daher sind diese QPe vielversprechend für den QD-Flash.

Diese Arbeit demonstriert erstmals Metallorganische Gasphasenepitaxie (MOVPE) von InGaSb/AlP/GaP QPen und deren Anwendung als Speichereinheiten für den zukünftigen QD-Flash Speicher. Die Speicherzeit dieser QPen wurde um 1 Größenordnung im Vergleich zu der von $In_{0.5}Ga_{0.5}As$/GaP QPen erhöht. InGaSb QPe wurden in n^+p-Dioden eingebettet, wobei eine zusätzliche AlP Barriere benutzt wurde, und elektrisch charakterisiert. Eine Lokalisierungsenergie $E_{loc} = (1.15 \pm 0.02)$ eV für Löcher wurde mittels Deep-Level Transient Spectroscopy (DLTS) gemessen.

Diese Arbeit untersucht Wachstumsstrategien, um die strukturellen und optische Eigenschaften der QPe zu verändern und die Löcherlokalisierung zu maximieren. Eine Wachstumsunterbrechung (Engl. growth interruption, GRI) nach der InGaSb-Abscheidung und ein Sb-flush vor QP-Wachstum sind sehr effektiv. Der Sb-flush vermindert die Oberflächendiffusion, wobei die QPe homogener werden und die Defektbildung unterdrückt wird. Die Anwendung der GRI führt zu einer Vergrößerung der QP-Größe, und zu einer beträchtlichen Verbesserung der QP-Lumineszenz. Der Einsatz von Antimon während des QP-Wachstums verkleinert den Einfangsquerschnitt um eine Größenordnung, im Vergleich zu der von $In_{0.5}Ga_{0.5}As$/GaP QPen QPen, d.h. von $(8 \pm 5)\cdot10^{-10}$ cm^2 auf $(9 \pm 5)\cdot10^{-11}$ cm^2. Dadurch wird die gemessene Speicherzeit der InGaSb/AlP/GaP QPe auf 1 Stunde bei Raumtemperatur erhöht, was derzeit der Rekordwert von MOVPE-QPen ist. Dieses Materialsystem ist daher ein exzellenter Kandidat für den zukünftige QD-Flash. Dies ist das erste Mal, das eine Änderung des Einfangsquerschnitts angewendet wurde, um die Speicherzeit der QPe zu erhöhen.

Parts of this work have been published in

- E. M. Sala, G. Stracke, S. Selve, T. Niermann, M. Lehmann, S. Schlichting, F. Nippert, G. Callsen, A. Strittmatter, and D. Bimberg, *Growth and structure of $In_{0.5}Ga_{0.5}Sb$ quantum dots on GaP(001)*, Appl. Phys. Lett. **109**, 102102 (2016).

  https://aip.scitation.org/doi/full/10.1063/1.4962273

Additionally, the following manuscript has been submitted for publication:

- E. M. Sala, F. Arikan, L. Bonato, F. Bertram, P. Veit, J. Christen, A. Strittmatter and D. Bimberg, *MOVPE growth of (In,Ga)Sb/AlP/GaP(001) quantum dots for nanoscale memory applications.*

Associated publications

- L. Bonato, E. M. Sala, G. Stracke, T. Nowozin, A. Strittmatter, M. Nasser Ajour, K. Daqrouq and D. Bimberg, *230 s room-temperature storage time and 1.14 eV hole localization energy in $In_{0.5}Ga_{0.5}As$ quantum dots on a GaAs interlayer in GaP with an AlP barrier*, Appl. Phys. Lett. **106**, 042102 (2015).

  http://aip.scitation.org/doi/full/10.1063/1.4906994

- G. Stracke, E. M. Sala, S. Selve, T. Niermann, A. Schliwa, A. Strittmatter, and D. Bimberg, *Indirect and direct optical transitions in $In_{0.5}Ga_{0.5}As$/GaP quantum dots*, Appl. Phys. Lett. **104**, 123107 (2014).

  https://aip.scitation.org/doi/10.1063/1.4870087

Conference contributions

1. *MOVPE growth and characterization of $In_{0.5}Ga_{0.5}Sb$ quantum dots on GaP(001) for nanomemories*, **invited seminar at the Masaryk University, Brno (Czech Republic)**, 2017.

2. *Growth and structure of $In_{0.5}Ga_{0.5}Sb$ quantum dots on GaP(001) for nanomemories*, **International Conference on Nano-photonics and Nano-optoelectronics (ICNN2017), Yokohama (Japan)**, 2017.

3. *Growth and structure of $In_{0.5}Ga_{0.5}Sb$ quantum dots on GaP(001)*, **18th International Conference on Metal Organic Vapor Phase Epitaxy (ICMOPVE), San Diego (USA)**, 2016.

4. *Growth and structure of $In_{0.5}Ga_{0.5}Sb$ quantum dots on GaP(001)*, **Deutsche Physikalische Gesellschaft (DPG) Frühjahrstagung, Regensburg (Germany)**, 2016.

5. *Growth and structure of $In_{0.5}Ga_{0.5}Sb$ quantum dots on GaP(001)*, **International Nano-Optoelectronics Workshop (iNOW), Tokyo (Japan)**, 2015.

6. *Growth and structure of $In_{0.5}Ga_{0.5}Sb$ quantum dots on GaP(001)*, **Deutsche Physikalische Gesellschaft (DPG) Frühjahrstagung, Berlin (Germany)**, 2015.

7. *Growth of InGaSb quantum dots on GaP (001) in MOVPE*, 29. **DGKK Arbeitskreistreffen "Epitaxie von III-V Halbleitern" Magdeburg (Germany)**, 2014.

8. *Direct optical transitions in $In_{0.5}Ga_{0.5}As$/GaP quantum dots grown by MOVPE and luminescence study of individual quantum dots*, **International Conference on Quantum Dots, Pisa (Italy)**, 2014.

9. *Growth, structure and spectroscopy of $In_{0.5}Ga_{0.5}As$ quantum dots grown by MOVPE on GaP(001)*, **Deutsche Physikalische Gesellschaft (DPG) Frühjahrstagung, Dresden (Germany)**, 2014

Contents

Introduction **15**

1 Fundamentals **19**
1.1 Structures with reduced dimensionality: Quantum Dots 19
1.1.1 Electronic properties 20
1.1.1.1 Modeling of QD electronic structure and band alignment 21
1.1.2 Growth modes of epitaxial layers and QD formation 24
1.1.3 Quantum dots as storage unit in a novel memory device: the QD-Flash concept 27

2 Experimental methods **31**
2.1 Metalorganic Vapor Phase Epitaxy (MOVPE) 31
2.1.1 Metalorganic precursors 31
2.1.2 Growth process and MOVPE equipment 32
2.2 Atomic force microscopy (AFM) 34
2.3 Transmission Electron Microscopy (TEM) and Cathodoluminescence Microscopy (TEM-CL) 35
2.4 Static and and Time-Resolved Photoluminescence (PL, TRPL) 36

3 MOVPE of InGaSb QDs on GaP(001) **39**
3.1 Antimony-based QDs on GaP: state of the art 39
3.2 Epitaxy of InGaSb QDs on GaP (001) 40
3.2.1 Sample structure and experimental details 41
3.2.2 Insertion of a GaAs interlayer enabling QD formation 42
3.2.3 QD formation: growth mode, critical thickness 45
3.2.4 Effect of a growth interruption 47
3.2.5 Use of antimony-flush 48
3.3 Structural investigations on buried InGaSb QDs 51

4 Towards the non-volatility limit **57**
4.1 Adjusting the properties of QD heterostructures for longer storage times 57
4.2 DLTS structure preparation: a novel precursor for the GaP *p*-doping . 60
4.2.1 Surface morphology 62

4.3 Measuring retention time in QDs: Deep Level Transient Spectroscopy (DLTS) . . . 64
4.3.1 Electrical characterization . . . 67

5 Optical properties and electronic structure 73
5.1 Sample structure for PL investigations . . . 73
5.2 Detection of QD luminescence via TEM-CL . . . 74
5.3 Development of QD luminescence . . . 76
5.4 Influence of increasing InGaSb coverage . . . 79
5.5 Modification of the V/III ratio during QD growth . . . 80
5.6 QD ripening during growth interruption . . . 81
5.7 Influence of antimony-flush on QD luminescence . . . 83
5.8 Optimization of QD cap layer thickness . . . 84
5.9 Temperature dependent investigations . . . 86
5.10 Expectations for a type-II band alignment . . . 89
5.11 Excitation power dependent investigations . . . 92
5.12 Time-resolved photoluminescence investigations . . . 98
5.13 Electronic configuration of InGaSb/GaAs/GaP QDs . . . 100

6 Summary and comparison with $In_{0.5}Ga_{0.5}As$/GaAs QDs on GaP 103

Conclusion and Outlook 107

A GaP substrate preparation before epitaxial growth: wet chemical treatments 109

Bibliography 113

Acknowledgments 129

Introduction

Until recently, the incredible fast progress of the semiconductor industry and information technology has been governed by the fast-pace downscaling of electronic components in the circuits, as forecasted by the empirical Moore law in 1965: *"the number of transistors on integrated circuits will double every two years"* [1]. Such prediction has been accurate for several decades now and has had also important consequences on the processing speed and price of technological and electronic goods. However, such rapid development by downsizing is no longer following the Moore law, hampered by the limits imposed by physics, as also announced in the updated *International Technology Roadmap for Semiconductors (ITRS)* in 2010 [2]. At present, the downsizing limit is represented by the 10 nm MOSFET (Metal-Oxide Semiconductor Field-Effect Transistor) gate length: such length could already lead to a direct source/drain tunnelling [3]. This limit has been set since many years, but recently a working 6 nm gate length MOSFET has been demonstrated [4]. However, it is still questionable if the present performances will be effectively improved also at a sub-10 nm level [3]: the theoretical threshold of 10 nm represents rather a *performance limit* of the downscaling. Hence, an important challenge to date is represented by the component integration in circuits [3], and novel functionalities of already existing devices would be of great advantage for this purpose. In particular, the branch of storage technology appears nowadays partly inadequate. The solid-state memory types are divided in two macro-categories, i.e. *volatile* and *non-volatile*, and commonly represented by the DRAM (Dynamic Random Access Memory) [5],[6] and the Flash memory. The DRAM shows fast write and access times ($\sim$20 ns) and good endurance ($>10^{15}$) but has poor retention times of the order of ms at room temperature, and it is therefore volatile. On the other hand, the Flash retains data for a long time ($>$10 years), being thus non-volatile, but shows slow write time ($\sim$ms). To overcome the gap between these two memory architectures, a universal non-volatile memory cell has to be considered, possibly combining the fast access times and good endurance of the DRAM and the long storage times of the Flash. Ideally, such a memory would be able to overcome the 10 years non-volatility limit. These properties are embraced by the QD-Flash [7],[8] which employs III/V quantum dots (QDs) as storage units, embedded in a MODFET (Modulation-Doped Field-Effect Transistor) structure. This memory concept has been developed at the Technical University of Berlin by Marent *et al.* in 2011 [9] and a functional QD-Flash prototype has already been demonstrated,

which is fully operating at temperature of less than 200 K [9],[10]. Here, every single QD would represent a single information bit. III/V self-assembled and defect-free Stranski-Krastanow (SK) QDs [11] are promising for such purpose: their fabrication takes advantage simply by the lattice mismatch between substrate and epilayer, without the need of surface pre-treatment, as for lithography. Also, the possibility to customize the material combination of QDs and the surrounding matrix makes such QDs excellent candidates as building blocks for the QD-Flash. In fact, choosing a suitable material composition would maximize the bandgap discontinuity, thereby enhancing the QD localization depth. Sb-based QDs embedded in a gallium phosphide (GaP) matrix, as for InGaSb/AlP/GaP, are considered one of the best options [12]. Furthermore, since GaP possesses a very small lattice mismatch to silicon ($< 0.4\%$) [13], the monolithic integration of GaP-based devices on silicon is feasible: the defect-free hetero-epitaxy of GaP on Si has been already successfully established [14],[15].
Since the beginning of the project aiming to develop such an ultimate QD-based memory architecture, the storage time for QDs has improved by 13 orders of magnitudes, i.e. from 0.5 ns of InAs/GaAs QDs [16] to the present 3200 s of InGaSb/AlP/GaP of this work, becoming thus gradually closer to the non-volatility limit of 10 years. This study opens up to the possibility to employ the large scale MOVPE growth of QDs for the future fabrication of the QD-Flash. Here, the record in the storage time for MOVPE-grown InGaSb/AlP/GaP QDs is demonstrated, amounting to almost 1 hour at room temperature. Such improvement has been exploited through the reduction of the QD capture-cross section of one order of magnitude, by introducing antimony during QD growth.

This thesis is organized as follows:

Chapter 1 illustrates the general physical principles of QDs and the growth modes of epitaxial layers. The concept of the QD-Flash is also introduced.

Chapter 2 gives an overview on the experimental techniques for the InGaSb/GaP QD structure fabrication, together with the methods used for their structural and optical characterizations.

Chapter 3 describes the growth process of InGaSb/GaP QDs, discussing the influence of the various growth parameters on the QD growth. Structural investigations on QDs are also presented.

Chapter 4 shows the preparation and electrical characterization of dedicated samples with embedded InGaSb/GaP QDs.

Chapter 5 investigates the optical properties of InGaSb/GaP QDs in detail, by means of static and dynamic photoluminescence. A proposal of electronic structure for such QDs will be also given.

Chapter 6 summarizes the results on InGaSb/GaP QDs and compares them with $In_{0.5}Ga_{0.5}As$/GaP QDs.

Appendix A gives a brief insight on the chemical treatment used for the preparation of the GaP wafers before epitaxial growth.

Chapter 1

Fundamentals

"I think that modern physics has definitely decided in favor of Plato. In fact the smallest units of matter are not physical objects in the ordinary sense; they are forms, ideas which can be expressed unambiguously only in mathematical language."

W. Heisenberg

1.1 Structures with reduced dimensionality: Quantum Dots

Quantum Dots (QDs) are semiconductor structures with reduced dimensionality, where the charge carriers are confined in the three spatial dimensions. When the QD size becomes comparable to the de Broglie wavelength λ_B of charge carriers quantum-mechanical effects occur. According to the concept of wave-particle duality, it can be expressed as

$$\lambda_B = \frac{h}{p} = \frac{h}{\sqrt{3m^* k_B T}} \tag{1.1}$$

where p is the carrier momentum, m^* its effective mass, k_B the Boltzmann constant, T the temperature and h the Planck constant. This leads to a three-dimensional localization of the carrier wave functions in **k**-space and to quantization of energy states, which appear thus discrete, similar to those observed in atoms. For this reason, QDs are also called *"artificial atoms"* [17] and were discovered for the first time in glass-crystals by the Russian physicist A. Ekimov in 1980 [18]. The quantization effects can be found in all type of QDs, whether self-assembled [19], colloidal [20],[21], or fabricated via lithography [22]. Of interest for this work are III-V epitaxial self-organized QDs.
This chapter gives a brief insight of the QD electronic properties and growth

modes (Sections 1.1.1 and 1.1.2) and on their application as storage unit for a novel nano-memory device (Section 1.1.3).

1.1.1 Electronic properties

The reduction of semiconductor dimensionalities and the consequent confinement of charge carriers leads to a profound modification of the density of states (DOS), which depends upon the downgrading level, as also schematically shown in fig. 1.1.

The density of states $g(E)$ for a 3D crystal - where the charge carriers have no spatial restriction and their energy levels are continuously distributed - is given by

$$g(E)_{3D} = \frac{1}{2\pi^2}\left(\frac{2m^*}{\hbar^2}\right)^{\frac{3}{2}}\sqrt{E} \qquad [cm^{-3}\cdot eV^{-1}] \tag{1.2}$$

where m^* is the effective mass and $\hbar$ the reduced Planck constant $\frac{h}{2\pi}$.

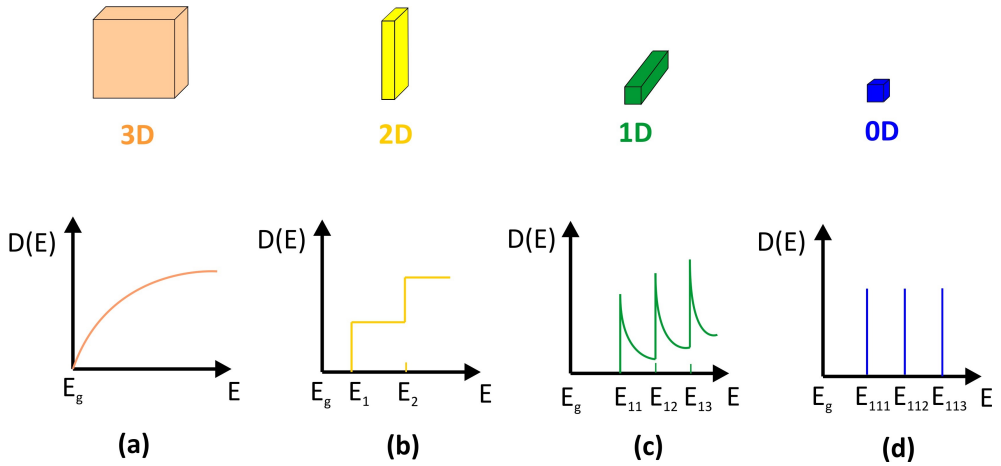

Figure 1.1: Schematic illustration of the density of states $g(E)$ for semiconductor structures with different degrees of dimensionality. **(a)** bulk, proportional to $\sqrt{E}$, **(b)** QW, step-like, **(c)** QWR and **(d)** QD, spike-like. After [20].

For a 2D semiconductor (*quantum well*, QW) the total density of states is the sum of all contributions from subbands and can be written as

$$g(E)_{2D} = \sum_{i=0}^{n} g_i = \frac{m^*}{\pi\hbar^2}\sum_{i=0}^{n}\Theta(E-E_i) \tag{1.3}$$

expressed in $cm^{-2} \cdot eV^{-1}$. The term $\Theta(E - E_i)$ represents the unit step function.

For the 1D case (quantum wire, QWR), carriers are quasi-free to move only along one spatial direction and the one-dimensional DOS is given by

$$g(E)_{1D} = \sum_{i=0}^{n} g_i = \frac{1}{\pi} \left(\frac{2m^*}{\hbar^2} \right)^{\frac{1}{2}} \sum_{i=0}^{n} (E - E_i)^{-\frac{1}{2}} \tag{1.4}$$

expressed in $cm^{-1} \cdot eV^{-1}$. If the mobility is further restricted for all three spatial dimensions, the zero-dimensional electronic DOS for a QD is the sum of δ functions:

$$g(E)_{0D} = \sum_{i=0}^{n} g_i = \sum_{i=0}^{n} \delta(E - E_i) \tag{1.5}$$

which leads to a fully quantization of electron and hole states, comparable to the discrete levels of an atom. Depending on the QD size and shape, only a finite number of energy states can exist. The energy level separation increases as the QD dimensions decrease and below a certain size no bound states exist anymore. For instance, a QD with lateral dimensions of ∼10 nm shows a typical energy level separation between 10 and 100 meV [23].

1.1.1.1 Modeling of QD electronic structure and band alignment

The confining potential of a buried QD is of finite depth and is given at first approximation by the band offset, which represents the band edge discontinuity appearing at the interface between two different semiconductors (*hetero-junction*). Depending on the relative energetic position of conduction and valence bands, QDs show a discontinuity either of type-I or -II, also called *band-alignment*. Fig. 1.2 shows schematically these two different band-lineups: typical type-I QDs are InGaAs/GaAs and confine both electrons and holes, while type-II[1] QDs provide confinement for either electrons or holes, which are therefore spatially separated [24]. An example for type-II QDs is given by GaSb/GaAs studied by Müller-Kirsch *et al.* in [25], where holes are localized in the QD, while electrons in the QD surroundings (GaAs matrix). Here, the electron wave-function (WF) is spread around the dot, resulting in a weak spatial electron-hole WF overlap [26],[27]. As a consequence, the carrier lifetimes for type-II structures are longer compared to those of type-I [28],[29]. The corresponding optical transition is, for type-II heterostructures, indirect, occurring between electrons in the QD surroundings and confined holes in the QD, while for a type-I QD it occurs between electrons and holes both confined in the QD body.

[1] The type-II band discontinuity is also known as *staggered* band alignment.

The type-II band-alignment allows for flexibility in controlling the electron-hole overlap and thus the charge carrier lifetime, which represents an important parameter for optical memories [30],[31] and *nano-memories* [12],[32].
In lasers, the use of a staggered type-II hetero-junction as active medium allows for tunability of the emitted radiation and was considered for the first time by Kroemer and Griffiths in 1983 [33]. Such lasers operate in the mid-infrared region of 3 - 7.3 μm and are desirable for various applications, such as chemical sensing, molecular spectroscopy and pollution monitoring and have been demonstrated in [34],[35]. Furthermore, type-II QD-based solar cells have been found to show an enhanced infrared response, compared to the GaAs cells without QDs and to InAs QD-based cells [36]. Additionally, the spatial separation of charge carriers may result in a large electrical polarizability of type-II QDs structures, as recently observed for type-II InAs/GaAsSb dots-in-a-well on GaAs [37]. Due to this property, the oscillator strength and the exciton radiative lifetime can be easily modulated by applying an external bias voltage, being thus convenient for semiconductor electro-optical applications. Finally, the use of type-II QDs can be implemented in the quantum information technology, as for quantum gates based on only one charge carrier type [38],[39].

A detailed discussion of the underlying physical mechanisms in a type-II QD-structure will be carried out in chapter 5.

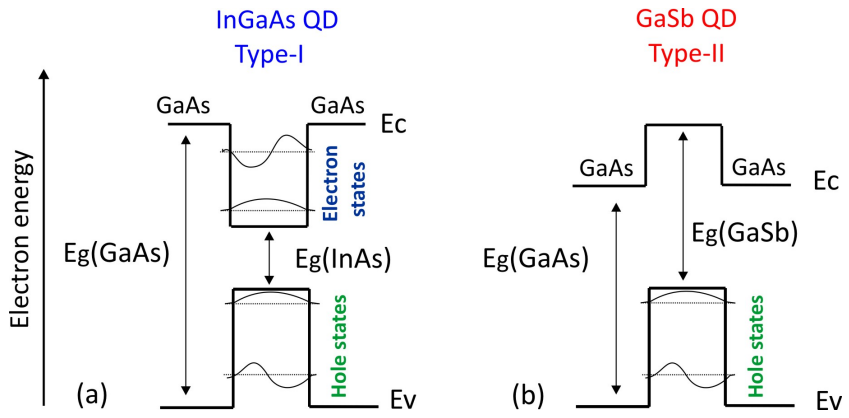

Figure 1.2: Sketch of type-I and type-II QDs, with indication of electron and hole states and band lineups. A typical type-I QD-system is represented by InGaAs/GaAs, whereas a type-II by GaSb/GaAs. Modified from [57].

The electronic structure of QDs can be modeled by using the 8-band **k·p** method [23],[41], which was initially developed to calculate the band-dispersion of a bulk semiconductor. It is basically derived from the Schrödinger equation describing the motion of a single electron under a given potential and allows to obtain the analytic expression for the band structures and effective masses at the center of the Brillouin zone, where the wave-vector $\mathbf{k} = 0$ (Γ point).

This method has been extended to the calculation of the electronic structure of buried QDs, where their electronic and structural properties can be connected with those of the matrix material. Important QD features like size, shape, composition, strain and piezoelectricity have to be taken into account to derive an adequate modeling. The 8-band **k·p** method is usually used to calculate the energy levels direct optical transition in type-I QDs [23], due to its restriction to the zone center Γ. For indirect type-II QDs, instead, where the minimum of the conduction band does not occur in the zone center Γ, other theoretical approaches are considered. The *tight-binding* (TB) model offers a suitable alternative to the 8-band **k·p** and enables to calculate the band positions at X and L ($\mathbf{k} \neq 0$), in addition to Γ. This model is also known as *Linear Combination of Atomic Orbitals* (LCAO), where electrons are considered to be tightly bound to the atoms, and the electronic WFs in the solid are approximated as linear combinations of atomic WFs [42],[43].
The matrix material for QDs used in this work (GaP) is an indirect semiconductor in **k**-space, with conduction band minimum at the X-point of the Brillouin zone [44]. Fig. 1.3 shows the band structure of an $In_{0.5}Ga_{0.5}As$ QD embedded in GaP.

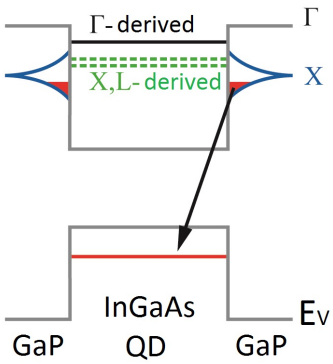

Figure 1.3: Sketch of the band structure and corresponding optical transition for a $In_{0.5}Ga_{0.5}As$ QD with height of $\sim$ 3 nm and diameter of $\sim$ 20 nm embedded in GaP matrix. Here, the transition energy between electron X states and QD hole states is determined to be $\sim$ 1.7 eV. From [40].

Here, the TB model has been used for determination of the QD energy states: the Γ level of QD lies above the X and L levels. Additionally, the strain generated by the lattice mismatch in the vicinity of the QD splits the X level of the GaP matrix, and a quantum well at the interface QD/matrix is formed, where electrons can localize. This causes a spatial separation of charge carriers: holes are localized in the QD and electrons in the surrounding matrix (in the QW in the QD vicinity) [40],[42]. Due to this configuration, the electron-hole WF overlap is weak, similar to that of usual type-II structures, as GaSb/GaAs. The bandgap is therefore indirect in both real and reciprocal space and the optical transition occurs between electrons in the QW at the interface with the QD and holes in the QD [40].

Material	$a(\AA)$	mismatch (%)	E_g (eV)
GaP	5.44	/	2.35 (X)
GaAs	5.64	3.5	1.52 (Γ)
$In_{0.5}Ga_{0.5}Sb$	6.29	13	0.33 (X), 0.41 (Γ)

Table 1.1: Lattice constants and energy gaps (with indication of bandgap point) of the three semiconductors GaP, GaAs and $In_{0.5}Ga_{0.5}Sb$ at T = 0 K [13]. The lattice mismatch of GaAs and $In_{0.5}Ga_{0.5}Sb$ with respect to GaP is also indicated.

1.1.2 Growth modes of epitaxial layers and QD formation

The QDs studied in this work have been fabricated epitaxially and in this section the fundamental mechanisms of epitaxial growth are discussed.

The expression *epitaxy* denotes the growth of a crystalline layer on a crystalline substrate. Such expression comes from the old Greek $\grave{\varepsilon}\pi\acute{\iota}$ ("*epi*"), which means "above", and $\tau\acute{\alpha}\xi\iota\varsigma$ ("*taxis*"), in an ordered way. The grown layer is also called "*epilayer*". If the epilayer has the same chemical composition as the substrate, the process is known as $homo$-epitaxy, otherwise as $hetero$-epitaxy. The substrate used for the growth experiments of this work is mono-crystalline gallium phosphide (GaP)[2], a III-V semiconductor having a zinc-blende crystal structure with lattice parameter 5.45 $\AA$. In hetero-epitaxy, the growing epilayer undergoes a strain, determined by the lattice *mismatch*, or *misfit*, between substrate and epilayer. Considering an epitaxial film with lattice constant a_0^{film} growing on a given substrate having a_0^{sub}, the lattice mismatch can be written as

$$f = \frac{a_0^{sub} - a_0^{film}}{a_0^{film}} \tag{1.6}$$

depending on whether f is negative or positive, the epilayer experiences a strain that can be either compressive or tensile, respectively. The mismatch f equals the in-plane strain $\varepsilon_{\parallel}$ of the growing epilayer. As the epilayer thickness increases, the strain energy accumulates in the growing layer. At a certain thickness d_c, called the critical layer thickness, it is energetically favorable for the system to plastically relax by developing dislocations, which are line defects represented by row of atoms.
Here, we consider the growth of III-V semiconductors as GaAs and InGaSb on GaP substrates. Both GaAs and InGaSb possess a larger lattice constant compared to that of GaP (as also clearly shown in fig. 1.4), which induces a compressive strain between substrate and epilayers. In table 1.1 their lattice parameters and misfits with respect to GaP are given.

[2]The crystallographic orientation is toward the (001) direction.

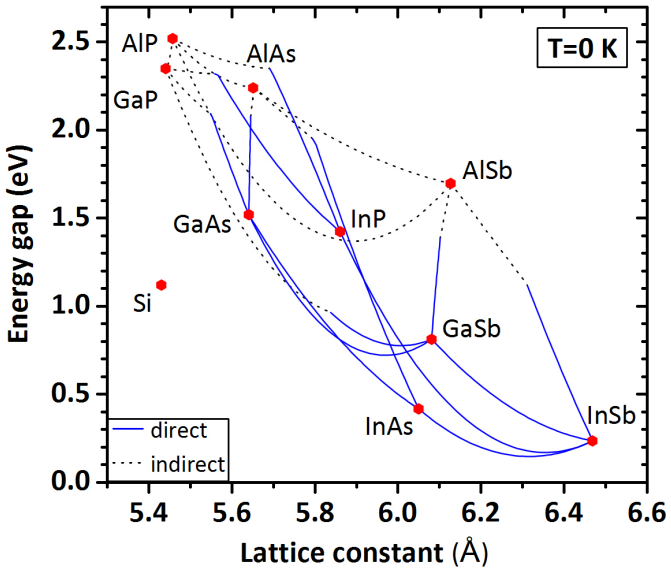

Figure 1.4: Scheme of the bandgap energy as a function of the lattice parameter for pure (red dots) and alloyed (lines) zinc blende semiconductors at T = 0 K. Direct and indirect bandgaps are also indicated, with blue straight lines and black dashed line,s respectively. After [13].

Generally, hetero-epitaxy is characterized by three growth modes, depending on the energy needed for the surface formation. For such distinction, three different surface energies are commonly used: γ_s, γ_e and γ_{se}, i.e. the surface energies of substrate, epilayer and interface substrate/epilayer, respectively. The growth modes can be summarized as follows:

1. **Franck van der Merwe (FM)** [45], where the epilayer atoms are attracted more strongly to the substrate than to each other. The epilayer wets the substrate surface completely and builds therefore an homogeneously closed layer. This is also known as *layer-by-layer* growth. Here, $\gamma_s \geq \gamma_e + \gamma_{se}$.

2. **Volmer-Weber (VW)** [46], where the epilayer atoms are more strongly attracted to each other than to the substrate. The epilayer does not wet completely the substrate, but it aggregates forming three-dimensional islands, which is energetic favorable. This mode is also known as *island growth*. Here, $\gamma_s < \gamma_e + \gamma_{se}$.

3. **Stranski-Krastanow (SK)** [11] represents an intermediate growth mode between FM and VW. The epilayer grows initially two-dimensionally in FM mode up to a critical thickness d_c, and the condition $\gamma_s \geq \gamma_e + \gamma_{se}$ applies. After exceeding a certain d_c, it is for the system energetic favorable to build new surfaces as 3D islands (minimization of total energy): the growth mode changes to VW, and $\gamma_s < \gamma_e + \gamma_{se}$. This change is ascribed to

the accumulation of elastic energy in the epilayer. The phase-transition from 2D- to 3D-growth takes place when the energy gained in the island formation is larger than the sum of the energy required for generating new facets and edges of the 3D island ($E_{tot} > E_{relax} + E_{surf} + E_{edge}$)[3] [47]. The lattice mismatch between epilayer and substrate plays a key role in determining the d_c upon which the phase transition occurs. Indeed, due to the mismatch, strain energy accumulates in the epilayer during the early 2D growth and relaxes elastically creating new surfaces in form of defect-free 3D islands. The few initial 2D monolayers (MLs) are normally referred to as *wetting layer* (WL). The SK mode is also known as *layer-plus-island* growth.

In the following picture the above discussed growth modes are depicted:

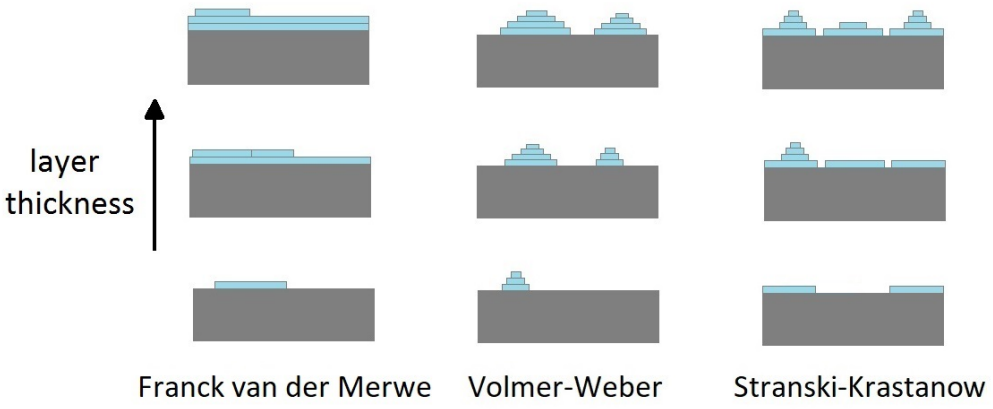

Figure 1.5: Schematic depiction of the three different growth modes of epitaxial layers.

The SK mode is the most successful approach for fabricating *self-assembled* and defect-free QDs [48]. They organize themselves spontaneously without the need of any other external driving-force, except for the strain generated from the lattice mismatch between substrate and epilayer. Their density can reach $\sim 10^{11}$ cm^{-2} making their use suitable for different kind of devices: as active medium for lasers, where they are used to enhance the optical gain, both high-speed edge-emitting [50],[51] and surface emitting [52],[53]; as optical amplifiers in opto-electronic applications [54],[55], for intermediate-band solar cells, where QDs are used to obtain additional sub-gap absorption, thereby increasing the current gain [56]; and, last but not least, for *nano-memory cells* [7]-[9],[57], where QD are used to store information as a memory cell.
The InGaSb/GaP QDs studied in this work are fabricated via SK method and

[3] E_{relax}, E_{surf} and E_{edge} represent the contribution from bulk strain relaxation, from formation of facets and of QD edges, respectively.

their formation process will be discussed in detail in chapter 3. The SK-grown QDs show little variations in size and shape which lead to a smearing of the QD localization energies. Consequently, the emission lineshape of a QD ensemble consists of a superposition of single QD emission, resulting in an inhomogeneous broadened ($\geq$ tenth of meV) spectrum.

1.1.3 Quantum dots as storage unit in a novel memory device: the QD-Flash concept

To date, the semiconductor memory market is dominated by two kind of memory types, the DRAM and the Flash-memory. The Flash is characterized by long storage times ($>$10 years) and is therefore *non-volatile*, but shows slow write times ($\sim$ms). It is usually used as memory device in portable applications and in many electronic products, as computer or industrial equipments, storing their operation instructions. On the other hand, a DRAM cell represents the main memory in a PC (personal computer) and provides fast write and access times ($\sim$20 ns), but has poor storage times of $\sim$ms at room temperature, being thus *volatile*. Moreover it shows a good endurance[4] of $>10^{15}$. A *universal non-volatile memory cell* should combine the fast access times and the good endurance of a DRAM and the long storage times of the Flash, ideally being able to overcome the 10 years non-volatility limit. A new kind of nano-memory embracing these characteristics is represented by the *QD-Flash*, developed at the Technical University of Berlin by Marent *et al.* in 2011 [9]. A prototype of the QD-Flash is schematically depicted in fig. 1.6.

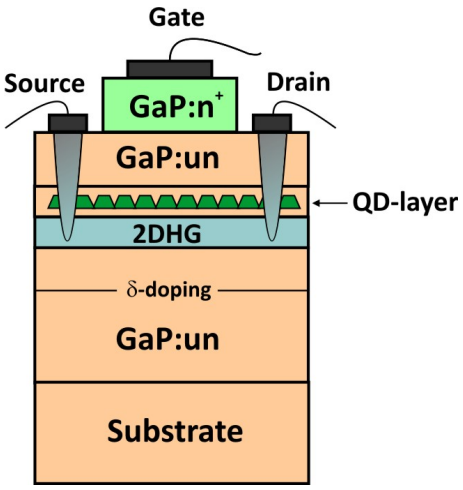

Figure 1.6: Schematic cross section of a QD-Flash based on GaP. This structure is basically a p-MODFET with embedded QDs. The holes for the 2DHG are released by the δ-doping layer. After [58].

[4]The *endurance* is defined as the minimum amount of write/erase cycles expected within a memory-cell life.

It employs III-V-based *self-organized* QDs embedded in a *p*-*n*-diode as storage unit, where every QD represents a single information bit (logic '1' = charged QD, logic '0' = uncharged QD). Considering for instance a typical areal density of 10^{11} QDs/cm^2 (usual density of SK QDs), a storage density up to $\sim$1 TBit/inch^2 might be obtained, provided that every single QD can be addressed individually. For the storage of charge carriers, a capture barrier is needed, which is realized taking advantage of the band bending of the *p*-*n*-diode. Using a diode structure has thus the advantage that the barrier heights can be tuned by simply applying an external bias voltage: the barrier can be eliminated by a positive bias between source and gate and the carriers can thus relax in QD states. As holes possess a larger effective mass than electrons, hole localization is preferred [10]. Indeed, the energy levels of holes confined in QDs are closely spaced (few $\sim$meV) and therefore up to an order of magnitude more holes can be stored with respect to electrons [23], [59], thereby maximizing the storage capacity of a single QD. The carrier capture of holes into QDs has been demonstrated to be $\sim$3 ps at room temperature [60]. This leads to a fast write time of $\sim$6 ns [61], making the QD-Flash competitive with the DRAM in the memory market [5],[6].

The three memory operations of a QD-Flash device are schematically depicted in fig. 1.7 and can be described as follows:

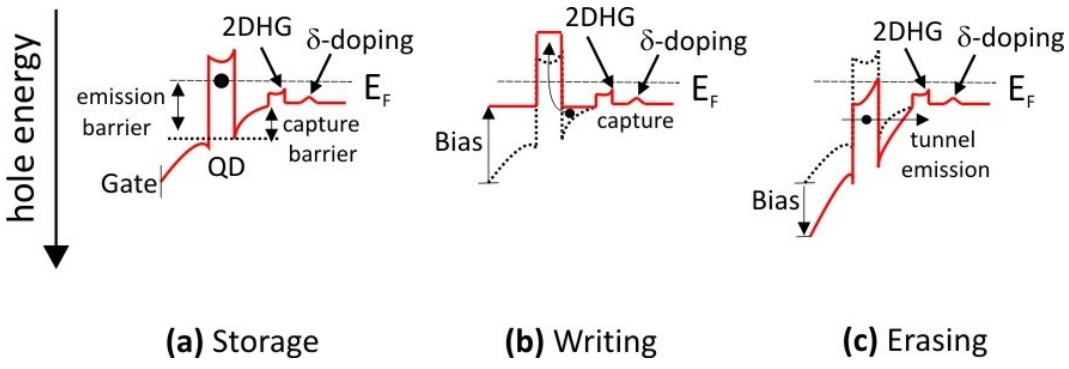

Figure 1.7: Schematic picture of the three operations of a hole-based QD-Flash structure. The Fermi level E_F is also indicated, which is pinned through the device by the 2DHG. From [12].

- **Storage**: to store a logic '1' in the QD-Flash (filled QD), the holes need to be localized in the QD, and this can be achieved by using an emission barrier formed by the charge carrier binding potential, i.e. their localization energy in the QD (fig. 1.7 **(a)**). The logic '0' instead, is represented by an empty QD; this state is maintained by the bend-bending of the diode.

- **Writing**: a forward bias is applied to the gate to eliminate the emission barrier generated by the bend-bending. Here, writing time of the order of ns can be obtained [61] (fig. 1.7 **(b)**).
- **Erasing**: the erasing of information is obtained by applying a reverse bias to the gate. By doing so, the tunnel barrier becomes narrower and a tunnel emission occurs (fig. 1.7 **(c)**).

The read-out of the charge state is done through a conductance variation of a 2DHG[5] (two-dimensional electron gas) in the vicinity of the QD-layer ($\sim$10 nm, see also fig. 1.6), leading to read times down to $\sim$3 ns for both charge states [62]. The δ-doping aims to create a well-define interface between the free charge carriers and doping impurities and provides holes for the 2DHG.

The carrier emission[6] is found to limit the storage time of a QD-Flash, but the device is designed so that only the thermal emission dominates the emission process [64]. To investigate the thermal emission of charge carriers from QDs and determine their storage time and localization energy, the Deep Level Transient Spectroscopy (DLTS) method [64],[65] is used. The storage time for carriers depends primarily on the depth of the localization potential provided from QDs and on their capture cross section σ_∞, which measures the scattering probability of holes with the surrounding matrix. Type-II QDs exhibiting hole confinement are preferred for QD-based memory applications, as the valence-band discontinuity is maximized for a given bandgap. Indeed, they lead to a higher carrier localization energy and to an increased storage capacity for single QD, with respect to type-I heterostructures [12],[66]. They are therefore considered the best candidates to be storage units for the future QD-Flash.

The reader is referred to chapter 4 for the discussion on the DLTS method, aiming to determine the storage time and capture cross-section of InGaSb QDs embedded in dedicated *n*-*p* structures.

[5]The charge density in 2DHG is decreased when holes are trapped in QDs and, as a consequence, the carrier mobility is diminished: this can be detected in the conductance variations of the 2DHG [9].

[6]There are three main carrier emission processes from QDs: thermal activation, tunneling, and optical activation [63],[58].

Summary

- QDs are semiconductor structures of reduced dimensionality, where the charge carriers are localized in all three spatial dimensions of space. They can be fabricated with different techniques; of interest for this work are epitaxial self-assembled QDs, also known as Stranski-Krastanow (SK) QDs.

- The SK growth mode allows for fabrication of self-assembled and defect-free QDs simply by taking advantage of the lattice mismatch between substrate and epilayer. By overcoming a critical layer thickness, determined by the mismatch, the epilayer relaxes elastically by creating new surfaces and edges and defect-free QDs are formed.

- By properly choosing the constituting materials for QDs and matrix, it is possible to employ such QDs as building blocks for a new memory device: the QD-Flash. Here, QDs are used to store the information by localizing the charge carriers for a given period of time.

- The best candidates as storage unit for the ultimate QD-Flash are represented by the type-II QDs, where the valence-band discontinuity is maximized, so that surpassing the non-volatility limit of 10 years becomes feasible.

Chapter 2

Experimental methods

"Die Anlage läuft störungsfrei"

"The machine runs smoothly"

Prelude of (almost) every
MOCVD meeting

In this chapter the experimental methods used for fabrication and characterization of QD structures are discussed. In section 2.1 the epitaxial technique used for QD growth will be described, while the methods for structural and optical characterizations are presented in sections 2.2 - 2.4.

2.1 Metalorganic Vapor Phase Epitaxy (MOVPE)

The Metalorganic Vapor Phase Epitaxy (MOVPE), also known as MOCVD (Metalorganic Chemical Vapor Deposition), is a versatile epitaxial growth technique used to grow compound semiconductors from metal-organic gases, developed for the first time by Manasevit and Simpson in 1969 [67]. It is a synthesis process, in which the chemical precursors are carried in a gas-phase to the vapor-solid interface of a heated substrate to form a solid deposit [68]. Fast deposition rates up to tenths of μm/h can be reached, together with good material uniformity and abrupt interfaces. MOCVD allows for high-quality and large-scale industrial production of semiconductor devices and is therefore cost-effective. The QD fabrication, which was initially developed with the Molecular Beam Epitaxy (MBE) technique, has been extended to MOCVD since about thirty years [69],[70].

2.1.1 Metalorganic precursors

The chemical precursors used in MOCVD are either metal-organics (MO) or hydrides. Metal-organics are combinations of a given element and one or more

carbon atoms of an organic hydrocarbon group, for example triethylgallium, $Ga(C_2H_5)_3$, also known as TEGa. Hydrides are instead compounds where Hydrogen is bound to a more electro-positive metal or metalloid, as Phosphine, PH_3. The precursors are carried into the reactor by using an inert carrier gas, in this case hydrogen in form of H_2, and they are thermally decomposed at the vapor-solid interface of a heated substrate. This process is assisted by a certain number of chemical reactions. In this work, the sources PH_3 and TEGa have been used as precursors to grow epitaxial gallium phosphide (GaP). The reactions leading to formation of GaP include the thermal dissociation of the above mentioned precursors and can be written as:

$$Ga(C_2H_5)_3 + PH_3 \rightarrow GaP + C_2H_2 + 4CH_4 \uparrow \tag{2.1}$$

$$Ga(C_2H_5)_3 + PH_3 \rightarrow GaP + 3C_2H_2 + 6H_2 \uparrow \tag{2.2}$$

The complete set of chemical reactions occurring at the vapor-surface interface are in practice more complex and consist of many additional steps: a precise description of these processes goes beyond the scope of this work and could be found elsewhere [68],[71].

2.1.2 Growth process and MOVPE equipment

The complex MOVPE growth process is schematically shown in fig. 2.1 and can be identified with five consecutive steps:

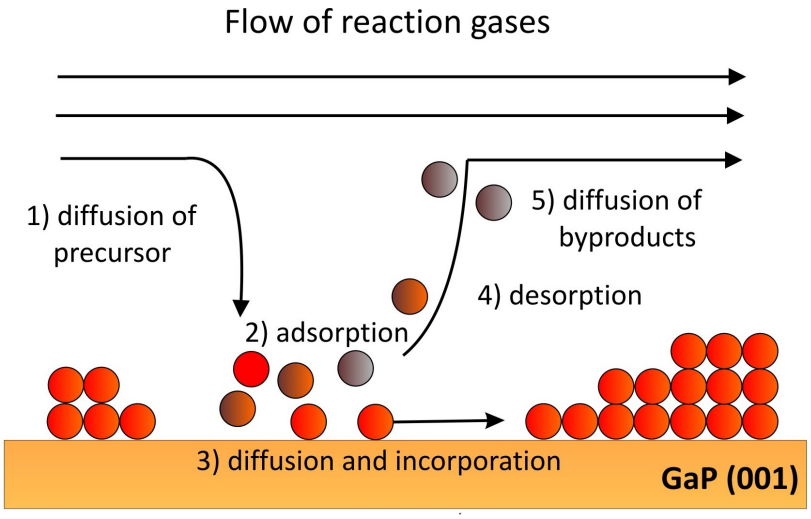

Figure 2.1: Schematic representation of the MOVPE growth processes taking place at the vapour-solid interface of a GaP(001) substrate.

1. diffusion and decomposition of reactants at the solid surface;
2. adsorption of the constituent elements on the surface;
3. adatom diffusion and incorporation in the epilayer;
4. desorption of the excess reaction species from the interface;
5. diffusion and transport of byproducts.

The processes comprising adsorption, adatom diffusion, and incorporation make up the interface reactions. The precursors carried by H_2 represent the source materials: they flow towards the substrate surface and react chemically at the interface. After adsorption, the source molecules diffuse and become eventually incorporated in the growing epilayer. After growth, excess reaction byproducts desorb from the surface and are transported away with the flow rate. For a detailed description of the MOVPE process, the reader is referred to G. B. Stringfellow [68],[71].

All growth experiments carried out in this work were performed at the Institute of Solid-State Physics of the TU Berlin by using a MOVPE equipment of the $Aixtron$ company, type $AIX\ 200\ RF$, with a horizontal quartz reactor. A schematic illustration of the apparatus is shown in fig. 2.2.

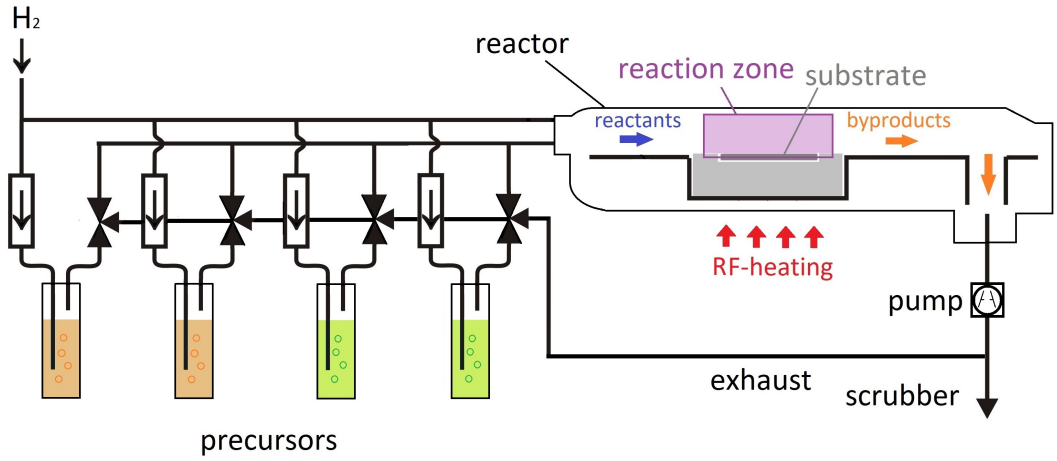

Figure 2.2: Schematic diagram representing the MOVPE apparatus used in this work.

The metalorganic precursors are stored in bubblers in liquid form (rarely solid), whose temperature and pressure is kept constant at a given value depending on the material. Inside each precursor container, the precursors form an equilibrium vapor pressure. The bubbler pressure is regulated by using a pressure controller, which is placed at the bubbler outlet. The carrier gas (H_2) flows through the bubblers via a pipe and saturates with the precursor molecules. Thereafter, the

reactant is carried to the reactor. On the other hand, the hydrides are stored at 20°C in liquid form and PH_3 is usually kept under a pressure of $\sim$ 40 bar. In this way, the hydrides can be transported directly into the reactor in gaseous form. A valve for each precursor line is also used to regulate the gas flow, which is measured in *mass flow* as **mol/min** (moles per minute) or *volume flow* (**sccm**, standard cubic centimeters per minute). During an epitaxy experiment, the total flow rate running through the whole MOVPE system is kept constant at the standard value of 5000 sccm. The reactants of groups III and V are injected separately into the reactor, to avoid any preceding chemical reaction between them. Indeed, the reactions mentioned before occur in the reaction zone at the vapor-substrate interface on a graphite susceptor (see also fig. 2.2). The heating is provided through induction by a radio-frequency generator (RF coil). The samples used in this work have been grown in a temperature range between 500 and 750 °C. The substrate temperature is measured by using a thermo-element, which is placed in the susceptor under the substrate. A sample rotation is provided (with a maximum velocity of 50 rpm) to ensure a uniform growth rate over the whole substrate surface. The reaction byproducts after the growth process are pumped away in the exhaust system.

The samples fabricated via MOVPE are characterized *ex-situ* using different experimental techniques. Structural characterizations have been carried out with atomic force microscopy (AFM) and transmission electron microscopy (TEM), while optical properties have been investigated by static photoluminescence (PL) and time-resolved photoluminescence (TRPL). Additionally, cathodoluminescence transmission electron microscopy (TEM-CL) was used to link optical information with structural properties.
The MOVPE growth, the AFM and static PL measurements have been performed by the author of this work. TRPL and TEM investigations have been carried out at the TU Berlin (Department of Solid-State Physics and Institute for Optic and Atomic Physics, respectively), while TEM-CL at the Institute for Experimental Physics of the University of Magdeburg.

2.2 Atomic force microscopy (AFM)

Atomic force microscopy (AFM) is a method used to investigate surfaces with a resolution of fraction of nanometer and was developed for the first time by Binnig and Quate in 1986 [73]. The essential components of the AFM are the followings:

1. a tip mounted on a cantilever spring,

2. a detection system to sense the cantilever deflection,

3. a feedback system for monitoring and controlling the cantilever deflection (i.e. the interaction force between tip and sample),

4. a raster scanning system moving the sample under the tip, and

5. a conversion system translating the acquired data.

The surface morphology is built by a sample scanning along an x-y grid: the variation in the cantilever deflection is used to quantify the distance between tip and sample, and is translated in height and width variations of the surface[1]. Piezoelectric elements under the specimen allow for precise movements on electronic command, which enable an accurate surface scanning. The distance between tip and specimen is usually between some $\mathring{A}$ngstroms and few nanometers and the tip-sample interaction forces are well described by *Lennard-Jones potentials* (L-J) [74]. The interaction range determines the operation modes which are *contact*, *non-contact*, and *tapping*. In non-contact (or attractive) mode, the tip-specimen separation is of the order of ten to hundreds $\mathring{A}$, and therefore the interaction is of long-range, represented by the Van der Waals attraction forces. In contact (or repulsive) mode, the distance is about few $\mathring{A}$ and thus of short-range, represented by the Born repulsive forces. In tapping mode (or intermittent contact), the cantilever oscillates with a given frequency and the surface morphology is reconstructed considering the variation of its oscillation amplitude. This mode operates between the attractive and repulsive region of the L-J potential. A more detailed discussion on the AFM operation and recent developments can be found in [75].
The AFM measurements of this work have been carried out in *contact mode*, and used to determine size and density of QDs. To this purpose, dedicated samples have been fabricated, where free-standing QDs have been grown without any additional capping layer. It is worth noticing that the lateral resolution of structures in AFM is limited by the physical size of the tip apex (the tips used here have a typical radius of 10-20 $\mathring{A}$).

2.3 Transmission Electron Microscopy (TEM) and Cathodoluminescence Microscopy (TEM-CL)

Transmission electron microscopy (TEM) is a microscopy technique for microstructural analysis of materials which employs the interaction of energetic electrons with matter. It was invented by M. Knoll and E. Ruska at the Technical University of Berlin in 1931 [76] and in 1986 Ruska was awarded the Nobel Prize in Physics for its development. As electrons interact strongly with matter (they are scattered by the repulsive potential in the electron clouds) and

[1]It is important to point out that only an upper size limit of structures can be inferred due to the convolution of sample surface with the tip shape.

can be easily focused, electron diffraction allows for a high-resolution imaging from microscopic parts of a sample, thereby obtaining very precise morphological information. Electrons are usually thermo-ionic emitted from an electron gun, as a tungsten filament, and transmitted through an ultra-thin specimen, usually between 10 and 100 nm thick. After being scattered from the constituting atoms of the specimen, a lens objective system is used to magnify the image resulting from the scattering. Thereafter, the image is focused on a fluorescent screen or a photographic film and can be analyzed. Two analysis can be performed:

- a *diffraction contrast*: an image of intensity variation of the diffracted electrons emerging from the specimen. The imaging can be either bright or dark field: the bright field is the most common method used in TEM, where the contrast image is formed by direct diffraction of electrons. Here, sample regions with heavier atoms appear dark, in contrast to the surrounding matrix. This method is also useful for detecting the presence of lattice defects, such as dislocations, stacking faults or antiphase boundaries.
- a *phase contrast*, which enables a high-resolution TEM imaging (known as HRTEM). Here, the phase of the diffracted electron wave interferes constructively (or destructively) with the one of the transmitted wave. Through this process, pillars of atoms can be distinguished, with resolution down to $\mathring{A}$.

In this work, both methods are used for the structural investigations of InGaSb/GaP QDs, as will be shown in chapter 3.

The use of cathodo-luminescence microscopy (CL) in the TEM permits to correlate optical and electronic properties of an investigated material with its morphology, providing luminescence information from a certain specimen area. The big advantage of this analytical technique is that the excitation beam can be focused with a diameter of few nm, providing luminescence information from a very precise specimen area. Through a line-scan, the luminescence spectra at every position are recorded. The luminescence information is then correlated with a contrast map of the investigated area, which corresponds to local fluctuations of the constituting elements. For investigations carried out in this study, the samples have been excited via a high-energy electron beam (80 keV) and the signal detected by using a Silicon-CCD camera. A detailed discussion of the TEM-CL method can be found in [77].

2.4 Static and and Time-Resolved Photoluminescence (PL, TRPL)

Photoluminescence (PL) represents the emission of photons due to a previous external excitation by means of an electromagnetic radiation. Photons of higher

energy than the material bandgap are absorbed and electron-hole pairs are optically generated in the medium. The carriers relax in the lowest energy level and recombine by emitting photons with energy lower than the exciting ones. The recombination energy represents the energy separation of the transition states involved. For the investigations carried out in this work, the excitation source is a blue laser with emission wavelength of 441 nm, corresponding to 2.81 eV, which lies above the GaP bandgap (2.35 eV at T = 0 K [13]). The light emitted from the sample is spectrally resolved by using a monochromator and detected with a Silicon photodetector (with a spectral sensitivity between $\sim$1.1 and $\sim$6.5 eV). The excitation density on the sample can be varied either by varying the laser output power or by using gray filters between the laser and the sample.

The time-resolved photoluminescence (TRPL) allows for the study of the charge carrier dynamics in a semiconductor structure. In particular, it is possible to determine the carrier decay transients at a specific wavelength and the processes underlying the carrier dynamics can be investigated on a time-scale of nanoseconds. Also information about the material quality can be collected, as impurities and defects can remarkably affect the carrier dynamics. This kind of technique is especially convenient to study type-II QDs: here, the electron-hole wave-function overlap is noticeably reduced and results in much longer decay times for charge carriers, with respect to type-I QD-structures.
The setup used for the TRPL measurements consists of a dye laser with emission wavelength of 445 nm, that provides pulses in the ns-range, alongside a detection system with resolution of $\sim$0.4 ns.

Summary

- MOVPE is a versatile and cost-effective epitaxial growth technique which allows for the growth of a wide range of semiconductor structures. Recently, it has been also exploited for the fabrication of high-quality semiconductor nanostructures like QDs.

- Various experimental techniques are used for the structural and optical characterization of the InGaSb/GaP QDs studied in this work. AFM is employed to determine size and density of free-standing QDs, although the lateral resolution is limited by the tip size. TEM, instead, allows for a more precise determination of QD size (buried QDs) and for detection of lattice defects, like dislocations.

- Static and time-resolved PL are employed to investigate the optical properties of QDs. TRPL allows to study the charge carrier dynamics at a given wavelength, being particularly useful for determining the direct or indirect character of a given optical transition in QDs. Additionally, through the use of CL microscopy in the TEM, the optical properties of a heterostructure can be correlated with its morphology.

Chapter 3

MOVPE of InGaSb QDs on GaP(001)

"Geduld ist der lange Atem der Leidenschaft".

"Patience is the long breath of passion".

K. Bund

In this chapter the formation of InGaSb/GaP QDs via MOVPE is discussed in detail. To date, no other studies on the growth of such QDs are reported in literature, neither in MOVPE nor in MBE environment: the growth of type-II InGaSb QDs in GaP matrix has been demonstrated for the first time in this work and published in [78].

3.1 Antimony-based QDs on GaP: state of the art

The use of type-II antimony-based QD is of great importance for increasing the storage time in nano-memory applications, as already mentioned in chapter 1. Recently, two research groups have explored the growth of GaSb QDs on GaP in a MBE environment: a Russian, at the *Novosibirsk State Technical University* [79],[80], and a French at the *University of Lille 1* [81]. In [79],[80], Abramkin *et al.* report on the growth of dislocation-free Stranski-Krastanow Ga(Sb,P) QDs on bare GaP. Such QDs are grown between 420 and 470 °C and exhibit photoluminescence between 1.6 and 1.9 eV: here, also the emission of a wetting layer (WL) is clearly observed. The authors compare the data of the PL emission energy with the transition energies of theoretical predictions which allows for the estimation of the QD stoichiometry. The experimental results find agreement with the calculations if a strong P/Sb intermixing (up to $\sim$ 75

%) in the QD structures is considered. Interestingly, they attribute the QDs to follow an indirect type-II transition, while the WL a type-I. The authors conclude that an intermixing between P and Sb during QD formation reduces the lattice mismatch between QDs and matrix, enabling the QD growth and preventing the introduction of misfit dislocations. It is worth noticing that the lattice mismatch between GaSb and GaP amounts to ∼10.5 %, a quite challenging value to ensure defect-free Stranski-Krastanow growth (for comparison, the well-studied QD systems InAs and $In_{0.5}Ga_{0.5}As$ on GaAs exhibit a lattice mismatch of 6.7 % and 3.5 %, respectively [13]).

Desplanque *et al.* in [81] study in detail the GaSb QD formation under different growth conditions (i.e. variation of growth temperature and rates, which range between 410 and 485 °C and between 0.1 and 0.2 ML/s, respectively). It is worth noticing, that such GaSb/GaP QDs have recently shown very promising results in the hole retention time (∼ 4 days at room temperature) [82]. In [81] it is shown that uncapped QDs are plastically relaxed having 60° interfacial dislocation pairs, which are not present upon capping with a few nm-thick GaP layer. Through structural investigations by means of HAADF-TEM[1], the authors observe a moderate P/Sb exchange between 10 and 20%, leading to a ∼10 nm intermixed layer above the QDs made of GaP/GaSb. This behavior is explained by the Sb/P interdiffusion during QD capping that results in a relief of the strain accumulated in the QDs. Such mechanism prevents the formation of dislocations, similarly to the Ga(Sb,P) QDs in [79]. The strain-relief upon capping was also investigated for $In_{0.5}Ga_{0.5}As$/GaAs/GaP QDs, where a ∼2 ML GaAs capping layer was employed to relieve the strain accumulated in the QDs [40].

3.2 Epitaxy of InGaSb QDs on GaP (001)

The investigations on the growth process of InGaSb/GaP QDs carried out in this work take the InGaAs/GaP QD system studied by Stracke *et al.* in [40], [84] as starting point and reference, as the MOVPE growth of such material system has been extensively investigated and is therefore well-established. The InGaAs QD formation on GaP is enabled by utilizing a GaAs/GaP *pseudo-substrate*, i.e. by covering the initially bare GaP surface with a thin GaAs interlayer (∼ 2-3 ML). The purpose of this insertion is to modify the GaP surface termination from P- to As- thereby affecting the surface energy and adatom surface diffusion: this treatment leads to the SK formation of InGaAs QDs. The lattice mismatch of $In_{0.5}Ga_{0.5}As$/GaP amounts to ∼6.9 %, which is comparable to that of InAs/GaAs (∼6.7 %): this should enable the SK QD growth on GaP without any further surface pre-treatment. The ∼ 2-3 ML GaAs interlayer serves thus solely to modify the surface energetics, since it cannot be referred to an homogeneously closed layer.

[1] See [83] for detailed information on this experimental technique.

The first step towards the development of the growth of InGaSb QDs on GaP is therefore to replace As with Sb, maintaining the InGaSb material amount roughly proportional to that used for the $In_{0.5}Ga_{0.5}As$ growth, and obtaining a nominal composition of $\sim 50\%$ for both In and Ga. In this work, the notation InGaSb will refer to the nominal QD stoichiometry of $In_{0.5}Ga_{0.5}Sb$. In the next sections, the experimental details on the growth mechanism of InGaSb will be provided, while structural investigations on buried InGaSb QDs will be shown in sec. 3.3.

3.2.1 Sample structure and experimental details

The growth starts with a ∼500 nm GaP buffer grown at 750 °C with PH_3 and TEGa (V/III of ∼175, growth rate 2 μm/h). This temperature represents a standard value for the growth of GaP buffer layers: studies show that GaP epilayers grown at this temperature exhibit very good step-flow morphologies with regular step edges [49] which ensure a planar surface for growing the next epilayers. Thereafter, the substrate temperature is reduced to the temperature of QD deposition ($T_g = 500$ °C, usual for QD growth [85], [86]) for the following steps:

1. stabilizing of the GaP surface with TBP (*tributyl-phosphate*), precursor of phosphorus used at $T_g = 500$ °C;
2. growth of a thin GaAs layer, referred to as GaAs *interlayer*;
3. Sb-*soaking*, by means of TESb supply (*triethyl-antimony*);
4. InGaSb deposition for QD formation, by using TMGa (*trimethyl-gallium*), TMIn (*trimethyl-indium*) and TESb;
5. growth interruption (GRI) without any supplemental group-V precursor supply, for a specific sample set to study the temporal evolution of QDs.

The purpose of using an Sb-*soaking*, or Sb-flush, before the QD deposition is to initiate the antimony incorporation in QDs (see sec. 3.2.5). The precursor molar flows used during QD growth are: TMGa = 4.2 μmol/min, TMIn = 4.2 μmol/min, and TESb = 2.5 μmol/min, resulting in a V/III ratio and growth rates of ∼0.3 and 0.15 ML/s, respectively. For the GaAs interlayer, instead, a V/III of 17 and a growth rate of 0.25 ML/s have been used respectively.

For structural investigations by means of AFM, the samples have been immediately cooled down after QD growth (QDs are therefore free-standing). The usual sample structure for AFM investigation is shown in figure 3.1.

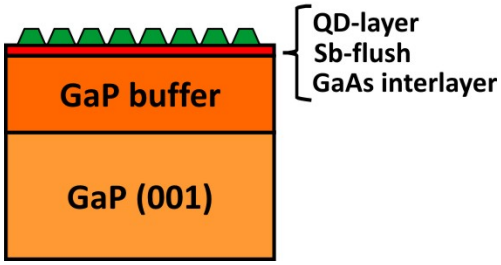

Figure 3.1: Schematic structure of a typical AFM structure with free-standing QDs.

3.2.2 Insertion of a GaAs interlayer enabling QD formation

Before investigating the MOVPE growth of InGaSb/GaP QDs, the growth mode of GaAs on GaP has been tested. The lattice mismatch between GaAs and GaP amounts to ∼3.5%, a value that could enable SK QD growth. For comparison, the well-known QD system $In_{0.5}Ga_{0.5}As$/GaAs exhibits a lattice mismatch of ∼3.5%, and its SK QD growth is well-estabilished [48],[85],[87]. Recently, Dadgostar *et al.* in [88] have demonstrated the SK growth of GaAs QDs on GaP in a MBE environment, by depositing 1.2 ML GaAs on bare GaP at $T_g = 450°C$ and growth rate of 0.3 ML/s.

In this work, a few GaAs MLs have been also deposited on a bare GaP surface. Fig. 3.2 shows the GaP surface after the deposition of 5 ML GaAs: a two-dimensional FM growth of thin GaAs epilayers on GaP can be maintained, and monolayer steps of a step-flow growth mode are clearly visible. Here, no QD formation is observed.

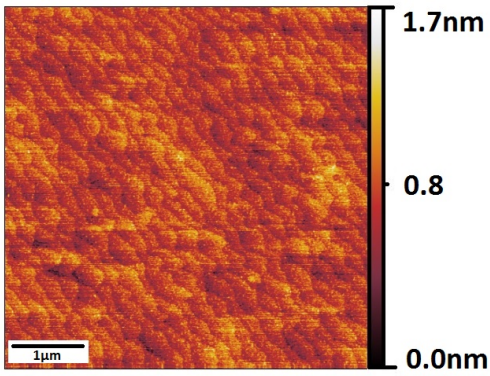

Figure 3.2: AFM micrograph of 5 ML GaAs grown on GaP.

The different outcome obtained for MOVPE growth, compared to MBE in [88], might be ascribed to the different physical conditions provided by a MBE

environment. In fact, the usual ultra-high-vacuum conditions of MBE might determine different GaP surface reconstructions, with respect to the same epilayers grown in a MOVPE reactor. Additionally, the different wafer heating method may cause slight variations in the substrate temperature. It is indeed well-known, that both the surface reconstruction and temperature can remarkably impact the surface energies and consequently the adatom surface diffusion: Rosini *et al.* in [89] showed that, for the growth of InGaAs on GaAs (001), the diffusion coefficient of In adatoms is strongly affected by the surface reconstruction of the GaAs surface[2]. This phenomena can determine, for the case of GaAs on GaP, whether the GaAs epilayer growth will follow a FM or a SK mode. To exploit the role of a thin GaAs interlayer on the InGaSb QD formation, a sample set with a fixed amount of InGaSb and increasing GaAs layer thicknesses has been prepared, i.e. between 0 ML (bare GaP) and 8 ML. As for the material system InGaAs/GaP [40],[84], if InGaSb is grown on bare GaP, neither VW nor SK QD growth is observed, as shown in fig. 3.3 **(a)**, where typical monoatomic steps are detected. For an interlayer thickness $<$ 3 ML, no QDs formation can be observed (fig. 3.3 **(a)**). By gradually increasing the GaAs coverage, the first QDs are formed for $\sim$ 3 ML and the QD density increases further proportional to it.

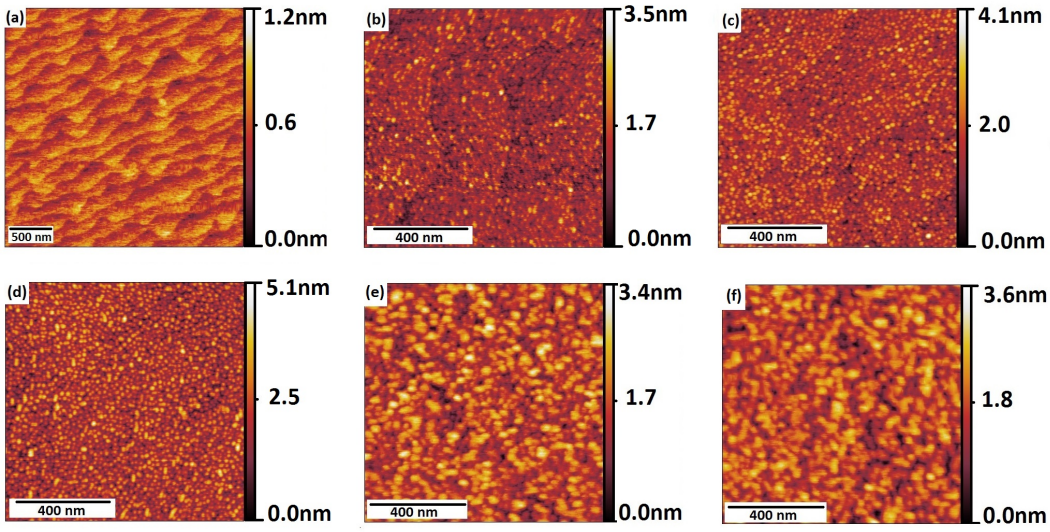

Figure 3.3: AFM micrographs of the GaP surface with fixed 0.42 ML InGaSb coverage: **(a)** without GaAs interlayer, with 3 **(b)**, 5 **(c)**, 6 **(d)**, 7 **(e)**, and **(f)** 8 ML GaAs. Sb-flush duration is of 1s for all samples [78].

Fig. 3.4 displays the 3D island density versus the GaAs interlayer thickness for a fixed amount of 0.42 ML InGaSb. The density varies from $6{\cdot}10^9$ cm^{-2} to

[2]Here, we refer to the example of GaAs (001), since studies on the surface diffusion of GaP (001) cannot be found (very old studies on this topic may exist but may not be available online).

$2{\cdot}10^{11}$ cm^{-2} for 3 and 6 ML GaAs respectively. For 3 ML, QDs are (27 $\pm$ 4) nm wide and (1.5 $\pm$ 0.5) nm high. If the GaAs thickness is further increased, small 3D islands merge into larger ones, as displayed in the AFM micrographs of figs. 3.3 **(e)** and **(f)**, with interlayer thickness of 7 and 8 ML, respectively. Here, the QD density drops accordingly to 10^{10} cm^{-2}.

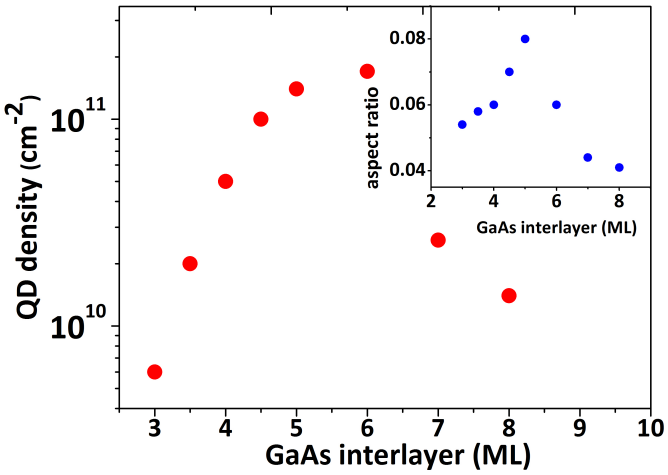

Figure 3.4: Logarithmic plot showing the variation of QD density towards GaAs interlayer thickness. The inset depicts the QD aspect ratio as a function of the GaAs thickness. InGaSb as QD material is fixed at 0.42 ML [78].

From 6 ML onwards, the QDs have a smaller *aspect ratio*[3] of ca. 0.03 compared to QDs grown on 5 ML GaAs, which show a typical ratio of $\sim$ 0.08. QDs show here heights between 2.2 and 2.4 ($\pm$ 0.6) nm, comparable to the value of (2.3 $\pm$ 0.4) nm for 0.42 ML InGaSb/5 ML GaAs, while the lateral dimensions are enhanced: from (28 $\pm$ 4) nm for 5 ML GaAs to (50 $\pm$ 12) nm and (58 $\pm$ 12) for 7 and 8 ML GaAs, respectively. Here, some of the biggest 3D islands might be already plastically relaxed. The inset of fig. 3.4 shows the evolution of the average aspect ratio of QDs with increasing GaAs thickness: the height-to-diameter ratio of QDs increases together with the GaAs interlayer coverage and from 6 ML GaAs starts decreasing. This observed dependence of QD morphology on the GaAs interlayer thickness clearly suggests that part of the GaAs interlayer becomes incorporated into QDs. As already pointed out, the high mismatch of 13% between GaP and $In_{0.5}Ga_{0.5}Sb$ represents a challenging value for enabling a defect-free QD growth and is close to enforce a VW island growth mode. Moreover, it is very likely that an intermixing via As-for-Sb exchange occurs at the GaAs/InGaSb interface [90], [91]: in this way, GaAs might become part of QDs. Hence, similarly to what has been found in Abramkin *et al.* [79], the intermixing with GaAs might lower the high strain between QDs and GaP,

[3]The aspect ratio of a QD is defined as the ratio of its heigth to its diameter.

bridging over the high mismatch and thus enabling the QD formation. The incorporation of parts of the GaAs interlayer into QDs finds confirmation in the TEM investigations on buried InGaSb QDs, where a contiguous GaAs layer beneath the QDs cannot be detected, as will be shown in sec. 3.3.

The GaAs interlayer thickness for the following growth experiments has been chosen in order to

1. obtain the highest QD aspect ratio which leads to a larger localization potential of QDs;
2. keep the strain generated by the GaAs coverage at minimum;
3. suppress formation of plastically relaxed islands.

Considering the previous discussion, a GaAs coverage of 5 ML fulfills these conditions, and has been therefore kept fixed at this value for all the following growth experiments carried out in this work.

3.2.3 QD formation: growth mode, critical thickness

The QD growth mode has been investigated by depositing an increasing amount of InGaSb as QD material on the GaAs/GaP surface. The AFM micrographs of free-standing QDs grown with different InGaSb amount are depicted in fig. 3.5, while fig. 3.6 shows a logarithmic plot representing the variation of the QD density towards the InGaSb coverage.

The critical layer thickness for the QD formation is determined to be $\sim$ 0.21 ML. At this coverage, the first 3D islands nucleate on the surface, with a density of $\sim 5 \cdot 10^9$ cm^{-2}, with lateral dimensions of (25 $\pm$ 5) nm and height of (1.6 $\pm$ 0.5) nm. Below the critical value of 0.21 ML, no QDs can be detected: the growth surface for sub-critical InGaSb coverage shows monolayer steps of a step-flow growth mode as shown in fig. 3.5 **(a)**. Then, QD density increases with the amount of deposited InGaSb reaching a maximum density of $\sim 2 \cdot 10^{11}$ cm^{-2} at 0.6 ML coverage. For an InGaSb coverage of 0.42 ML, QD density reaches $\sim 1.4 \cdot 10^{11}$ cm^{-2} and QDs are on average (28 $\pm$ 4) nm wide and (2.3 $\pm$ 0.4) nm high, respectively. For an InGaSb deposition of $\sim$1 ML, an additional nucleation of larger clusters with a density of $\sim 2.5 \cdot 10^7$ cm^{-2} is detected (width of (90 $\pm$ 5) nm and height of (6 $\pm$ 0.5) nm, as shown in fig. 3.5 **(d)**). The observed evolution of QD formation is a hallmark of a Stranski-Krastanow growth [11],[92] although an InGaSb coverage less than 1 ML cannot be referred to as a contiguous layer.

As also observed in the previous section, the GaAs interlayer contributes partly to the QD formation. Indeed, during the growth of the 5 ML-thick interlayer, elastic energy already builds up and the following deposition of a sub-ML amount of highly-mismatched InGaSb leads to an abrupt growth mode change from FM to SK, where the energy release is translated in formation of new facets and

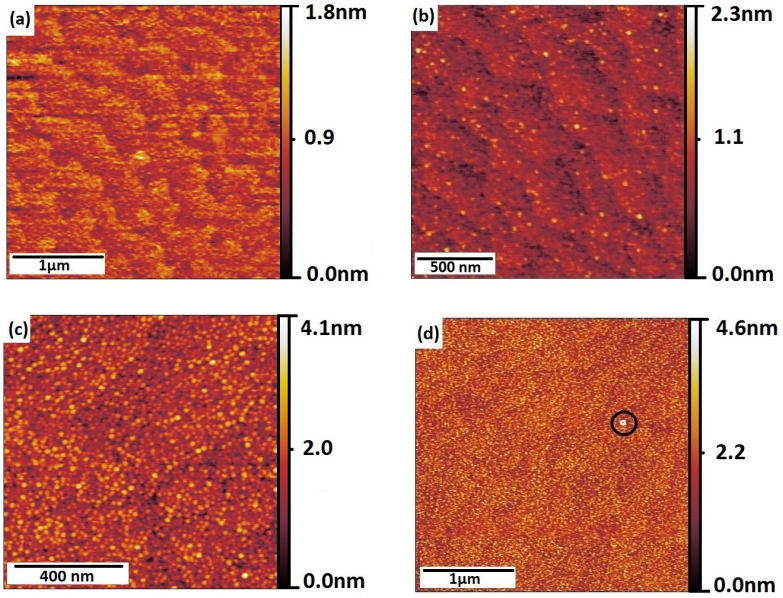

Figure 3.5: AFM micrographs of free-standing QDs grown with increasing InGaSb coverages. From top left: **(a)** 0.17 ML, **(b)** 0.21 ML **(c)**, 0.42 and **(d)** 1 ML, where also a cluster is detected, marked with a black circle. A 2s Sb-flush and 1s GRI have been used for all samples [78].

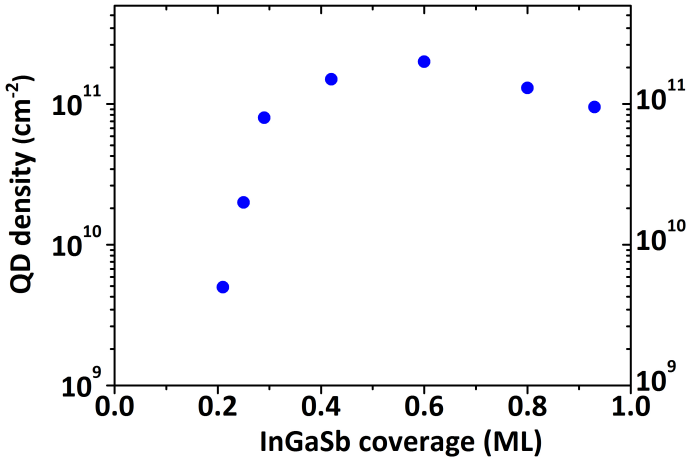

Figure 3.6: Logarithmic plot of the QD density trend for an InGaSb coverage between 0 and 1 ML [78].

edges, by means of 3D islands. The elastic energy density built up in a growing epilayer is directly proportional to the square of the in-plane strain $\varepsilon_{\parallel}$ (represented by the lattice mismatch between substrate and epilayer, see also Eq. 1.6 in sec. 1.1.2) and to the epilayer thickness d, and is given by [93]

$$E_{el,A} = 2 \cdot G \cdot \varepsilon_{\parallel}^2 \frac{1+\nu}{1-\nu} \cdot d \tag{3.1}$$

where G and ν are the shear modulus and the Poisson ratio of the epilayer, respectively. Here, the elastic energy accumulated in the interlayer contributes substantially to the energy needed for QD formation, and only 0.21 ML InGaSb are already sufficient for enabling the QD formation. As comparison: for the QD-system $In_{0.5}Ga_{0.5}As/GaAs/GaP$, a 0.52 ML InGaAs coverage on 2.2 ML GaAs was the critical thickness for QD formation [40]. At this value, the QDs showed sizes comparable to those of InGaSb here, but a lower density of $\sim 5{\cdot}10^7$ cm^{-2}, corresponding to two order of magnitude less then the present case, i.e. $\sim 5{\cdot}10^9$ cm^{-2}, where 5 ML GaAs + 0.21 ML InGaSb are grown. By using the Eq. 3.1, the elastic energy accumulated in the system GaAs interlayer + InGaAs or InGaSb QDs can be evaluated[4]. By comparing the elastic energies built up in the two systems, it can be found that 0.21 ML InGaSb + 5 ML GaAs accumulate 20-times more energy than 2.2 ML GaAs + 0.52 ML InGaAs. The thicker GaAs interlayer and bigger lattice parameter of InGaSb, compared to InGaAs, lead to a greater accumulation of elastic energy which relaxes elastically forming two order of magnitude more 3D islands.

3.2.4 Effect of a growth interruption

When a growth interruption (GRI) without any precursor supply is applied immediately after the QD deposition, the QDs undergo a well-known process in which material transfer between 3D islands occurs. As a consequence, the QD size increases and the density is reduced: this mechanism is referred to as *QD-ripening* [85],[86]. In fig. 3.7 AFM micrographs of free-standing InGaSb QDs with different GRIs are presented. With 1s GRI (fig. 3.7 **(a)**), QDs have lateral dimensions of (28 $\pm$ 4) nm and heights of (2.3 $\pm$ 0.4) nm with density of $\sim 1.5{\cdot}10^{11}$ cm^{-2}. As shown in the plot in fig. 3.7 **(d)**, with longer GRI the QD density decreases, while QDs grow bigger in size: after 400 s, the islands have diameter of (31 $\pm$ 7) nm and height of (3.5 $\pm$ 1) nm. For 800 s, lateral dimensions reach (33 $\pm$ 8) nm and height (4 $\pm$ 1.2) nm with density $\sim 8{\cdot}10^{10}$ cm^{-2}. These results demonstrate that a ripening process via material transfer between the QDs occurs. Furthermore, it is worth noticing that the low V/III ratio used during InGaSb QD formation ($\sim$ 0.3) clearly affects the temporal evolution of the 3D islands. Indeed, the V/III ratio is often used as parameter to control the QD size and density during ripening [87],[94]: a low V/III reduces the adatom

[4] The parameters of shear modulus and Poisson ratio can be found in [13].

diffusion length, leading to smaller and denser islands, compared to higher V/III ratios.

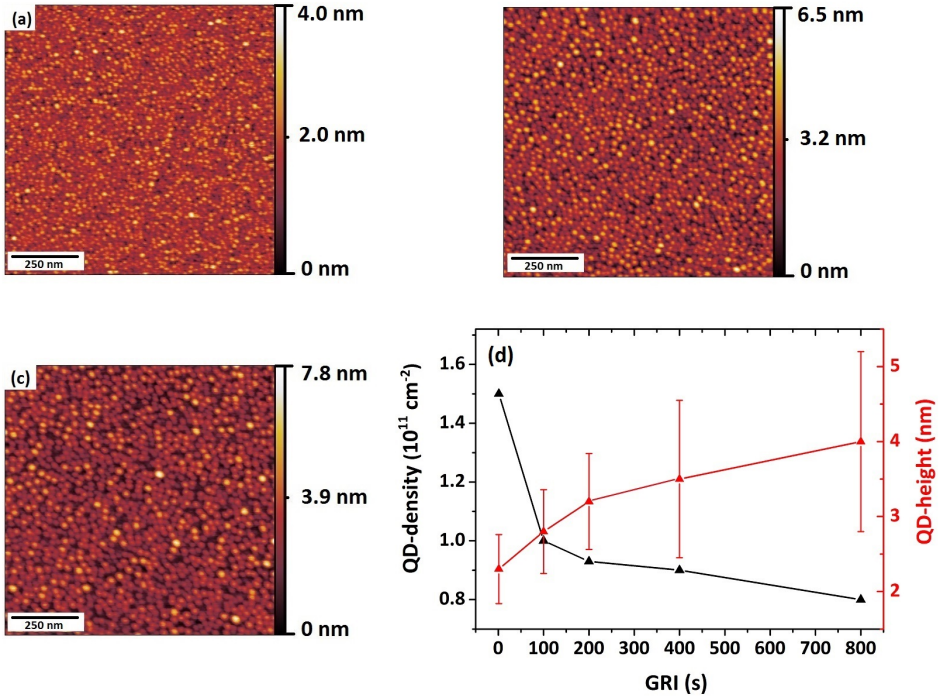

Figure 3.7: AFM micrographs of 0.51 ML InGaSb QDs with different GRI durations: **(a)** 1 s, **(b)** 400 s and **(c)** 800 s. In **(d)** the variation of QD-density and -height vs. GRI is depicted. 2 s Sb-flush has been used for all samples.

Here, the material transfer during the ripening process appears diminished over the extended GRI of 800 s. One reason for that can be the rather low V/III ($\sim$0.3) used during the QD growth. As comparison, Stracke *et al.* in [40] report that $In_{0.5}Ga_{0.5}As$/GaP QDs grown with a V/III of $\sim$ 5 exhibit defects after a GRI of 400 s. Additionally, as it will be seen in the next section, the use of Sb during the QD growth affects the surface diffusion, playing an important role in reducing the material transfer between the 3D islands. From these observations follows that the reduced V/III employed in InGaSb growth contributes to the reduction of defect formation during the ripening time, thereby leading to a more stable QD configuration.

3.2.5 Use of antimony-flush

As shown in sec. 3.2.1, a short Sb-soaking is employed after the growth of the GaAs interlayer and before the QD deposition, in order to start the Sb incorporation into QDs. Antimony belongs to the category of surface-active species,

also called *surfactants*. Although their microscopic impact on heteroepitaxial growth is still under debate, their use has been reported to affect morphology, composition and microstructure of epilayers. For the first time in 1989, Copel *et al.* [95] employed As as a surfactant to suppress island formation in the growth of Si/Ge/Si(001). Similarly, Sb has been largely used as surfactant, for example to modify surface reconstructions: the exposure of InGaP/GaAs(001) epilayers to an Sb flux modifies its reconstruction from (2 x 4)- to (2 x 3)-like [96]. An Sb-terminated GaAs(001) surfaces can be also obtained by exposing GaAs to an Sb flux [91]. This mechanism is attributed to the As-for-Sb anion *exchange reaction*, where Sb takes the sites of As, leading to a lowering of the surface energy [90]. On closer inspection, the reaction taking place at the Sb-exposed GaAs interface can be written as follows [90]:

$$GaAs\downarrow + \frac{1}{2}Sb_2\uparrow \rightarrow \ GaSb\downarrow + \frac{1}{2}As_2\uparrow \tag{3.2}$$

which leads to the formation of GaSb and molecular As in gaseous form. This process may apply also to the QD system studied in this work, since the GaAs interlayer is exposed to an Sb-soaking before the QD deposition. Hence, the GaSb resulting from this reaction can initiate the Sb incorporation into QDs. However, a deep understanding of this exchange and incorporation process occurring at the GaAs interface may be much more complex and would require a separated study.

Due to the above mentioned properties, the use of Sb can represent also a way for controlling the formation and electronic properties of QDs: through reduction of the surface energy and adatom surface diffusion, Sb-assisted QD growth can result in smaller and more homogeneous QDs, thereby suppressing the defect formation and increasing the QD density [98],[99],[100]. This effect has been observed in various QD system, as Ge QDs on Si [101] and InAs QDs on GaAs grown both in a MOVPE [102] and a MBE [103] environment. In this work, the influence of an Sb-flush on the InGaSb QD formation has been studied by varying the Sb supply time t_{Sb} before the QD material deposition. In fig. 3.8, three AFM micrographs of free-standing QDs are displayed, where different t_{Sb} are applied, ranging from 0 to 4 seconds.

In **(a)** QDs are grown without Sb-flush: the QD areal density is $\sim$6·10^{10} cm^{-2}, the QD diameter is of (35 $\pm$ 6) nm and the height of (2.6 $\pm$ 0.5) nm. Here, the large objects (marked with circles) are attributed to plastically relaxed QDs. These defects have a density of $\sim$10^{9} cm^{-2} and dimensions of (53 $\pm$ 3) nm and (3.2 $\pm$ 0.3) nm for width and height, respectively. Upon prolonging t_{Sb}, the formation of defective QD is reduced: for $t_{Sb} = 1$ s the QD density is decreased to $\sim$10^{8} cm^{-2}, and for $t_{Sb} \geq 2$ s the defect formation is completely suppressed. Simultaneously, QDs appear smaller and more uniform: in plot **(d)** the QD density and height versus t_{Sb} is presented: for 4 s flush, QDs have lateral dimensions of (24 $\pm$ 3) nm and height of (2 $\pm$ 0.3) nm, with density of $\sim$1.7·10^{11} cm^{-2}.

This investigation demonstrates that the use of an Sb-flush suppresses the island coalescence, while simultaneously increasing the QD density. This phenomenon is ascribed to the reduction of the adatom surface diffusion caused by Sb, as a consequence of the lowering of the surface energy. Hence, employing an Sb-*soaking* before depositing the QDs represents a way for easily controlling the QD structural properties. Additionally, its impact on the QD optical and electronic properties will be discussed in chapter 5.

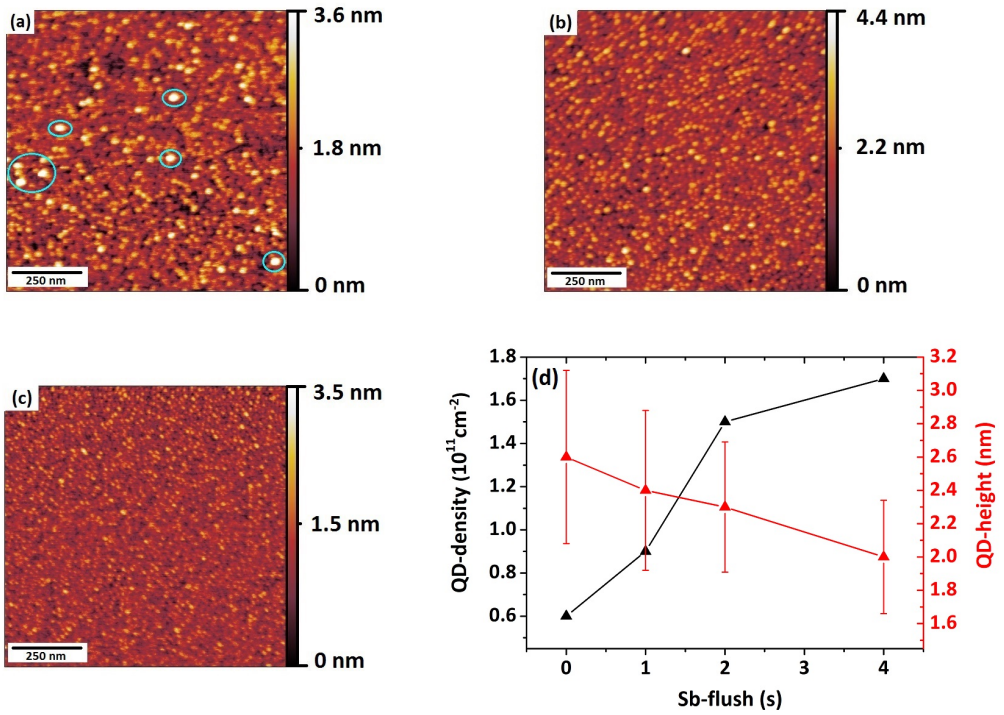

Figure 3.8: AFM micrographs of free-standing 0.51 ML InGaSb QDs, 1s GRI: without **(a)**, with 1s **(b)** and 4s **(c)** Sb-flush. In **(d)** the variation of QD density and height vs. Sb-flush duration is shown.

The use of an Sb-flush has been implemented also for $In_{0.5}Ga_{0.5}As/GaAs/GaP$ QDs. Here, the Sb exposure has been applied continuously during the entire duration of the QD growth. The experiment starts by depositing solely 2.3 ML $In_{0.5}Ga_{0.5}As$ QDs on ∼2.2 ML GaAs/GaP, as shown in fig. 3.9 **(a)**. The 2.2 ML GaAs interlayer represents the usual interlayer thickness used for the InGaAs QD growth [40],[84]. Thereafter, Sb has been additionally supplied during the growth of InGaAs, and the Sb/As molar flux ratio gradually increased. It is worth noticing that the As flux has been kept constant for every experiment, and only Sb has been varied. From figs. 3.9 **(b)**-**(d)** is evident that with increasing Sb

supply, the QD density decreases abruptly.

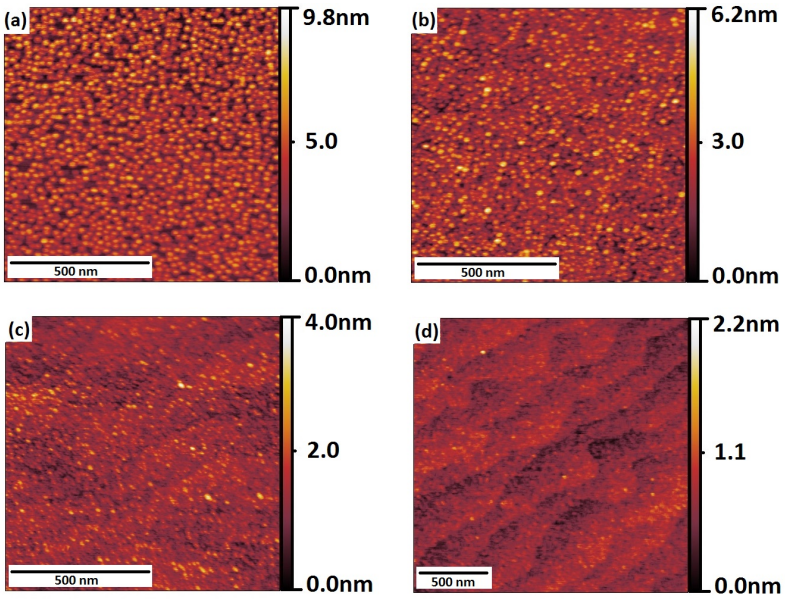

Figure 3.9: AFM micrographs of InGaAs(Sb)/2.2 ML GaAs/GaP QDs using different Sb/As molar flux ratios: **(a)** 0, corresponding to InGaAs QDs, **(b)** 0.1 **(c)**, 0.2 and **(d)** 0.3.

The plot of fig. 3.10 **(b)** displays the trend of the QD density with variation of the Sb/As ratio, from 0 to 0.1, corresponding to a TESb of 0 - 7.7 μmol/min. In this range, the QD density decreases of 3 orders of magnitude, from $\sim 10^{11}$ to $\sim 10^{8}$ cm^{-2}, respectively. If the Sb supply is further increased, a complete suppression of island formation occurs, and no QDs are detected anymore: here only monolayer steps of a step-flow growth can be observed, as shown in fig. 3.10 **(a)**.

This outcome demonstrates that, also for $In_{0.5}Ga_{0.5}As$ QDs, Sb strongly inhibits the QD nucleation, even if it is supplied during the entire QD growth step. From this observation follows that the suppression of the island coalescence does not depend on the QD stoichiometry, but is rather an independent property of Sb. The additional Sb supply during QD growth can be therefore used as a tool to adjust the QD structural properties.

3.3 Structural investigations on buried InGaSb QDs

In order to get a microstructural insight into the material distribution of the QD region, structural investigations, by means of Transmission Electron Microscopy (TEM), have been carried out on buried InGaSb/GaAs/GaP QDs [78]. Fig. 3.11

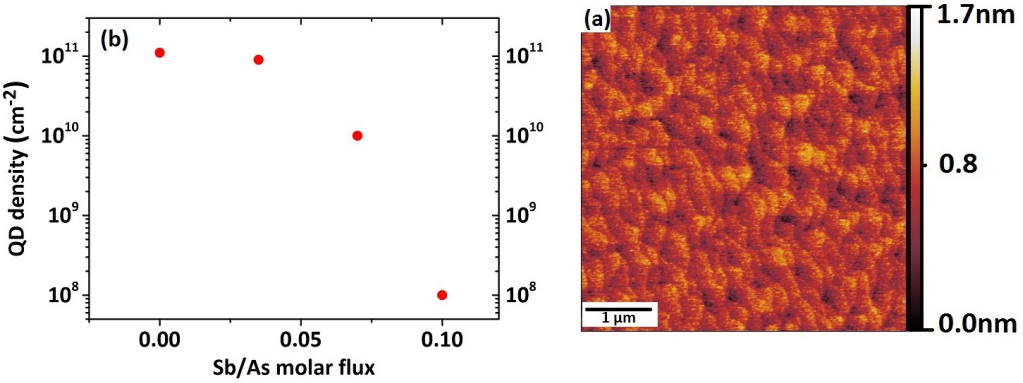

Figure 3.10: **(a)** The density trend of InGaAs(Sb)/2.2 ML GaAs/GaP QDs towards the Sb/As ratio. **(b)** AFM micrograph of the 2.2 ML GaAs/GaP surface, where an Sb/As molar flux ratio of $\sim$ 0.2 is used. No QDs can be observed, the surface shows instead ML-steps of a step-flow growth.

(a) and **(b)** shows cross-sectional TEM micrographs, as diffraction and phase contrast, respectively. Both images were acquired under strong-beam bright field conditions.

The micrograph shown in fig. 3.11 **(a)** was taken along the [010]-zone axis of the specimen, tilted of 6° in respect to the electron beam direction to avoid an overlap of the QDs, as also schematically indicated in the depiction. In this way, it is possible to have a projected view over the QD plane and estimate their density ($\sim$7·10^{10} cm^{-2}, which agrees with the AFM results). The different material composition between QDs and GaP leads to a diffraction contrast, from which the QDs appear dark with respect to the bright background, represented by the GaP. The same QDs are shown in fig. 3.11 **(b)** as a zone-axis high-resolution TEM (HRTEM) micrograph. From both micrographs, QDs appear dislocation-free; in fact, the diffraction conditions used for such investigations are sensitive to the typical dislocations in fcc-structures. The micrograph depicted in fig. 3.12 was recorded again along the [010]-zone axis and shows the amplitude signal of a Fourier-filtered (200)-reflection. Here, two single QDs (dark regions) can be clearly detected and the resulting contrast represents a material concentration map.

The material composition of QDs cannot be inferred from this investigations: only variations in the electron density can be distinguished: the QDs appear indeed darker with respect to the surrounding matrix. These two QDs show a truncated-pyramid shape, which is usually found in buried cubic QDs [104]. Their lateral dimensions are of 15 nm (for the base) and 2.5 and 1.5 nm for the height, respectively. It is worth noticing that the QD lateral dimensions appear here smaller with respect to the AFM measurements: in fact, only an upper size limit can be inferred from the AFM, that normally overrates the QD lateral size

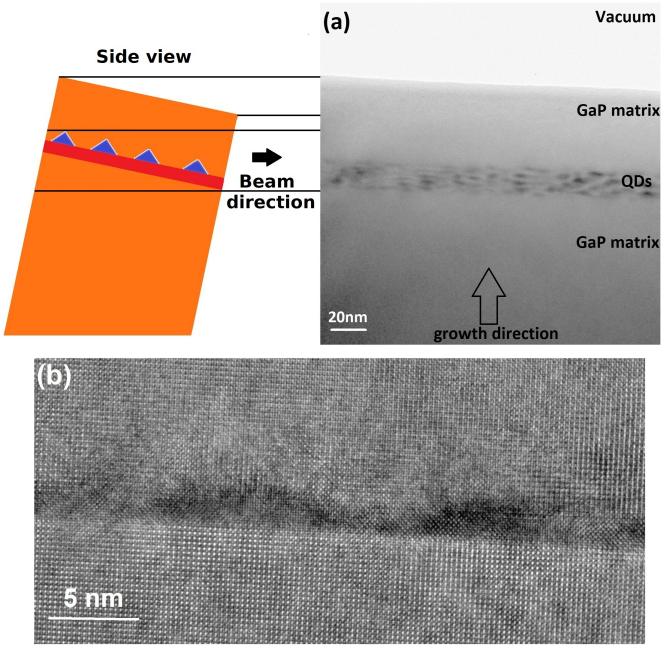

Figure 3.11: **(a)** Cross-sectional TEM micrographs of 0.42 ML InGaSb QDs on 5ML GaAs/GaP, with 1s Sb-flush, and capped with 6 nm GaP. The specimen has been tilted to better display the QD plane. The growth direction is also indicated. **(b)** HRTEM micrograph: two QDs are clearly detectable [78].

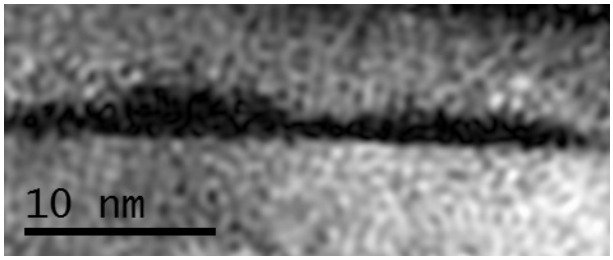

Figure 3.12: Amplitude signal of a Fourier filtered (200)-reflection of a HRTEM image of single QDs: 0.42 ML InGaSb on 5ML GaAs/GaP capped with 6 nm GaP. The QDs are represented by the region of dark contrast [78].

due to convolution of the sample surface with the AFM tip shape.

In fig. 3.13 another high resolution cross-sectional TEM image[5] of the QD region is shown and again, the QDs appear as dark contrast with respect to the GaP matrix. Interestingly, from the TEM investigations presented so far, no GaAs interlayer beneath the InGaSb QDs can be identified. This would thus confirm the assumption that the GaAs becomes partly incorporated into QDs during QD formation. Indeed, the dependence of QD morphology on GaAs interlayer thickness of fig. 3.4 exhibits an increase of QD density and aspect ratio with thicker interlayer, suggesting embodiment of parts of GaAs into QDs.

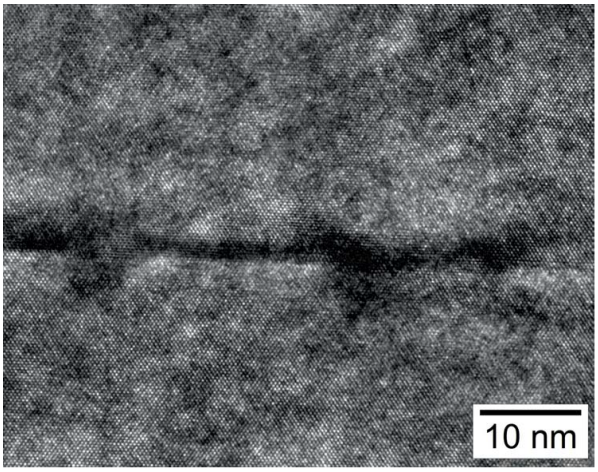

Figure 3.13: High resolution TEM image of 0.51 ML InGaSb QDs, 1s GRI, capped with 6nm GaP. The QDs appear as dark contrast areas. The 5 ML GaAs cannot be resolved as a contiguous layer anymore.

[5]Also in the submitted paper: E. M. Sala, F. Arikan, L. Bonato, F. Bertram, P. Veit, J. Christen, A. Strittmatter, and D. Bimberg, *MOVPE growth of (In,Ga)Sb/AlP/GaP(001) quantum dots for nanoscale memory applications.*

Summary

- The growth of InGaSb QDs on GaP has been studied in detail. The QD growth is enabled by using a few-ML-thick GaAs interlayer prior to InGaSb material deposition, similarly to $In_xGa_{1-x}As$ QDs on GaP. The QD growth follows a typical Stranski-Krastanow mode. The dependence on the GaAs interlayer thickness of the QD formation suggests an incorporation of a given amount of interlayer into the QDs. This assumption finds confirmation in the microstructural investigations by means of TEM, where a contiguous GaAs interlayer lying beneath the QDs cannot be revealed.

- The effects of a GRI applied after QD formation are studied: with increasing interruption time, QDs increase their size while reduce their density. A lower V/III ratio during QD formation prevents the formation of defects, reducing the material transfer rate between the 3D islands, and a more stable QD configuration can be reached.

- The role of an Sb-soaking on QD formation has been studied. Sb suppresses the island coalescence, due to a reduction of surface energy and adatom migration length. This leads to shrinkage of the QD sizes and a reduction of defect formation. Therefore, the Sb-flush can be also used as a tool to modify the QD structural properties.

- TEM structural characterization on buried QDs detect dislocation-free QD-structures having a truncated-pyramid shape typical of buried QDs.

Chapter 4

Towards the non-volatility limit

"The secret of change is to focus all your energy, not fighting the old, but on building the new."

Socrates

This chapter gives an insight on the DLTS technique for determination of localization energy and capture cross-section of holes trapped in InGaSb/GaP QDs. After discussing the QD heterostructures properties leading to longer retention times, experimental details on DLTS sample preparation and measurement will be presented.

4.1 Adjusting the properties of QD heterostructures for longer storage times

The storage time for holes in QDs depends primarily on the depth of the localization potential provided from QDs, and on their capture cross-section σ_∞, which measures the scattering probability of free holes from the host material into QDs. In previous measurements, the capture cross-section has been observed to vary over six orders of magnitude for a given hole localization energy, i.e. from 10^{-15} to 10^{-9} cm^2 [59],[64]. Fig. 4.1 shows the hole storage times obtained so far for various QD heterostructures towards their localization energies, with varying cross-section. The black points represent the experimental values: the first one corresponds to the earliest result at room temperature for holes captured in InAs/GaAs QDs, which amounts to $\sim$0.5 ns [16]. By employing an additional $Al_{0.9}Ga_{0.1}As$ barrier, their storage time increases to 1.6 s [105]. A considerable improvement in the retention time is obtained by replacing the GaAs matrix material with GaP[1]: for $In_{0.5}Ga_{0.5}As$/AlP/GaP QDs, a storage time

[1] Up to $\sim$700 meV in the localization potential can be gained by using GaP instead of GaAs [106].

of 230 s at room temperature is reached [107]. To date, the longest storage time has been measured for MBE-grown GaSb/GaP QDs, which amounts of about 4 days [82]. In parallel, the InGaSb/AlP/GaP QDs studied in this work exhibit ∼1 hour retention time, corresponding to a localization energy of 1.15 eV (indicated in red in fig. 4.1), that represents to date the record for MOVPE-grown QDs.

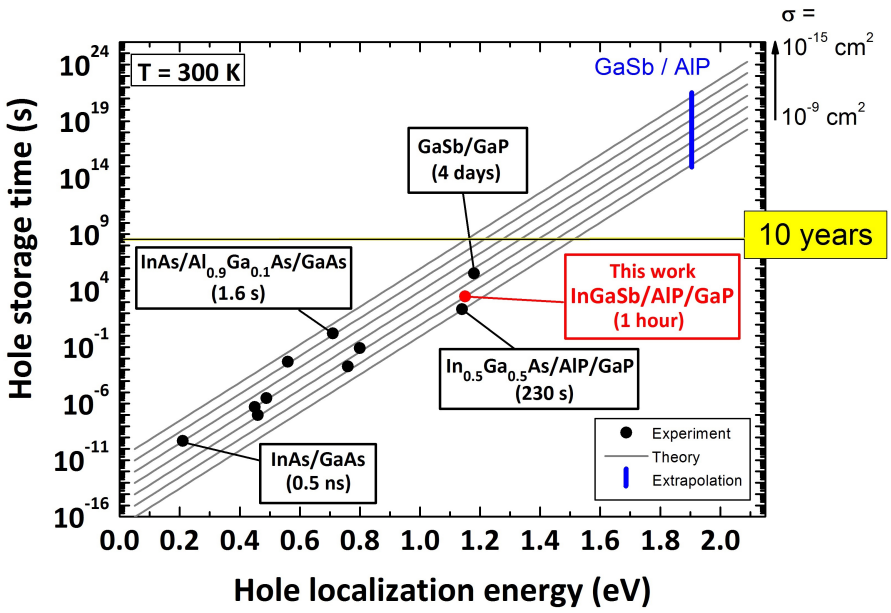

Figure 4.1: A roadmap of hole localization energy vs. storage time for different III-V-based QD material systems at T = 300 K. The theoretical trend of the storage time for varying values of the capture cross-section is indicated with grey lines, while the black points represent the experimental results. The vertical blue mark displays the theoretical expectation for the material combination GaSb/AlP. After [64],[108].

Ideally, the ultimate non-volatile QD-Flash should show retention times equal or greater than 10 years. Three important parameters of the QD heterostructures strongly influence the storage time and can be adjusted:

1. Localization potential of QDs As mentioned in sec. 1.1.3, type-II QDs exhibiting hole confinement are preferred for nanomemory applications, as the valence band discontinuity (VBO) is maximized. Indeed, they lead to a higher localization energy and to an increased storage capacity for single QD, with respect to type-I heterostructures [12],[66]. Among type-II structures, antimony-based QDs naturally provide a large localization potential and are therefore considered to be the best candidates as building blocks for the future QD-Flash. Additionally, an important role plays by the choice of the matrix material to

provide even larger discontinuity of the valence bands. For instance, by replacing GaP with AlP as matrix material, additional ∼500 meV in localization energy can be gained, thereby further increasing the retention time of the QD heterostructure. Theoretical calculations yielded for GaSb QDs embedded in an AlP matrix a localization potential of ∼1.9 eV [109] (also indicated by the blue mark in fig. 4.1), corresponding to a storage time of billions of years.

2. Additional AlP barrier An additional AlP barrier placed below the QDs aims to increase the localization energy of holes in the QDs of about ∼500 meV[2], and therefore improve their storage time. It hampers the hole emission, while not affecting their capture [64]. For the QD system $In_{0.5}Ga_{0.5}As/GaP$, the use of an additional barrier has effectively enhanced the retention time by ∼500 meV [107]. It is worth noticing, that the very small lattice mismatch of $\sim 0.02\%$ between the AlP barrier and the GaP matrix [13] enables the use of an AlP layer without generating much strain in the DLTS structures.

3. Capture cross-section The QD capture cross-section depends on many physical parameters, like QD geometry and QD interaction with the surroundings, including Auger scattering and coupling to phonons [64]. A systematic cross-section engineering would represent a valuable tool for extending the hole retention time in QDs, as the capture cross-section varies over six order of magnitude for a given hole localization energy. For instance, the measured localization energy $E_{loc} = 1.15$ eV for the InGaSb QDs studied in this work would already suffice for non-volatility, provided that the capture cross-section be reduced to $\sigma_\infty = 10^{-14}$ cm^2. A cross-section engineering is in practice achieved by acting on the structural and electronic properties of the QDs through control of the QD parameters. The QD growth conditions can be adjusted in order to modify the QD size, composition and density. In the previous chapter, the Sb-flush and the GRI have been found to remarkably affect such QD properties: a prolonged GRI yields bigger QDs, while an Sb-flush reduces the QD size. It is important to notice that increased QD dimensions would increase the QD localization potential [23] at expense of the cross-section, while a reduction of QD dimensions would decrease both the cross-section and the QD localization depth. Hence, to successfully employ a cross-section engineering, all such combined effects must be taken into account. Up to now, an effective technique aiming to model the impact of the QD properties and the QD interactions with the matrix on the capture cross-section has not yet be developed: further investigations are needed in this direction.

[2] Experimental values for the VBO of GaP/AlP heterostructures lie in the range of 0.34 – 0.69 eV, as reported by Vurgaftman and Meyer in [13], Sec. **E**.

4.2 DLTS structure preparation: a novel precursor for the GaP p-doping

For the DLTS measurements, dedicated structures have been fabricated: a typical DLTS structure consists of a n^+-*p*-diode, with QDs embedded in the *p*-doped region of the GaP matrix. The *p*-doping has been carried out by using carbon as an alternative *p*-dopant for GaP. Up to now, Zn has been normally used for this purpose [110]-[114], but important side effects have been reported, as for:

- the so-called *memory effect*, which occurs when the precursor supply is stopped, but the dopant becomes incorporated into the growing epilayer for a certain time after the end of its supply;
- a high diffusivity: Zn diffuses through the growing epilayer exhibiting accumulation in the neighboring regions [115][3]. Both the memory effect and the high diffusivity of Zn prevent to achieve abrupt interfaces and a sharp doping profile, which is of fundamental importance for the correct functionality of the DLTS structure fabricated in this work (and in general of electronic devices);
- a high ionization energy of Zn, amounting to $\sim$70 meV [120]. This leads to a lower density of free holes than the nominal doping concentration, at low temperatures, because of the difficulty of ionizing the acceptors. This issue prevented to carry out more sensitive DLTS measurements on $In_{0.25}Ga_{0.75}As$/GaP QDs in [84] by means of charge-selective, where less charge carriers are involved.

The use of C as *p*-dopant for GaP provides important advantages over Zn:

- the absence of any memory effect and a lower diffusivity compared to Zn, based on investigations on GaAs [121]-[123], as to date no studies of carbon diffusion in GaP are reported, and
- the greater availability of free holes even at low temperatures, as the carbon ionization energy in GaP is lower than the one of Zn, i.e. $\sim$50 meV [120].

Such adavantages can remarkably benefit the performances of the DLTS devices, leading to more abrupt *n*-*p* interfaces and avoiding any contamination of the QD layer embedded in the *p*-region of the DLTS structure. Additionally, the more sensitive charge-selective DLTS measurements can be carried out trouble-free.

Different carbon sources can be used as C-precursors, such as CBr_4, CCl_4, or the novel CCl_3Br, i.e. *carbon trichloro-bromide*. Unfortunately, no recent studies

[3] The mechanism of memory effect and high-diffusivity of Zn have been extensively studied for both GaP [110]-[114], and GaAs [116]-[118],[119].

on the intentional carbon doping of GaP have been reported in literature[4], so that a direct comparison between the use of the different precursors available on the market cannot be made. For this reason, recent investigations on C-doped GaAs will be considered as reference. The use of the novel CCl_3Br in GaAs has shown the advantage of suppressing the *in-situ* etching [125],[126], observed otherwise when employing CBr_4 and CCl_4, which leads to an unstable growth rate [127]-[129]. Different physical-chemical mechanisms are responsible for such etching mechanism, as the removal of As by HBr (resulting from the CBr_4 decomposition) [127], or by formation of GaCl in the vapor phase via reduction of Ga species [129]. However, the precise mechanisms underlying the *in-situ* etching are still under debate, and their deep understanding goes beyond the purpose of this discussion. To avoid any side effects of such precursors, the carbon source CCl_3Br has been chosen as precursor for carrying out the *p*-doping of GaP epilayers.

For the fabrication of DLTS structures, a low *p*-doping of $\sim 10^{16}$ - 10^{17} cm^{-3} is required, to allow the depletion zone to penetrate up to the QD layer at the relatively low voltages used in the DLTS measurements. In order to determine the desired doping concentrations, a sample set with varying CCl_3Br supply has been fabricated. All samples were grown on semi-insulating GaP (001). The CCl_3Br molar flow has been varied from 0.6 to 16 μmol/min. The growth parameters used for the C-doped epilayers are the followings: $T_g = 620°C$, V/III ratio of $\sim$ 13, TEGa and TBP molar fluxes of $\sim$25 and $\sim$340 μmol/min respectively, and growth rate of $\sim$1 μm/h. The samples have been electrically characterized by using the Van der Pauw method [130], which allows for the estimation of the doping type, the carrier concentration and the mobility of charge carriers. In fig. 4.2 the free hole concentration n_h is plotted as a function of the CCl_3Br molar flow at T = 300 K.

The data clearly show that the carrier concentration increases linearly over the measurement range, from $3{\cdot}10^{16}$ to $8{\cdot}10^{17}cm^{-3}$, as also indicated by a linear fit. In the inset, the Hall mobility is plotted against the hole concentration. As the free carrier concentration increases, the carrier mobility decreases: this is a typical behavior due to the increased ionized impurity scattering[5] [131]. By comparing these results with usual values for the mobility of GaP:C [124], they find good agreement. For instance, for n_h in the range of $\sim 5{\cdot}10^{16}$ - $8{\cdot}10^{17}cm^{-3}$, hole mobilities between 289 and 100 $cm^2/V{\cdot}s$ for GaP:C are measured, which agree very well with the reported experimental values. Furthermore, an interesting comparison can be made with the use of CCl_3Br in GaAs, investigated by Bhunia *et al.* in [125]: there, similar molar flows, T_g and V/III have been used as in this work, but a $\sim$2.5 orders of magnitude greater hole concentration has been obtained. Since from the observed trend of fig. 4.2 an electrical carbon self-compensation mechanism can be largely excluded, it might be speculated that

[4] Only one minor study of intentional C-doping of GaP can be found (see D. P. Bortfeld *et al.*, 1971 [124]), where a propane doping source was used.

[5] The ionized donors and acceptors act as Coulomb scatterers after releasing their charges. This is likely to inhibit the motion of charge carriers.

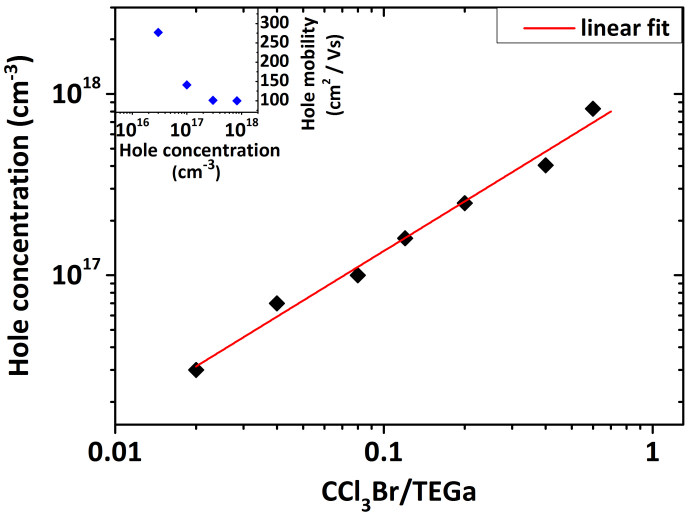

Figure 4.2: Dependence of hole carrier concentration n_h on room temperature mobility. In the inset, n_h is plotted towards the hole mobility.

carbon has a poorer incorporation efficiency in GaP compared to GaAs. This means that, for GaP, a greater amount of CCl_3Br has to be supplied to the reactor to obtain a comparable doping concentration as for GaAs.

4.2.1 Surface morphology

The surfaces of carbon-doped GaP epilayers have been investigated by using a Nomarski phase-contrast optical microscope. In fig. 4.3 micrographs of four epilayers grown with different doping concentrations, varying from $3{\cdot}10^{16}$ to $8{\cdot}10^{17}$cm^{-3}, are presented and refer to the samples electrically characterized in the previous section. The lowest *p*-doped sample (fig. 4.3 **(a)**) shows a mirror-like surface exhibiting some hillocks, with lateral dimensions between $\sim$10 and $\sim$25 μm and an areal density of $2{\cdot}10^3$ cm^{-2}. Their size remain almost unchanged with increasing CCl_3Br molar flux, whereas their density increases up to $5{\cdot}10^4$ cm^{-2} (fig. 4.3 **(c)**). With increasing hole concentration, i.e. of $8{\cdot}10^{17}$ cm^{-3}, the surface morphology degrades, as can be seen in fig. 4.3 **(d)**, where additional small pits are detected. The surface hillocks might be ascribed to impurity microprecipitates of the dopant element, while the small pits to microstrain arising from such precipitates, similarly to what has been observed by Iizuka *et al.* for doped GaAs [132] and GaP [133][6]. A further increase of the CCl_3Br flux leads to a very poor surface morphology, which can be detrimental for the

[6]For a better comprehension of such mechanism further and more appropriate investigations are required, as for dedicated etching techniques and electron probe microanalysis, as carried out by Iizuka *et al.* in [132].

correct functionality of the DLTS structures. However, as already pointed out, for the purpose of this work the doping region between 10^{16} and 10^{17} cm^{-3} is of interest (see also sec. 4.3.1), and for such doping concentrations a good surface morphology is obtained.

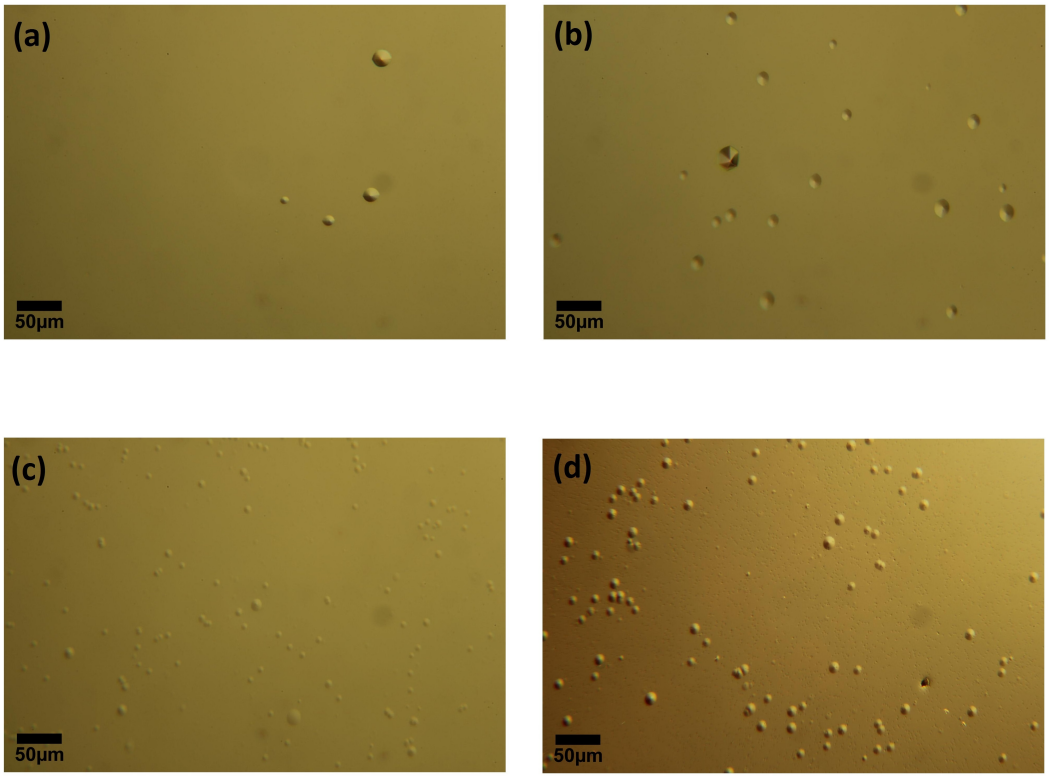

Figure 4.3: Nomarski micrographs of C-doped GaP(001) epilayers with nominal thickness of 2 μm, grown with increasing CCl_3Br molar fluxes. From up left (corresponding doping concentrations are also indicated): **(a)** 0.6 μmol/min, 3·10^{16} cm^{-3}, **(b)** 1.1 μmol/min, 8·10^{16} cm^{-3}, **(c)** 6 μmol/min, 3·10^{17} cm^{-3}, and **(d)** 16 μmol/min, 8·10^{17} cm^{-3}.

4.3 Measuring retention time in QDs: Deep Level Transient Spectroscopy (DLTS)

In this section, the Deep-Level Transient Spectroscopy (DLTS) method used for determination of activation energies and capture cross-section of InGaSb/GaP QDs is discussed. Originally, the DLTS technique has been employed to determine deep levels (traps) caused by defects or impurities in semiconductors [65]. Indeed, QDs can be treated as traps storing charge carriers for a certain time and can be therefore investigated by using this technique, which allows for a detailed study of carrier dynamics and energy levels of QDs.
The storage time τ for holes in QDs can be expressed as the inverse of the thermal emission rate e_a for holes from QDs [97][7]:

$$\frac{1}{\tau} = e_a = \gamma T^2 \sigma_\infty \exp\left(-\frac{E_a}{k_B T}\right) \tag{4.1}$$

where E_a is the activation energy for holes, k_B the Boltzmann constant, T the temperature, σ_∞ the capture cross-section for $T = \infty$, and γ a constant depending on the hole effective mass and degeneracy of hole states (relies on the considered host material [134]). E_a represents the energy barrier that holes need to surpass in the emission process and σ_∞ measures the scattering probability of holes with the surrounding matrix, which depends on many physical parameters, as the QD geometry and the QD interaction with the surroundings [12]. Hence, the storage time τ depends solely on E_a and on σ_∞.
The DLTS method is a capacitive technique, thus a simplified sample structure, in form of a n^+-p-diode can be used for the measurements, instead of a whole QD-Flash prototype. The usual work cycle of a DLTS measurement is shown in fig. 4.4. The measurement starts by applying a bias voltage V_m so that the depletion region is extended over the QD layer and the QDs are empty (discharged), and situated below the Fermi level (fig. 4.4 **(a)**). After applying a pulse voltage V_p, the QD are charged with holes (fig. 4.4 **(b)**). After all energy levels of the QDs are filled, the voltage is returned to the initial value V_m: the holes states are now below the Fermi level and the QDs are discharged, and this induces hole emission (thermal activation). The emission process is detected via time-resolved measurement of the capacitance transient $C(t)$. In general, the recorded $C(t)$ from a single emission is mono-exponential, with an emission time constant τ and is given by [135]:

$$C(t) = C(\infty) - \Delta C_0 \exp\left(-\frac{t}{\tau}\right) \tag{4.2}$$

[7] The hole tunneling emission from QDs can be neglected [63].

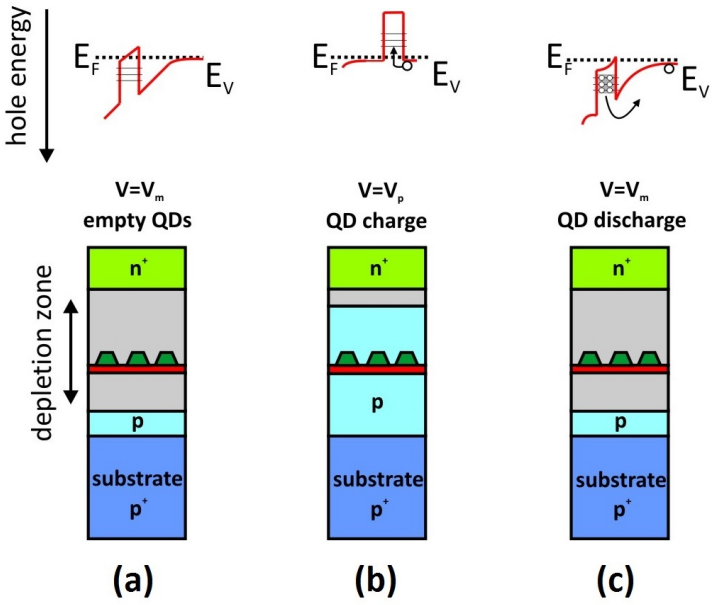

Figure 4.4: Schematic illustration of a DLTS cycle for a n^+-p-diode. The upper part shows the band diagram corresponding to the three stages of the DLTS measurement: **(a)** equilibrium state before the bias pulse, **(b)** QD charge during and **(c)** after the bias pulse. E_F and E_V represent the Fermi level and the valence band edge respectively.

where $C(\infty)$ is the *steady-state* capacitance at V_m and ΔC_0 is the overall change in $C(t)$ for $t = \infty$ (capacitance of the n^+-p-junction considering completely charged QDs). It is important to point out that the capacitance transients of QDs are not mono-exponential, due to ensemble effects exhibiting inhomogeneous broadening [135]. Therefore, the measurement cycle is repeated for several temperatures. To evaluate the activation energy E_a, the cross-section σ_∞ and an emission constant τ, the rate-window concept (double-boxcar method [136]), with a reference time constant τ_{ref} is used, thereby investigating an emission process in a given time. The DLTS signal is obtained by the capacitance difference at two different times t_1 and t_2, at a certain temperature T:

$$D(T, t_1, t_2) = C(T, t_2) - C(T, t_1) \tag{4.3}$$

Substituting Eq (4.2) in (4.3), it can be obtained:

$$D(T, t_1, t_2) = \Delta C_0 \left[\exp\left(-\frac{t_2}{\tau(T)}\right) - \exp\left(-\frac{t_1}{\tau(T)}\right) \right] \tag{4.4}$$

where t_1 and t_2 define the rate window with τ_{ref} given by:

$$\tau_{ref} = \frac{t_2 - t_1}{\ln\left(\frac{t_2}{t_1}\right)} \tag{4.5}$$

The DLTS spectrum is obtained by plotting $D(T, t_1, t_2)$ towards T, as shown in fig. 4.5.

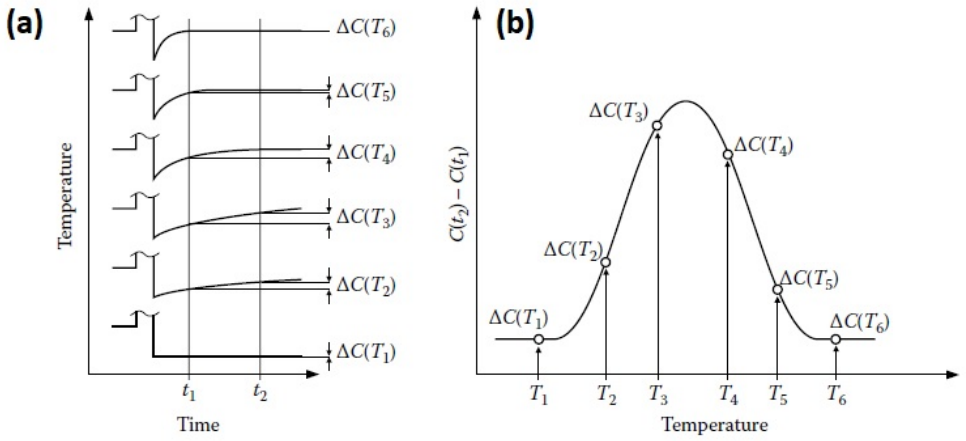

Figure 4.5: **(a)** Example of capacitance transients of a thermally activated emission process recorded at different temperatures T_i for a given rate window $t_2 - t_1$.**(b)** DLTS chart resulting from plotting the capacitances $C(T, t_2) - C(T, t_1)$. From [58].

The analysis of the capacitance transients with different time reference constants τ_{ref} gives an ensemble of spectra, each one corresponding to a certain temperature. From the maximum values of these spectra, coupled values of τ_{ref} and T are obtained and used for the calculation of the activation energy and storage time. By applying the natural logarithm to Eq. (4.1), it can be obtained:

$$\ln(T^2 \tau_{ref} \gamma_h) = \frac{E_a}{k_B T} - \ln(\sigma_\infty) \tag{4.6}$$

By using the Arrhenius analysis and plotting $T^2 \tau_{ref} \gamma_h$ against $1/T$, the activation energy and capture cross-section can be extracted via linear fit, where E_a represents the slope and σ_∞ the intercept of the fit. The storage time instead is extrapolated by using Eq (4.1), substituting the value of E_a and σ_∞ found previously.

4.3.1 Electrical characterization

For electrical characterizations, three dedicated DLTS samples have been fabricated:

- one containing the GaAs interlayer and InGaSb QDs ("*only-QDs*");
- one with QDs and an additional AlP layer ("*QD-barr*");
- a reference containing only the AlP layer ("*only-barr*").

which are in form of n^+-*p*-diodes, as schematically depicted in fig. 4.6. They are grown on *p*-doped GaP (001) substrates, having nominal p-doping of $\sim$1.5·10^{18} cm^{-3} (serving also as back-contact for the processing). The first segment of each diode consists of $\sim$300 nm thick carbon-doped GaP buffer layer, with a carrier concentration of $\sim$5·10^{16} cm^{-3}.

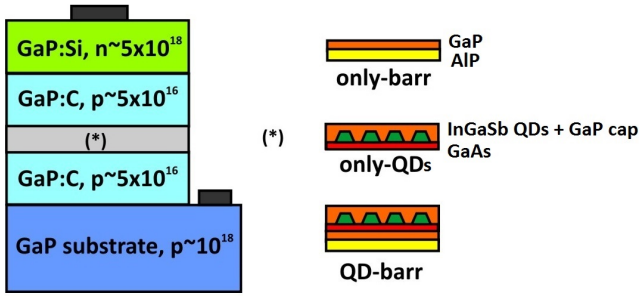

Figure 4.6: Design of the three DLTS structures. The asterisk indicates the different types of layer structure containing, from top right, only the AlP barrier, only QDs, or QDs + AlP.

For samples *only-barr* and *QD-barr*, a $\sim$20 nm AlP layer beneath the QDs is employed, which acts as an emission barrier for charge carriers in the QDs (growth temperature $T_g = 800$°C) and is overgrown with a thin GaP layer ($\sim$2 nm). When the barrier is used, the localization energy E_a is given by the sum of the E_a of QDs and the height of the AlP barrier. The GaP thin capping, instead, is used to protect AlP from adsorbing impurities during the cooling down step preceding the QD growth. Thereafter, the GaAs interlayer and the QDs are grown and capped with 6 nm undoped GaP, at $T_g = 500$°C. They are followed by a $\sim$500 nm GaP *p*-layer having the same carrier concentration as the buffer. The upper segment of the diode consists of a highly *n*-doped GaP layer ($\sim$5·10^{18} cm^{-3}), serving as top-contact layer, where Si is used as dopant.
The electrical characterization consists of static capacitance spectroscopy (C-V profiling) [97], [137] and time-resolved capacitance spectroscopy as DLTS. Since hole localization in the QDs stores the capacitance within the p-n junction, C-V profiling can be used to determine the voltages at which holes are captured into

and released from the QDs [137], thereby defining the interval of interest for the DLTS measurement.

The *conventional* DLTS measurement returns the average value of the activation energy over all bound states of the QDs (i.e. the *mean*, *ensemble* activation energy). Instead, the *charge-selective* DLTS [138] has been performed to determine the activation energy of the hole ground state, which is referred to as *hole localization energy*, meaning the energy difference between the hole ground state and the valence band edge of the surrounding matrix material. In charge-selective DLTS, the measurement and pulse voltages are increased in small steps across the measurement interval, so that only one of the internal levels of the QDs is involved in each measurement step: ideally, one hole per QD enters and leaves the QD in each DLTS cycle. The charge-selective measurement has been carried out with different reverse biases, so that all QD internal levels are probed. It is important to point out that also an energy-broadened QD ensemble can be measured by charge-selective DLTS, as it permits to investigate the emission from many charge carriers all having the same activation energies.
For all samples and measurements, the temperature has been swept from 50 K to 400 K, in steps of 5 K. For conventional DLTS measurements, the reverse bias V_m has been set to 6 V and the pulse bias $V_p = 0$ V, whereas for charge-selective DLTS, $V_p = V_m - 1$ V and V_m between 1 V to 6 V. The capacitance transients are measured at a frequency of 1 MHz and an AC voltage of 100 mV. The pulse length has been chosen so that the charging process is completed at all temperatures. For *only-QD* sample, the pulse length is 0.2 s and the measurement time 1.8 s, while for *only-barr*, 0.5 and 2.5 s, and for *QD-barr*, 2 and 8 s. The reference times τ_{ref} for all samples ranges between 0.5 s and 5 s. The capacitance transients of the *conventional* DLTS on the three investigated structures are shown in fig. 4.7[8].

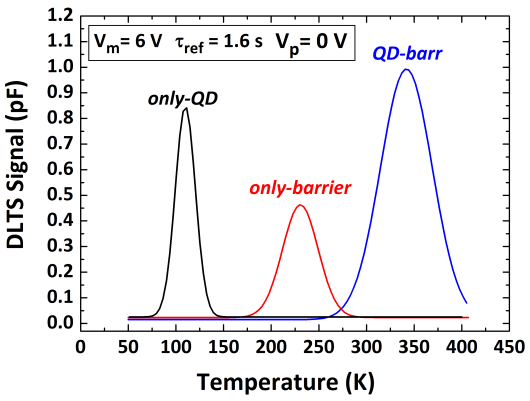

Figure 4.7: Conventional DLTS spectra of the three different n^+-p-diodes of fig. 4.6.

[8] Also in the submitted paper: E. M. Sala, F. Arikan, L. Bonato, F. Bertram, P. Veit, J. Christen, A. Strittmatter, and D. Bimberg, *MOVPE growth of (In,Ga)Sb/AlP/GaP(001) quantum dots for nanoscale memory applications.*

The peak of *only-QD* is centered around 110 K, that of sample *only-barr* around 230 K, while for *QD-barr* it appears at higher temperatures: between 280 K and 400 K. This suggests a larger localization energy than that of *only-QD*, as expected from the presence of the additional AlP barrier. The sample containing only QDs shows the smallest activation energy: E_a= (0.298 $\pm$ 0.006) eV. For *only-barr* the activation energy represents the height of the energy barrier formed by AlP on GaP and amounts to (0.63 $\pm$ 0.01) eV, in agreement with the value reported in literature, ranging between 0.34 and 0.69 eV [13]. The E_a for *QD-barr* has been determined to be (0.86 $\pm$ 0.02) eV, which is consistent with the sum of the activation energies of *only-QD* and *only-barr*, i.e. (0.92 $\pm$ 0.01) eV. The values for the capture cross-section are the followings: (4.6 $\pm$ 1.2)·10^{-12}, (6.6 $\pm$ 1.7)·10^{-12} and (1.4 $\pm$ 0.4)·10^{-14} cm^2, for *only-QD*, *only-barr* and *QD-barr* respectively.

The *charge-selective* DLTS has been performed on both the *only-QDs* and the *QD-barr* samples to determine the *hole localization energy* E_{loc} for QDs with and without the AlP barrier. The voltage V_m= + 6 V is the highest value for which hole localization in QDs can be detected and therefore the energy value measured at this voltage represents the hole ground state in QDs, i.e. the E_{loc}. In fig. 4.8 the Arrhenius plot resulting from plotting $T^2\tau_{ref}\gamma_h$ of the DLTS spectra for every τ_{ref} vs. $1/T$ is displayed, referring to the sample *QD-barr*.

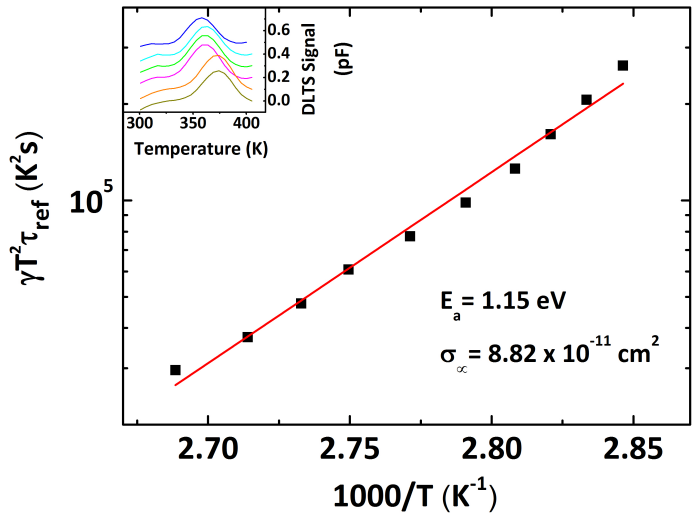

Figure 4.8: Arrhenius plot of the DLTS peak position for varying reference time constants τ_{ref} ranging between 0.5 and 5 s. In the inset, as an example, capacitance transients for τ_{ref} = 1.6 s are shown, which are taken for V_m between 1 and 6 V (V_p = V_m-1). *Courtesy of F. Arikan, TU Berlin.*

Via a linear fit, the activation energy and capture cross-section σ_∞ can be extracted, represented by the slope and by the value of the intercept with the y-axis, respectively. As an example, the capacitance transients for a τ_{ref} of 1.6

$Sample$	E_{loc} (eV)	σ_∞ (cm^2)	τ (s)
only-QD	0.370 ($\pm$ 0.008)	(2.1 $\pm$ 0.5)·10^{-12}	(7.7 $\pm$ 1.3)·10^{-9}
QD-barr	1.15 ($\pm$ 0.02)	(9 $\pm$ 5)·10^{-11}	3200 ($\pm$ 300)

Table 4.1: Localization energies and capture cross-sections obtained by charge-selective DLTS, together with the extrapolated storage times for the two QD-samples, alongside their errors.

s, taken between 1 and 6 V of the sample *QD-barr*, are depicted in the inset of fig. 4.8. For *only-QDs*, E_{loc} has been determined to be (0.370 $\pm$ 0.008) eV, while for *QD-barr* (**1.15 $\pm$ 0.02**) eV. The value of 1.15 eV localization energy represents here the combined effect of the QDs and the AlP barrier. The σ_∞ for *only-QDs* is (2.1 $\pm$ 0.5)·10^{-12}, while for *QD-barr* (9 $\pm$ 5)·10^{-11} cm^2.

In sec. 3.3 it has been shown that a contiguous GaAs interlayer beneath the QDs cannot be detected via TEM measurements. Assuming therefore that a given amount of GaAs from interlayer becomes incorporated into InGaSb QDs, a reduction in the actual Sb content of QDs is expected (an As/Sb intermixing is very likely to occur). This mechanism would also impact the real E_{loc} for InGaSb/GaP QDs, which is thus expected to lie in-between the VBO QDs/matrix of the two heterostructures $In_{0.5}Ga_{0.5}As$/GaP and $In_{0.5}Ga_{0.5}Sb$/GaP. The expected value can be calculated by using the *IFIGS-and-electronegativity* concept, which is to date considered a reliable method for providing the calculation of valence-band offsets of heterostructures[9]. This theory has recently found experimentally good agreement for the QD system GaSb/GaP, where the predicted VBO of 0.67 eV [138] agrees very well with the measured value of 0.65 eV between GaSb QDs and GaP matrix [81]. The calculation of the VBOs for the two QD-systems $In_{0.5}Ga_{0.5}As$/GaP and $In_{0.5}Ga_{0.5}Sb$/GaP yields $\sim$0.3 and $\sim$0.6 eV respectively [138]. Therefore, the measured value of $E_{loc} = (0.370 \pm 0.008)$ eV finds good agreement with the predictions. Finding a lower value for E_{loc} than the predicted $\sim$0.6 eV for $In_{0.5}Ga_{0.5}Sb$/GaP confirms the assumption of a significant As incorporation in QDs reducing the actual Sb content in the InGaSb QDs. The real VBO between such InGaSb QDs and GaP matrix becomes thus closer to that of $In_{0.5}Ga_{0.5}As$/GaP.

[9] The IFIGS-and-electronegativity theory provides a description of the electrostatic-dipole contribution to the semiconductor heterostructures VBOs by the electronegativity difference of the corresponding materials. A detailed discussion on this method can be found in [139] and [140].

Storage time After the determination of E_{loc} and σ_∞, the storage time τ for holes captured in QDs is extrapolated by using Eq. (4.1), which can be written as:

$$\tau = \frac{1}{\gamma T^2 \sigma_\infty} \exp\left(\frac{E_a}{k_B T}\right) \tag{4.7}$$

The parameter γ depends on the matrix material used, and for GaP amounts $\sim 2.6 \cdot 10^{25}$ [134]. Substituting the hole localization energy $E_{loc} = (1.15 \pm 0.02)$ eV and capture cross-section $\sigma_\infty = (9 \pm 5) \cdot 10^{-11}$ cm^2 found for the sample *QD-barr*, Eq. 4.7 yields a hole storage time τ at T = 300 K of (**3200** $\pm$ **300**) s (**$\sim$1 hr**). In table 4.1 the obtained values for the two QD-samples are listed alongside their errors. As expected from the previous observations, the highest τ is found for the structure with QDs and AlP barrier.

This result marks an improvement of one order of magnitude with respect to the former result of (230 $\pm$ 60) s for MOVPE-grown $In_{0.5}Ga_{0.5}As$/GaP QDs, where the hole localization energy E_{loc} for the system (QDs + AlP) was determined to be (1.14 $\pm$ 0.04) eV and the capture cross-section $\sigma_\infty \sim (8 \pm 5) \cdot 10^{-10}$ cm^2 [107]. Hence, the increase in the storage time τ has been obtained through a reduction of one order of magnitude of σ_∞, while the two measured E_{loc} for $In_{0.5}Ga_{0.5}As$/GaP and InGaSb/GaP appear comparable. This effect is ascribed to the use of Sb instead of As in QDs, which has apparently impacted the capture processes of holes in QDs. A deeper understanding of such processes requires further investigations, in particular as far as regards the chemical composition of QDs.

In conclusion, the material combination InGaSb/AlP/GaP proposed in this work represents a promising candidate for the use in the future QD-Flash, provided two important considerations:

1. the As incorporation into QDs should be reduced in order to obtain almost pure $In_{0.5}Ga_{0.5}Sb$ QDs. This would increase the Sb content in QDs and, according to the theoretical predictions, enhance the localization potential for holes of $\sim$0.3 eV, reaching $E_{loc} = 1.45$ eV and thus making the non-volatility feasible;

2. the measured $E_{loc} = 1.15$ eV would be already sufficient to reach the 10 years retention time, if the capture cross-section would be reduced to $\sigma_\infty = 10^{-14}$ cm^2.

The next step towards non-volatility is therefore the development of a systematic capture cross-section engineering, aiming to achieve a reliable method to control the capture cross-section of the QDs through their growth parameters. Furthermore, additional investigations on QD growth conditions are needed in order to have a better control on the QD composition.

Summary

- *p*-doping of GaP has been improved by using the carbon precursor CCl_3Br. Doping concentration between $3{\cdot}10^{16}$ and $8{\cdot}10^{17}$ cm^{-3} have been successfully reached. A mirror-like GaP surface has been obtained at low carrier concentrations (of $5{\cdot}10^{16}$ cm^{-3}), a value needed for the fabrication of the DLTS structure. The advantages of using C instead of the common Zn are the lower diffusivity and activation energy with respect to C and the absence of a *memory effect*. These properties allow for the fabrication of abrupt interfaces and ensure a greater availability of free holes at low temperatures with respect to Zn-doped epilayers.

- Electrical characterizations, by means of *conventional* and *charge-selective* DLTS, have been carried out on QD structures with and without an AlP barrier, to determine the hole localization energy and the capture cross-section. Charge-selective DLTS measurements on InGaSb/AlP/GaP QDs result in the highest localization energy of 1.15 eV for holes captured in QDs. The associated QD capture cross-section has increased by one order of magnitude with respect to the one of $In_{0.5}Ga_{0.5}As$/AlP/GaP QDs. This is ascribed to the use of Sb instead of As in QD growth and leads to a hole storage time of about 1 hour at room temperature, making InGaSb/GaP QDs promising candidates for QD-based nano-memories.

- The next step towards non-volatility is the development of a reliable method aiming to control still more systematically the capture cross-section by modifying the QD properties. Furthermore, a reduction of the As incorporation via As/Sb intermixing in QDs has to be taken into account to increase the hole localization.

Chapter 5

Optical properties and electronic structure

"If we knew what it was we were doing, it would not be called research, would it?"

A. Einstein

In this chapter optical properties of InGaSb/GaAs/GaP QDs are investigated via static photoluminescence (PL), cathodoluminescence (CL) and time-resolved PL (TRPL). The experimental results are discussed in order to derive a proposal for the electronic structure.

5.1 Sample structure for PL investigations

The usual sample structure containing QDs used for optical characterizations is shown in fig. 5.1. Here, the QDs are embedded in GaP matrix with a thin GaP cap layer (usually of few nm) grown at the same growth temperature T_g as for the QDs, which aims to stop the QD ripening. To complete the sample structure, an additional GaP layer of 50 nm is grown at $T_g = 620$ °C. This temperature has been chosen to minimize thermally activated In and/or Ga interdiffusion in the QD layer. In fact, for a temperature equal or greater than 650 °C, a blueshift of the QD emission has been frequently observed, in particular for InAs/GaAs QDs [141],[142]: In and/or Ga might migrate from the QDs across the QD/matrix interface, causing a modification of QD size and composition, which results in a blueshift in the QD emission.
As it can be seen in fig. 5.1, an additional $Al_{0.4}Ga_{0.6}P$ barrier is placed 150 nm beneath the QD layer, and used to provide a diffusion barrier for the photogenerated charge carriers. For every sample, the total thickness comprising the GaP

grown above and below the QDs and the barrier is kept fixed, in order to provide a constant crystal volume where the charge carriers are photogenerated. In this way, the luminescence intensity obtained for the various QD structures at the same external excitation can be compared.

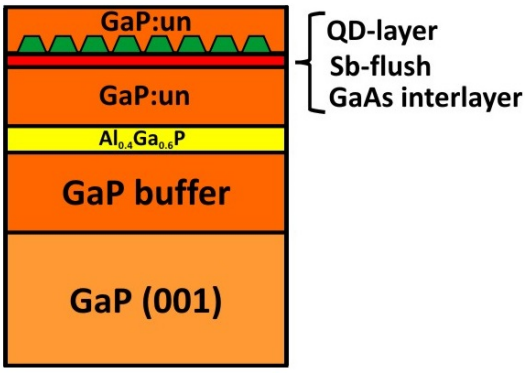

Figure 5.1: Schematic structure of a PL structure with embedded QDs.

For the optical characterizations, undoped GaP substrates[1] have always been used, to avoid spectrally overlapping emission from impurity centers in GaP.

5.2 Detection of QD luminescence via TEM-CL

In fig. 5.2 **(a)** a cross-sectional STEM image (high-angle-annular-darkfield contrast) of a PL sample containing QDs reveals the complete layer structure, referring to fig. 5.1. The QDs and the 20 nm $Al_{0.4}Ga_{0.6}P$ layers can be clearly revealed, in white and dark gray, respectively. Simultaneously, cathodoluminescence spectroscopy has been carried out in a scanning transmission electron microscope. A CL linescan was recorded at a temperature of 15 K, across the layer structure depicted in fig. 5.2 **(a)**. The color contrast shown in **(c)** represents the measured CL intensity as a function of the specimen position. The QD emission is detected between 1.74 and 1.88 eV, while the emission in the range of 2.2 - 2.3 eV close to the GaP energy gap can be attributed to neutral donor bound excitons (D^0,X) transition [143]. Fig. 5.2 **(c)** is a linescan from the surface towards the GaP substrate showing wavelength and intensity distributions at each position[2].

[1] Due to shortcoming supply, substrate batches were ordered by different companies. Therefore, slight variations in the emission wavelength and intensity within the different sample sets cannot be excluded, and they are due to the distinct wafer origin.

[2] Also in the submitted paper: E. M. Sala, F. Arikan, L. Bonato, F. Bertram, P. Veit, J. Christen, A. Strittmatter, and D. Bimberg, *MOVPE growth of (In,Ga)Sb/AlP/GaP(001) quantum dots for nanoscale memory applications*.

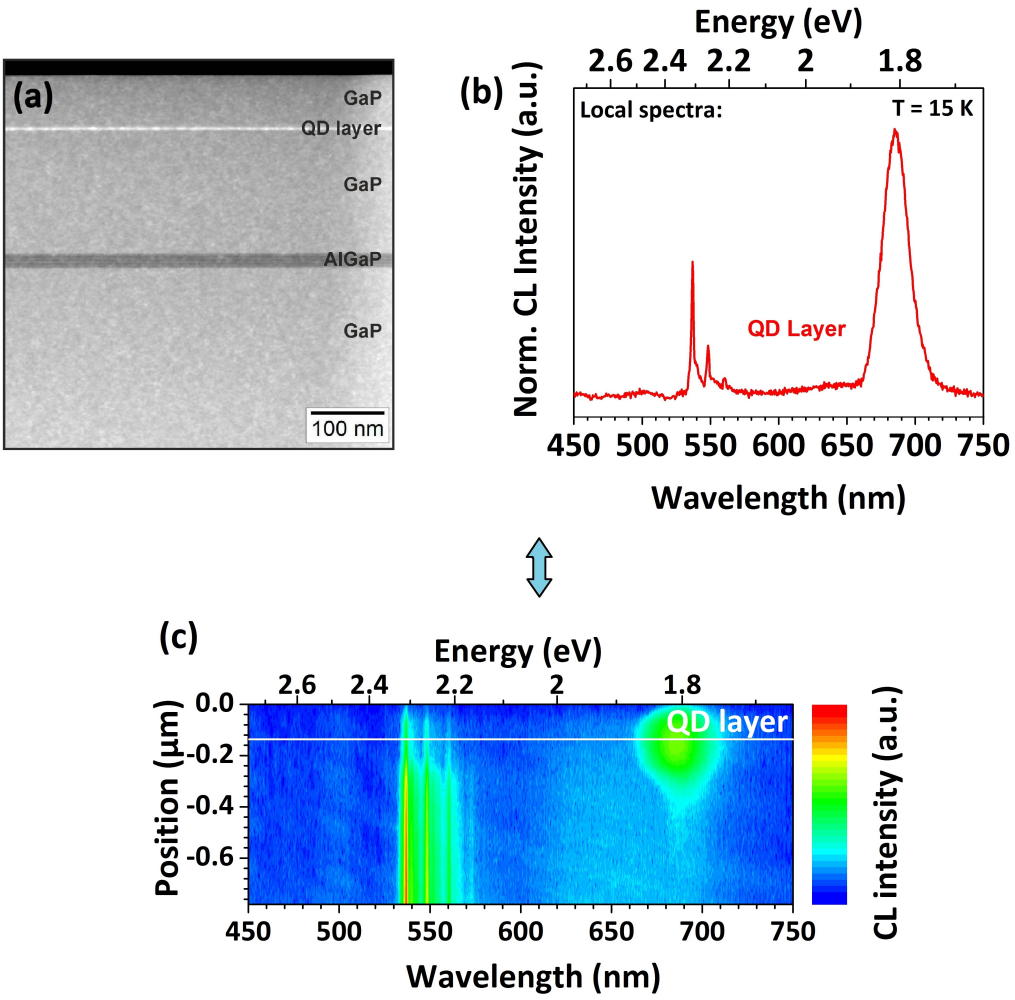

Figure 5.2: **(a)** Cross-section STEM view of a PL structure with embedded QDs (as depicted in fig. 5.1) in HAADF contrast. The QD layer can be detected as the horizontal white line, 50 nm below the top surface, while the dark gray broad line 20 nm thick represents the $Al_{0.4}Ga_{0.6}P$ layer. **(b)** Corresponding CL linescan at 15 K and **(c)** CL linescan showing wavelength and intensity distributions of various distances from the surface. The emission detected at ∼1.82 eV originates from the InGaSb/GaAs/GaP QD region, while the one at ∼2.2 - 2.3 eV belongs to GaP (including 4 phonon replica).

5.3 Development of QD luminescence

In fig. 5.3, three PL spectra taken at T = 10 K of different PL samples are presented, containing respectively: only 5 ML GaAs interlayer, 5 ML GaAs interlayer + 0.21 ML InGaSb, or 5 ML GaAs interlayer + 0.51 ML InGaSb. All spectra show two main emissions, one between 1.7 and 2 eV and a broader one in the range 1.3 - 1.5 eV. The latter is found in every PL spectra investigated in this work (both in samples with and without QDs, independently of the InGaSb coverage) and is ascribed to the near infrared emission of donor-acceptor (D,A) pairs (DAP) in GaP, which arises at low temperature. This pair recombination process was extensively studied by Dean *et al.* in [144] where such (D,A) pairs were found to be formed by carbon, cadmium, or zinc bound to a deep trap center as oxygen, which is usually present inadvertently in GaP grown crystals. By comparing the present results with the GaP luminescence spectra of [144], the emission observed here can be attributed to a carbon acceptor bound to an oxygen trap. At low temperatures, this emission represents an efficient radiative recombination channel, competing thus with the QDs (or GaAs QW) in trapping the charge carriers. From here on, this long-wavelength emission will be referred to as *competing DAP channel*. As it will be seen later, this luminescence is almost totally suppressed at room temperature. Most likely, the shallow acceptor-bound electron thermally escapes at higher temperatures.

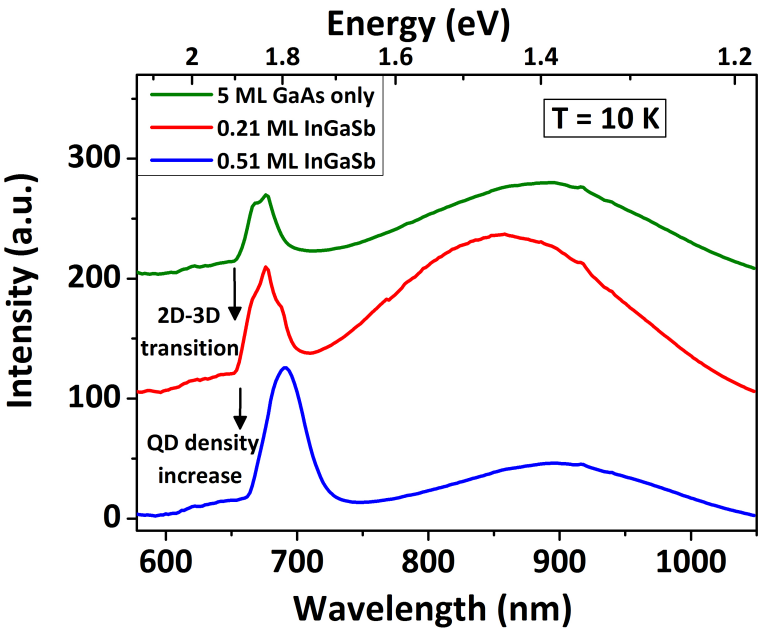

Figure 5.3: PL spectra recorded at T = 10 K of GaAs/GaP and InGaSb/GaAs/GaP QDs, with 2s Sb-flush and 1s GRI, showing the transition from GaAs QW to QDs. The spectra are vertically shifted for better visualization. Excitation density: 1000 $W{\cdot}cm^{-2}$.

The green line of fig. 5.3 corresponds to the emission of the GaAs interlayer and it is splitted into two peaks, having energies of 1.83 and 1.85 eV. These can be ascribed to the emission caused by island formation occurring at the interface of the thin GaAs QW, also known as *monolayer-fluctuations* [145]. Since this GaAs interlayer is not an homogeneously closed layer, as already pointed out in chapter 3, fluctuations of the layer thickness are very likely to occur. These observations find good agreement with the study of Prieto *et al.* in [146], who report on optical and theoretical studies of GaAs QWs grown on GaP. The authors investigate the optical emission of GaAs QWs with thicknesses between 1 and 6 ML, and compare the experimental results to the theoretical calculations.

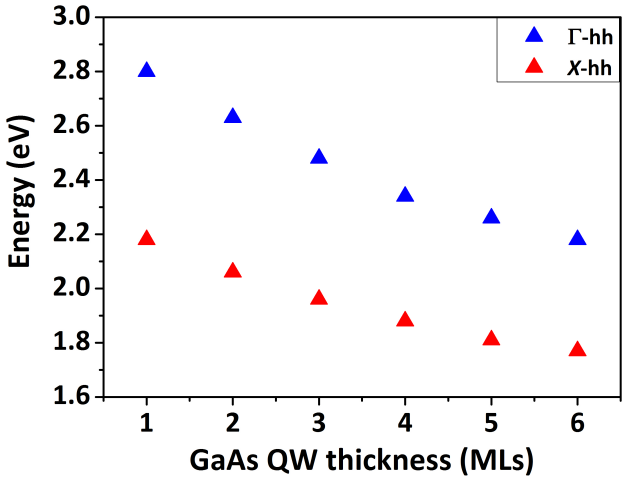

Figure 5.4: Calculated transition energies between electrons residing in X and Γ states and heavy holes (hh) in a GaAs QW strained on GaP. After [146].

Such splitting in the optical spectra is observed also there and reflects the ML-fluctuations at atomic scale of the GaAs QW. More precisely, these two peaks correspond to the emissions of a 4 and 5 ML-thick GaAs layer (1.88 and 1.81 eV respectively), as indicated in fig. 5.4. The slight discrepancy between the predicted values and the experimental results found here can be ascribed to intermixing at the GaP/GaAs interface. The observed transitions correspond to the recombinations between electrons in the X minimum and heavy holes (hh) of GaAs, and labeled as X-hh. The transition Γ-hh indicated in blue in fig. 5.4 refers to the transition between electrons in the Γ conduction band of GaAs and heavy holes. It is worth noticing that the additional emission detected between 600 and 650 nm (i.e. between 1.9 and 2.1 eV) in the three spectra of fig. 5.3 is again due to ML-fluctuations, corresponding in this case to 2 - 3 MLs, as suggested in fig. 5.4.

The red line of fig. 5.3 refers to spectrum when the 2D-3D transition for QD formation starts, which occurs for 0.21 ML InGaSb, as revealed by the AFM investigations of sec. 3.2.3. Fig. 5.5 **(a)** shows such spectrum, with Gaussian line-shape fits: a peak arises at the low energy side of the emission (1.82 eV, drawn in green), showing the first contribution of QDs to the PL emission, while the double contributions of the GaAs interlayer are still partially present (1.83 and 1.85 eV, drawn in blue). With increasing InGaSb coverage (0.51 ML), the low energy contribution redshifts from 1.82 eV to 1.79 eV, and the total intensity is increased almost 3-times, in agreement with increasing QD density (see green fit of fig. 5.5 **(b)**). A strong reduction (ca. 6-times) of the *competing DAP channel* emission can be also associated with the QD density increase. In fact, the QDs provide more efficient recombination channels than the *DAP*.

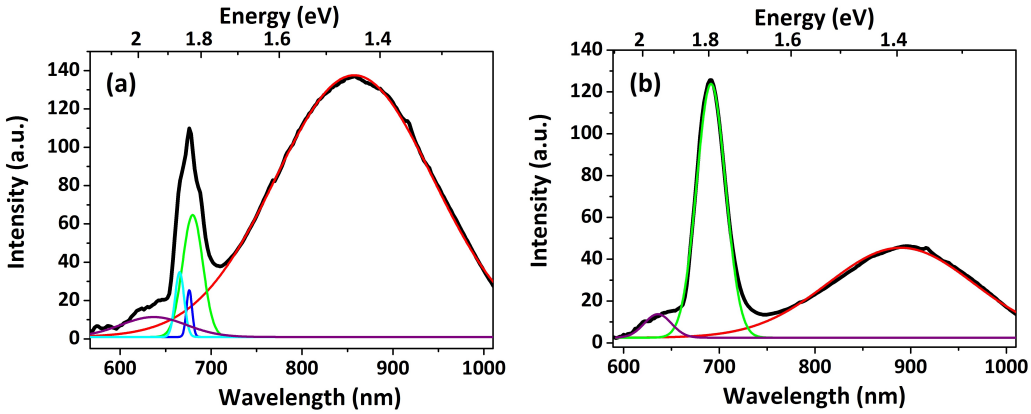

Figure 5.5: Examples of line-shape fits using Gaussian functions on **(a)** sample showing 2D-3D transition (0.21 ML InGaSb) and **(b)** sample with 0.51 ML InGaSb QDs, 2s Sb-flush and 1s GRI. Both referring to the plots of fig. 5.3. Excitation density: 1000 W·cm^{-2}, T = 10 K.

5.4 Influence of increasing InGaSb coverage

In fig. 5.6 the PL spectra recorded at room temperature of samples with buried QDs on 5 ML GaAs are shown, where the InGaSb coverage was varied from 0 (corresponding to only GaAs interlayer) to 1 ML. The emission energy of the sample containing only the GaAs interlayer is detected at $\sim$ 1.82 eV (here, the splitting previously observed at T = 10 K is disappeared due to the broadening at room temperature).

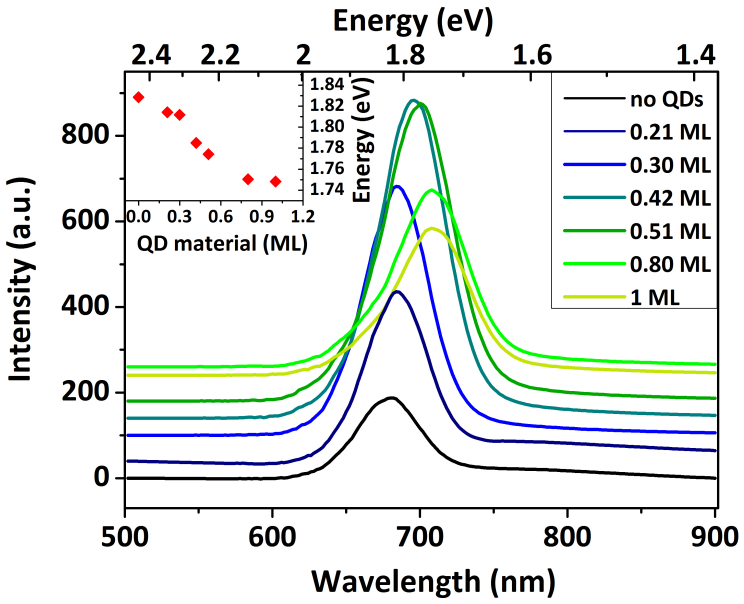

Figure 5.6: PL measurements at T = 300 K of QD samples with varying InGaSb supply, from 0 to 1 ML, with 2s Sb-flush and 1s GRI. Excitation density: 1000 W·cm^{-2}. The spectra are vertically shifted for better visualization. In the inset, the spectral position of the emission energy vs. the QD material is displayed.

By increasing the InGaSb coverage, the emission intensity increases, as also displayed in plot of fig. 5.7. For 0.21 ML, the emission energy shifts towards lower energies (of $\sim$ 10 meV), and the intensity is doubled: this behavior is ascribed to the 2D-3D transition, where the first QDs are formed, as also confirmed by the AFM investigations of sec. 3.2.3. Further InGaSb supply (0.42 ML) leads to an additional redshift of $\sim$ 30 meV and the total emission intensity becomes 4-times greater as the emission from the *only GaAs interlayer*. Here, more QDs are formed and contribute to the total emission. Moreover, the QDs grow bigger in size and the QD levels lie deeper in the gap [23], resulting in a redshift of the transition energy. If the coverage is further increased, from $\sim$ 0.8 ML onwards the intensity drops and only small redshift of the emission occurs: the increase of the QD dimensions is accompanied by the formation of defects which reduces

the total QD emission due to non-radiative recombination.

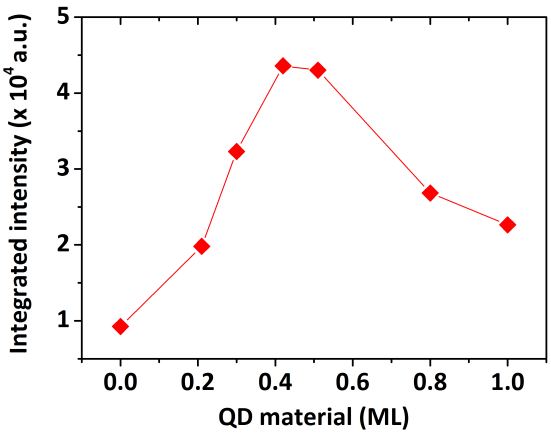

Figure 5.7: Integrated emission intensity of QDs with varying InGaSb supply.

5.5 Modification of the V/III ratio during QD growth

The V/III ratio used during QD growth has been adjusted to optimize the QD emission intensity. Its influence on the luminescence has been studied by modifying the Sb supply, while keeping the Ga flux constant. The TESb molar flux has been varied between 1.3 and 10 μmol/min, resulting in a V/III ratio of $\sim$ 0.15 - 1.2. Fig. 5.8 **(a)** displays the PL spectra of QDs grown with different V/III ratios.

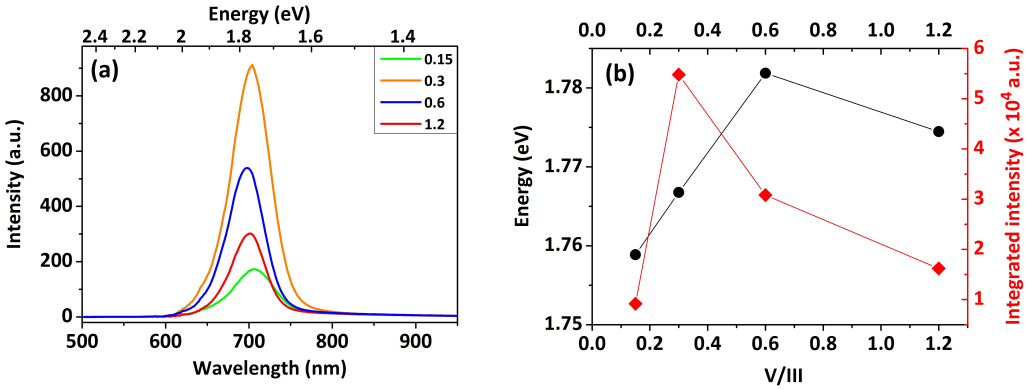

Figure 5.8: **(a)** PL spectra of QDs (InGaSb coverage of 0.51 ML, 2s Sb-flush, and 1s GRI for all samples). **(b)** Trend of the QD emission energy together with the total integrated intensity vs. the V/III ratio. Excitation density: 1000 W·cm^{-2}.

The spectral position varies slightly with the V/III ratio ($\sim$ 20 meV), whereas

the emission intensity increases by 6-times over the entire range, as also shown in fig. 5.8 **(b)**. The limited variation of the emission energy suggests that the QD dimensions and composition remain rather stable, although the V/III ratio varies by one order of magnitude. This is again ascribed to the surfactant effect of antimony which reduces the adatom surface diffusion, partly suppressing the material transfer between the QDs. The increase in the QD luminescence intensity is attributed instead to the reduction of defects with increasing Sb supply, as also previously seen (sec. 3.2.5). The optimum is found for a V/III ratio of ~ 0.3 and this value is used for all the PL structures investigated in this work.

5.6 QD ripening during growth interruption

The impact of the growth interruption (GRI) on the QD morphology studied in sec. 3.2.4 can be better understood with the addition of PL investigations. In fig. 5.9 PL spectra at room temperature of QDs grown with different GRI times are displayed. The QD emission is detected between 1.77 and 1.74 eV, for 1 and 800 s GRI, respectively.

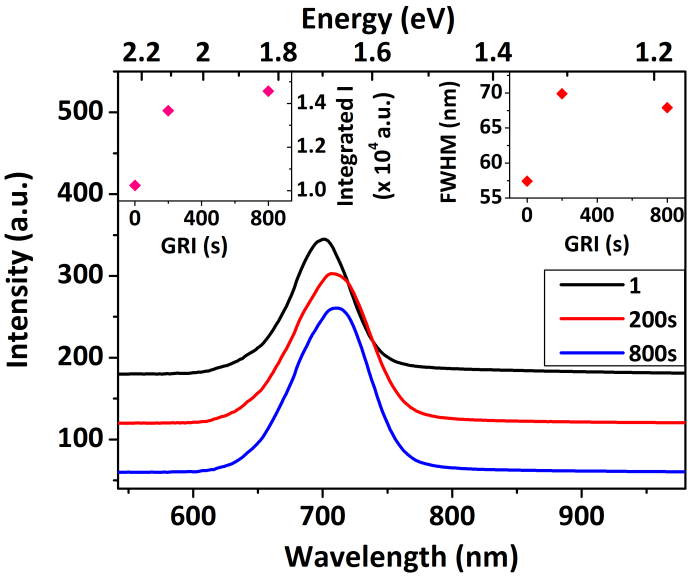

Figure 5.9: PL spectra of buried 0.51 ML InGaSb QDs, 1s Sb-flush, recorded at 300 K, grown with different GRIs. In the inset on the right the FWMH vs. GRI time is plotted, while on the left the total integrated intensity vs. GRI is shown. The spectra are vertically shifted for better visualization. Excitation density: 1000 W·cm^{-2}.

The QD luminescence redshifts by $\sim$30 meV proportional to GRI time, revealing an increase of the average QD volume, as also supported by the AFM investigations. The associated FWHM is displayed in the right inset of fig. 5.9:

the QD emission for 1s GRI exhibits a FWHM of ∼57 nm, which increases by ∼ 20 % for 200 s and then remains almost stable up to 800 s. The trend of the FWHM confirms the broadening of the QD size distribution with increased GRI. In the left inset, the total integrated intensity is displayed versus GRI time: an extended GRI of 800 s leads to an increase of 45% in the PL emission, as compared to 1 s. Interestingly, the emission intensity and energy remain quite stable with a prolonged GRI, in contrast to what is found for InGaAs/GaP QDs studied by Stracke *et al.* [40]. There, GRIs greater than 150/200 s led to a remarkable decrease in the QD emission. A similar behavior has been observed also for InAs/GaAs QDs [86]. In both cases, the luminescence drop is due to the formation of defects (as plastically relaxed islands). In the present study, instead, with the extended GRI, no clusters are formed even for 800 s, as also confirmed by the previous AFM investigations of sec. 3.2.4. As discussed there, both the quite low V/III ratio (∼ 0.3) and the Sb supply during QD growth help to reduce the adatom diffusion length and material transfer between the 3D islands. On the other hand, the reduced redshift of the QD spectral position reflects the indirect nature of the considered energetic transition: for type-II QD heterostructures, the variations of QD size has a limited influence on the optical transition, compared to type-I structures [86], due to the spatial separation of the charge carriers (here: electrons in the X-valley of GaP at the QD interface and holes in the QD). A reduced impact of the GRI on the QD spectral position has been also reported for InGaAs/GaP QDs (grown without strain-reducing layer) in [40].

In fig. 5.10, PL spectra of the same QDs taken at low temperature (T = 40 K) are shown.

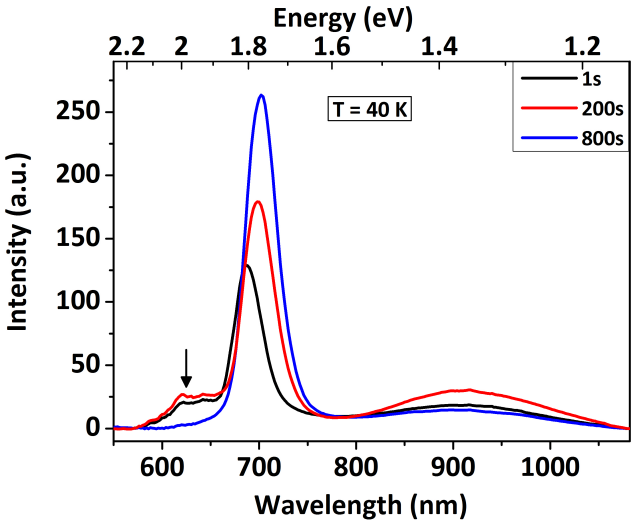

Figure 5.10: PL spectra of buried 0.51 ML InGaSb QDs, 1s Sb-flush, recorded at 40 K, grown with different GRI durations. Excitation density: 1000 W·cm^{-2}.

The spectral trends are similar as for room temperature measurements, i.e.

a slight redshift with increasing GRI is accompanied by an increase in the QD emission intensity. Additionally, only for shorter GRIs, a luminescence around 1.9 - 2 eV is detected and indicated with an arrow in fig. 5.10. This feature has been already observed and discussed previously (sec. 5.3) and attributed to ML-fluctuations at the thin GaAs QW interface [145],[146]. As the QDs grow larger (800 s GRI), this luminescence quenches, while the one of QDs increases. As in the case of InGaAs/GaP QDs [40],[147], strain induced electron states around the QD region (X-valley) may evolve at lower energies than the GaAs QW states with increasing QD size.

5.7 Influence of antimony-flush on QD luminescence

As previously seen in sec. 3.2.5, the use of an Sb-flush in QD growth has been found to be essential in controlling the structural properties of QDs. To evaluate the impact of such Sb-flush on the QD optical properties, PL structures containing QDs grown with increasing t_{Sb} have been fabricated. t_{Sb} has been varied between 0, 2 and 4 seconds, as for the AFM set of sec. 3.2.5. In fig. 5.11 their PL spectra recorded at room temperature are presented.

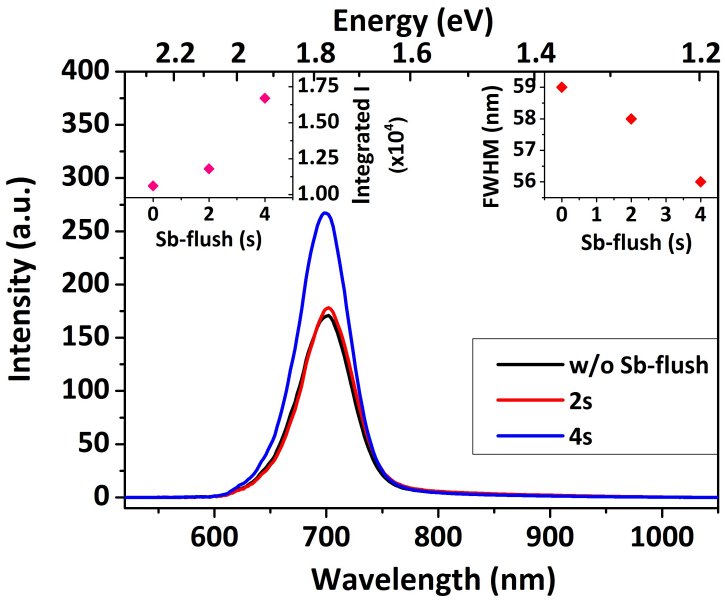

Figure 5.11: PL spectra at room temperature of buried 0.51 ML InGaSb QDs, grown with different t_{Sb}, 1s GRI. In the inset on the right the FWHM of the QD emission is plotted vs t_{Sb}. In the inset on the left the total integrated PL intensity vs. t_{Sb} is displayed. Excitation density: 1000 W·cm^{-2}.

A larger integrated intensity can be found for $t_{Sb} = 4$ s, which shows an improvement of ∼45% compared to QDs grown without Sb-flush. Simultaneously, the FWHM of the QD emission is slightly reduced (of $\sim 5\%$), as also displayed in the right inset of fig. 5.11. A blueshift of the QD spectral position can be also detected, amounting to $\sim$ 5 meV. These observations are consistent with the previous AFM investigations, where the QDs become slightly smaller and more homogeneous with a prolonged t_{Sb}, which plays also an important role in suppressing the non-radiative recombination (reduction of cluster formation).

5.8 Optimization of QD cap layer thickness

To optimize the thickness of the QD GaP capping, a sample set with different capping layers has been fabricated, i.e. from 1 to 10 nm, and grown at the same substrate temperature of QDs ($T_g = 500$ °C). Fig. 5.12 displays the PL spectra of QD structures with different capping thicknesses.

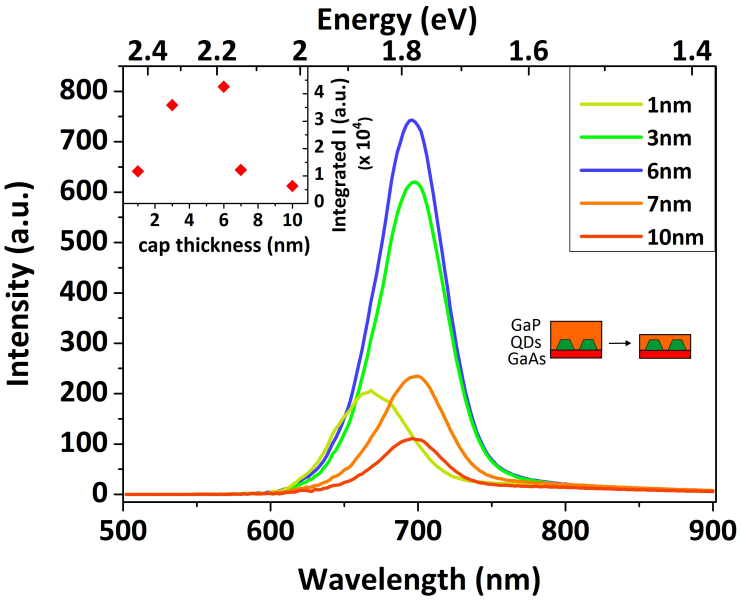

Figure 5.12: PL spectra at T = 300 K of samples with capping layers between 1 and 10 nm. Excitation density: 1000 W·cm^{-2}. The QDs are grown with ∼0.41 ML InGaSb, 2s Sb-flush, 1s GRI. In the inset the trend of total integrated intensity towards the cap thickness is displayed. On the right a sketch schematically depicts the reduction of the GaP cap above the QDs.

For a GaP coverage of 1 nm, the QD emission energy lies at 1.86 eV, while from 3 nm onwards it remains around 1.78 eV, without further noticeable vari-

ations. On the other hand, the emission intensity increases by 3-times from 1 to 3 nm, reaching the maximum for 6 nm cap thickness, while from 7 nm on, it drops abruptly. At 1 nm, the rather low emission intensity, together with the spectral position of 1.86 eV, suggests that only few smallest 3D islands are covered by the thin GaP cap. In fact, the QD luminescence is even blueshifted with respect to that of the 5 ML GaAs only (lying at $\sim$ 1.82 eV, see fig. 5.6). Here, the QDs that remain uncapped after the cap growth are apparently dissolved during the following ramping up of temperature (T_g = 620 °C), which is needed for the growth of the last 50 nm GaP layer. The trend observed from 7 nm onwards is ascribed to defect formation reducing the QD emission intensity, due to non-radiative recombination. Indeed, since the T_g = 500 °C used for the cap does not ensure a defect-free step-flow GaP growth (GaP grows rather by 2D islands), the formation of point defects for thicker cappings is very likely.

5.9 Temperature dependent investigations

Fig. 5.13 shows the temperature-dependent PL spectra of QDs over the range 10 - 300 K. For temperatures < 40 K many sharp maxima between 2.1 and 2.3 eV close to the GaP bandgap are visible, corresponding to the neutral donor bound excitons (D^0,X) transition, which finds agreement with the CL observations presented in fig. 5.2.

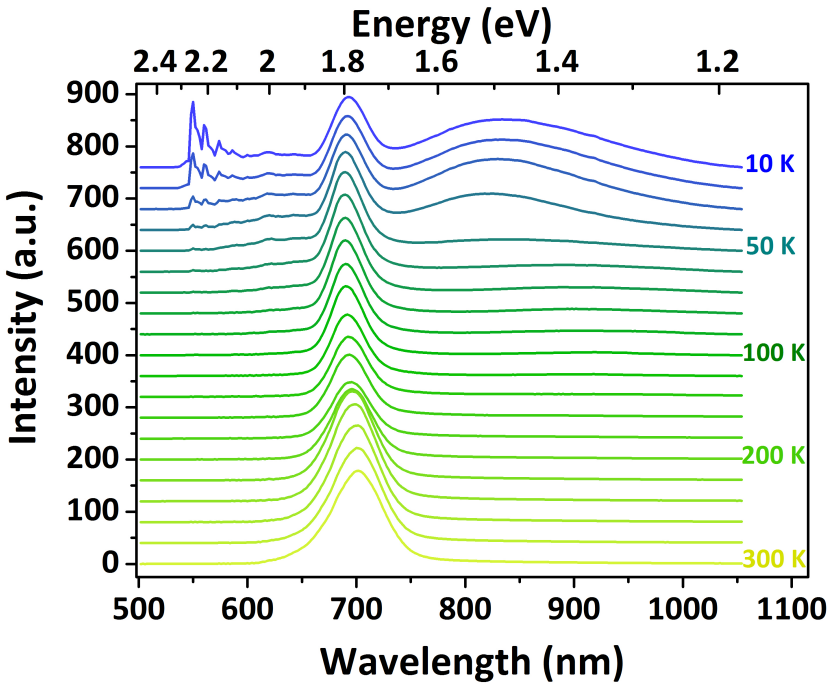

Figure 5.13: Temperature dependent PL spectra of buried 0.51 ML InGaSb QDs, 2s Sb-flush, 1s GRI. The corresponding temperatures are shown on the right. The spectra are vertically shifted for better visualization. Excitation density: 1000 W·cm^{-2}.

Additionally, for T $\leq$ 70 K, local maxima between 1.9 and 2 eV belong to ML-fluctuations at the GaAs/GaP interface, while the QD emission detected at T = 10 K lies at $\sim$1.79 eV. The emission of the *competing DAP channel* is also easily recognizable for T $\leq$ 50 K. In this temperature range such luminescence quenches very fast, as also shown by the red curve of fig. 5.14, displaying the trend of the integrated intensities for 10 $\leq$ T $\leq$ 300 K. For T $>$ 50 K, this quenching proceeds more slowly towards 300 K. The QD emission intensity, instead, stays almost stable until about 180 K and from 200 K on starts increasing (see black curve). At T = 300 K it is doubled compared to the initial value. Such behavior is in contrast to what is usually observed in temperature-dependent investigations of

QDs, where the carrier capture by QDs decreases with temperature [148],[149], [150]. Here, with increasing temperature, the electrons bound to the shallow acceptors are likely to thermally escape, so that more carriers may contribute to recombination in the QDs.

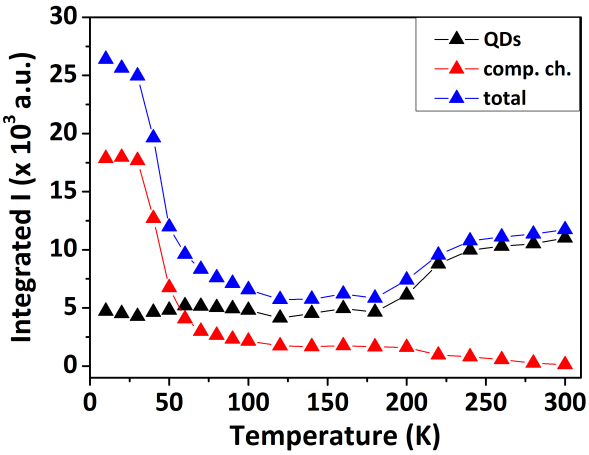

Figure 5.14: Trend of the total integrated emission intensity, with indication of the different contributions (QDs, *competing DAP channel*) vs. temperature (10 - 300 K).

Fig. 5.15 displays the trend of the QD emission energy over the whole temperature range, where two important characteristics can be distinguished:

1. a moderate blueshift of about 10 meV at low temperatures (10 - 60 K), in contrast to the S-shape feature usually observed in temperature-dependent investigations of type-I QDs, and

2. a weaker temperature dependence compared to the well-known Varshni trend [151], in the range of 70 - 300 K.

The conventional S-shape of the QD spectral position (meaning an initial red-shift followed by a blueshift) found in the temperature-dependent investigations of type-I QDs, as for InAs/GaAs [148],[149],[152] is not revealed here. Such phenomenon is commonly attributed to carrier delocalization from strongly to weakly localized states, in particular due to potential flutuactions given by interface disorders and/or composition inhomogeneities [153]. In the investigations carried out in this work, instead, a moderate blueshift for $10 \leq T \leq 60$ K is observed. It amounts to $\sim$10 meV, as indicated by the blue arrow in fig. 5.15, and represents a clear sign of carrier delocalization. A comparable evolution of the QD spectral position has been found in other Sb-based type-II QD heterostructures, as for GaSb/GaAs QDs investigated by Müller-Kirsch in [154] and InSb/InAs QDs studied by Lyublinskaya *et al.* in [155]. Due to the high QD

density ($\sim 10^{11}$ cm^{-2}), a carrier redistribution between the QDs due to tunneling is possible, so that they can migrate from dot to dot. If additionally QDs have a rather homogeneous size distribution as here, such relocalization is most likely to occur.

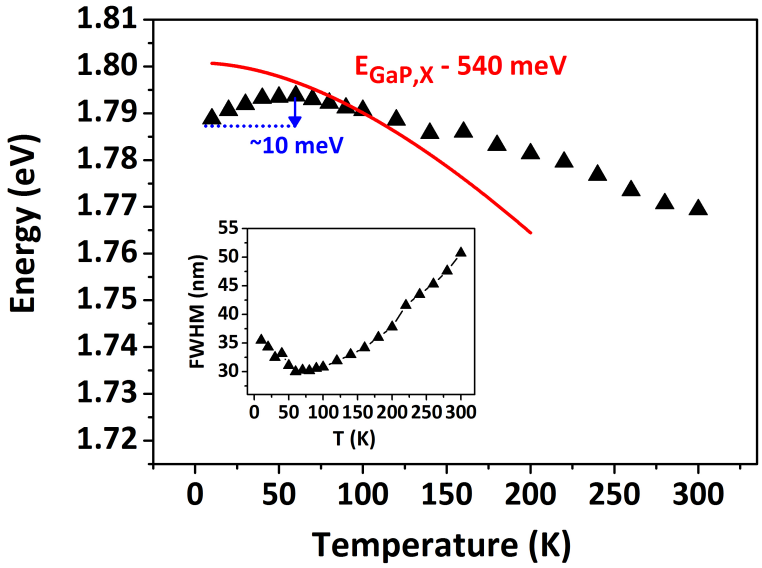

Figure 5.15: Trend of the QD emission energy vs. temperature (10 - 300 K). A Varshni fit is also displayed, referring to the GaP indirect energy gap at the X point. The inset shows the trend of the QD FWHM with temperature.

In particular, the trend of the FWHM of QD emission displayed in the inset of fig. 5.15 reveals a carrier delocalization into smaller QDs: starting from 10 K, it decreases until it reaches its minimum at exactly 60 K, when the blueshift ends. Thereafter, for $T >$ 60 K the FWHM broadens monotonically up to $T =$ 300 K. In the temperature range 70 $\leq T \leq$ 120 K, the QD emission energy follows the Varshni trend for the indirect bandgap of GaP in X ($E_{GaP,X}$), as displayed by the red curve in fig. 5.15, where 540 meV have been subtracted to provide a fit to the experimental data points. For greater temperatures, instead, a deviation from such redshift is observed. Simultaneously, the integrated intensity of the QD emission gradually starts to increase (see fig. 5.14), revealing an additional contribution of thermally activated radiative recombinations. With increasing temperature, the phonon population in the system is enhanced, so that the contribution of phonon-assisted transitions due to phonon-scattering becomes relevant. Most likely, electrons are scattered from the X point to higher energy levels with better WF overlap with the holes in the QDs, as for GaAs or Γ states[3] and recombine there. Such carrier delocalization leads to a partial compensation of the Varshni redshift, resulting in a weaker temperature dependence.

[3] As reference see also the proposal of band edge configuration of InGaSb/GaAs/GaP QDs, sec. 5.13.

5.10 Expectations for a type-II band alignment

As introduced in chapter 1, QDs showing a type-II band alignment possess particular properties, because of the charge carrier spatial separation. Here, the consequences of such kind of band alignment will be discussed. The separation of charge carriers, i.e. the holes localized in the QD body and electrons in the surroundings, causes a diminished electron-hole wavefunction (WF) overlap and consequently a reduction of the transition rate (i.e. recombination probability), generally resulting in long radiative decay times (see also sec. 5.12). Instead, in a type-I QD heterostructure, both charge carriers are localized in the QD body, which leads ideally to an e-h overlap of 100% [156].

The effects taking place in a type-II QD system are actually complex, but can be summarized as follows:

- *Coulomb interaction* between electrons residing in the QD surroundings and holes in the QD. The electric field generated by the two charge carrier types modifies the confinement potential and generates a triangular potential well for non-equilibrium electrons at the QD/matrix interface [157]. With increasing excitation density, this quantum well becomes deeper and the electron confining potential becomes deeper as well [158]-[160] (approximation of infinite triangular QW). As a consequence, a band bending of the band structure is formed (see fig. 5.16) which pushes electrons closer to the holes confined in the QD. By applying an increasing external pumping, the optical transition energy increases proportionally and a blueshift is observed in the PL spectra.

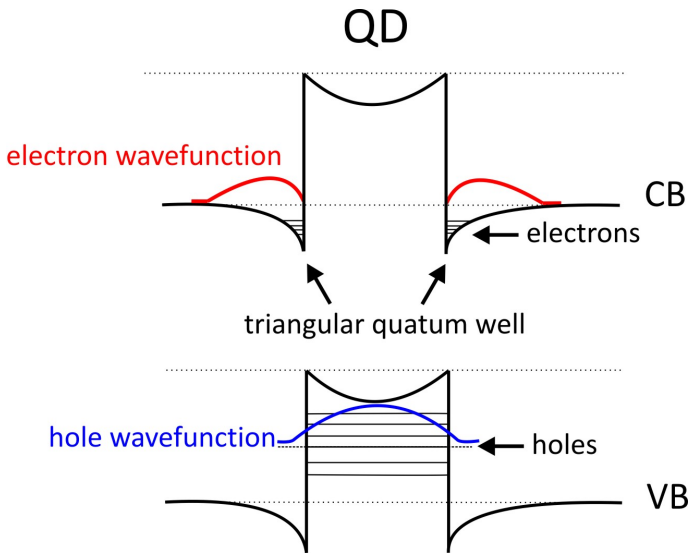

Figure 5.16: Schematic drawing of a type-II QD with indication of electron and hole wavefunctions and quantized states.

More precisely, the variation of the electron quantization energy in the triangular well with increasing carrier injection can be written as [158], [161]

$$\partial E_C = \left(\frac{\hbar^2}{2m^*}\right)^{\frac{1}{3}} \left(\frac{9}{8}\pi\right)^{\frac{2}{3}} \left(\frac{2\pi e^2}{\varepsilon_0 \varepsilon_r}\right)^{\frac{2}{3}} n^{\frac{2}{3}} \tag{5.1}$$

where n is the generated carrier density, m^* the electron effective mass, $\hbar$ the reduced Planck constant, and ε_0, ε_r the vacuum and the relative permittivity, respectively.
This modeling was initially developed for type-II QWs [158] but has found good agreement with various type-II QD system [25],[79],[99],[162].
To connect the excitation density (photon flux) with the generated carrier density in the material, one should consider the bimolecular rate equation [163]:

$$\frac{\partial n_e}{\partial t} = \frac{\partial n_h}{\partial t} = B n_e n_h \tag{5.2}$$

where n_e n_h are the electron and hole densities, respectively, and B the recombination constant. With the charge neutrality condition

$$n_e = n_h \tag{5.3}$$

So that the excitation density P generating a given concentration of electrons and holes can be written as:

$$P = B n^2 \tag{5.4}$$

Hence, by substituting (5.4) in (5.1):

$$\partial E_C \propto P^{\frac{1}{3}} \tag{5.5}$$

That is, the variation of the electron quantization energy in the triangular well is proportional to the third root of the applied excitation density. This description should be considered as a guide for the understanding of the impact of the Coulomb interaction between the separated charge carriers on the electron confinement. However, for a precise modeling, one has to take into account the actual QD physical properties and the influence of the applied excitation density. For instance, Gradkowski *et al.* in [164] have recently studied the variation of the electron and hole WF properties at high excitation densities for various type-II QD heterostructures, combining

theoretical and experimental investigations. Without, or at low external excitation, the electron WFs lie in the well between the QDs, whereas at higher carrier injection, the WFs undergo profound modifications, as for the formation of an electron WF tight ring around the QD body. As a consequence, the hole WF inside the QD is pushed towards the wider QD basis. This phenomenon apparently affects the transition probability (given by the overlap of the e-h WFs) and might lead to deviations from the above discussed relation $\partial E \propto P^{\frac{1}{3}}$. Similarly, Klenovský *et al.* in [165] report on the modeling of InAs QDs with GaAsSb capping layers having different thicknesses, and observe that the dependence of the emission intensity from the excitation power depends on the GaAsSb layer thickness employed. It deviates from the typical $P^{\frac{1}{3}}$ if a thick ($\sim$ 8 nm) GaAsSb layers is used, while for thinner ones ($\sim$ 3 nm) it follows the usual trend. To summarize, deviations from the predicted $P^{\frac{1}{3}}$ have to be considered, and might depend on the excitation power and/or on the specific QD system geometry and material combinations.

- *Many-particle effects*, i.e. interactions between the charge carriers: for 0D systems as QDs, the h-h interaction has to be taken into account: in fact, the h-h interaction dominates over e-e and e-h, resulting in a *capacitive charging* of the QDs [25],[166],[167]. The QDs can be thus considered as nano-capacitors holding a charging energy of

$$\partial E_C = \frac{e^2 d}{4\varepsilon_r \varepsilon_0} \tag{5.6}$$

  where e is the electron charge, d the QD diameter, and ε_0, ε_r the vacuum and the relative permittivity, respectively. In type-II QDs, the h-h interaction is much stronger than in usual type-I QDs and dominates over the other two types of interactions (e-h and e-e), thus contributing to the blueshift of the QD emission energy under increasing pumping.

- *State-filling*: the hole states in a QD are quantized and, by applying an increasing excitation power, the excited hole states can be gradually populated. This should result in the formation of "shoulders" in the PL spectra, which correspond to optical transitions at higher energies. This effect is usually observed in type-I QDs [168], where the arising excited state peaks are due to occupation of excited electron states and can be clearly distinguished. Instead, since for type-II QDs there are no electron states in the QD, the higher energy transitions cannot be clearly resolved and often result in a considerable broadening of the PL emission, as observed by Müller-Kirsch *et al.* in [169].

Excitation density dependent investigations on InGaSb/GaP QDs have therefore been carried out.

5.11 Excitation power dependent investigations

In this section, the QD emission with varying excitation power density P will be analyzed for QDs grown with different Sb-flush durations t_{Sb}, since the Sb-flush has been shown to remarkably affect the QD structural and optical properties. All investigations have been carried out at T = 10 K, with $2 < P < 1000$ W·cm^{-2}. For all spectra, a line-shape analysis with Gaussian curves has been performed to distinguish the different contributions of the PL emission. The resolved emissions are always denoted with "*peak 1, 2, 3* ", corresponding to the lowest, middle and highest emission energy of the QD ensemble, respectively, and displayed with the same colors on the graphs. Moreover, the line-shape fit of the *competing DAP channel* emission is always indicated in red.

Fig. 5.17 **(a)** shows the PL spectra for QDs without Sb-flush, and figs. 5.17 **(b)**-**(c)**, two examples of the corresponding line-shape fits for $P = 40$ and 140 W·cm^{-2}, respectively. By analyzing the spectra at such low excitation densities, it can be seen that *two* peaks can be fitted to the QD emission. By carrying out a similar analysis to the spectra corresponding to QDs with $t_{Sb} = 2$ s and 4 s, *three* contributions are distinguished (examples of these fits are given in figs. 5.19 and 5.21 **(b)**-**(c)**). Table 5.1 summarizes the values of the QD spectral positions for the different t_{Sb}, at the lowest excitation power $P = 2$ W·cm^{-2}. The observed emission energies are consistent with the previous AFM investigations showing size reduction and improved homogeneity of QDs grown with Sb-flush. Here, the contributions of the different QD size populations are detectable, which undergo a blueshift with increasing t_{Sb}, consistently with lower energy transitions due to decrease in QD size [23]. In particular, for t_{Sb}=2 s and 4 s, a third peak at higher energies 1.79 eV arises, ascribed to the smaller QD size population.
With increasing excitation density P, the general trend of the QD emission energies of all contributions is a blueshift, whose magnitude deviates from the theoretical $P^{\frac{1}{3}}$ discussed in the previous section. In table 5.2, for each QD emission (*peak*) the corresponding blueshift over the whole P range are given as "ΔE ". Moreover, the trend of the emission energies vs. P with varying t_{Sb} are displayed in figs. 5.18, 5.20 and 5.22 **(a)**. The curves can be fitted with power-law functions, showing that $\Delta E \propto P^b$ with $b \ll \frac{1}{3}$. The fitted values of the exponents can be found in table 5.3. The deviation of the emission energy from the third root of the pumping is qualitatively understood if a modified configuration of electron states is considered, compared to the sole bend bending of type-II QDs, which presupposes an approximation of infinite potential well confining electrons at the QD vicinity.

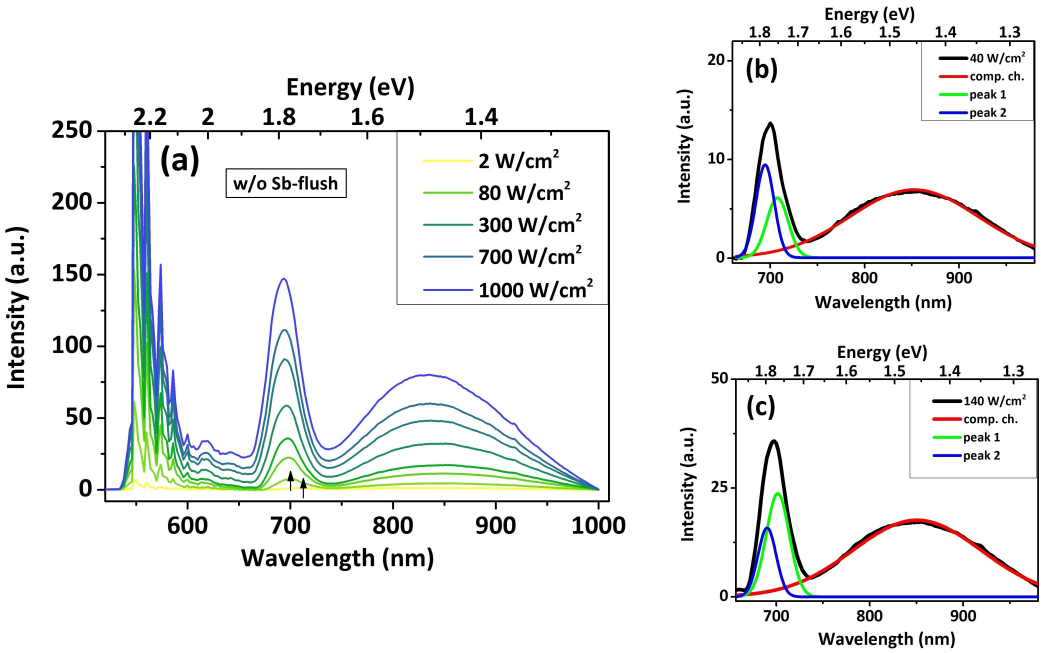

Figure 5.17: **(a)** PL measurements at T = 10 K of QD samples with 0.51 ML InGaSb QDs, without Sb-flush, 1s GRI, with varying excitation density from 2 to 1000 W·cm^{-2}. The arrows indicate the splitting of the QD emission in two peaks. **(b)** - **(c)** Examples of line-shape fits for 40 and 140 W·cm^{-2}.

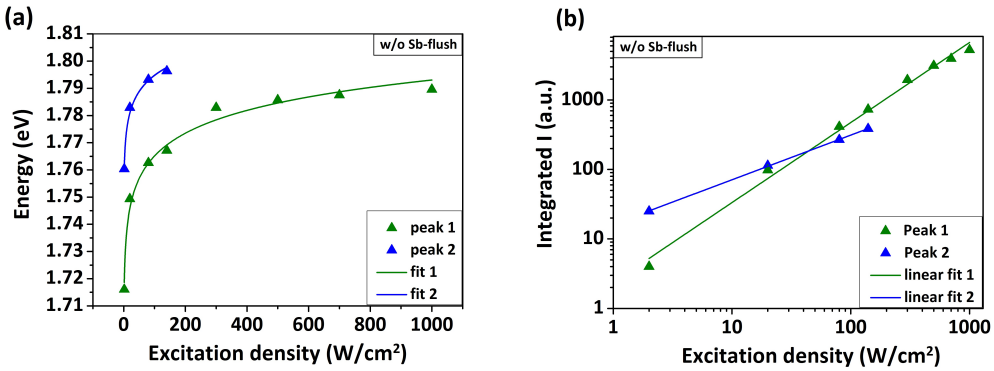

Figure 5.18: QD emission energies **(a)** and total integrated intensity **(b)** as a function of the excitation density for QDs without Sb-flush (double logarithmic plot).

t_{Sb} (s)	$peak\ 1$ (eV)	$peak\ 2$ (eV)	$peak\ 3$ (eV)
0	1.71	1.76	/
2	1.72	1.76	1.79
4	1.74	1.77	1.79

Table 5.1: QD emission energies as a function of the Sb-flush duration t_{Sb}, for the lowest applied excitation density (2 W·cm^{-2}).

t_{Sb} (s)	ΔE_1 (meV)	ΔE_2 (meV)	ΔE_3 (meV)
0	74	37	/
2	22	25	22
4	43	17	26

Table 5.2: Blueshifts of the QD emission energies for different t_{Sb} over the whole excitation power range (2 - 1000 W·cm^{-2}). The labels 1,2,3 correspond to the three peak energies shown in table. 5.1.

For instance, if electrons are localized in a finite QW in the X point at the QD/matrix interface, similarly to $In_{0.5}Ga_{0.5}As$/GaP QDs [40], the blueshift magnitude of the QD emission energy with increasing P can deviate from the conventional $P^{\frac{1}{3}}$ dependence (see also sec. 5.13).

t_{Sb} (s)	b_1	b_2	b_3
0	0.0068 $\pm$ 0.0003	0.0048 $\pm$ 0.0003	/
2	0.0022 $\pm$ 0.0003	0.0024 $\pm$ 0.0003	0.0020 $\pm$ 0.0004
4	0.0043 $\pm$ 0.0003	0.0015 $\pm$ 0.0004	0.0025 $\pm$ 0.0001

Table 5.3: Fitted exponents of the QD emission energies for different t_{Sb} over the whole excitation power range (2 - 1000 W·cm^{-2}), corresponding to the three peaks of table 5.1.

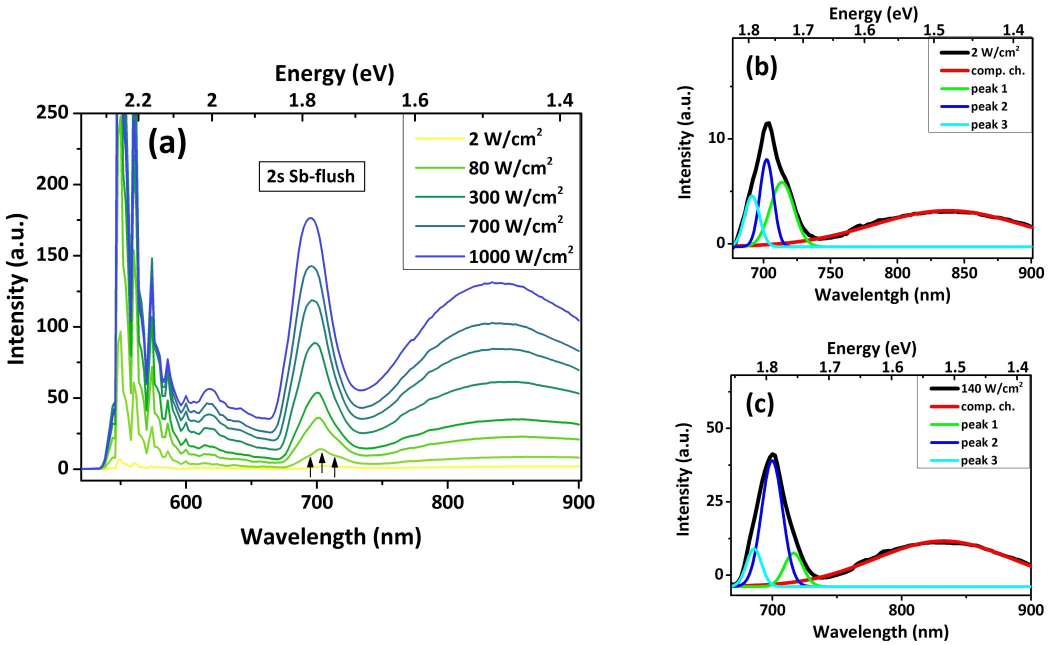

Figure 5.19: **(a)** PL measurements at T = 10 K of QD samples with 0.51 ML InGaSb QDs, without Sb-flush, 1s GRI, with varying excitation density from 2 to 1000 W·cm^{-2}. The arrows indicate the splitting of the QD emission in three peaks. **(b)** - **(c)** Examples of line-shape fits for 2 and 140 W·cm^{-2}.

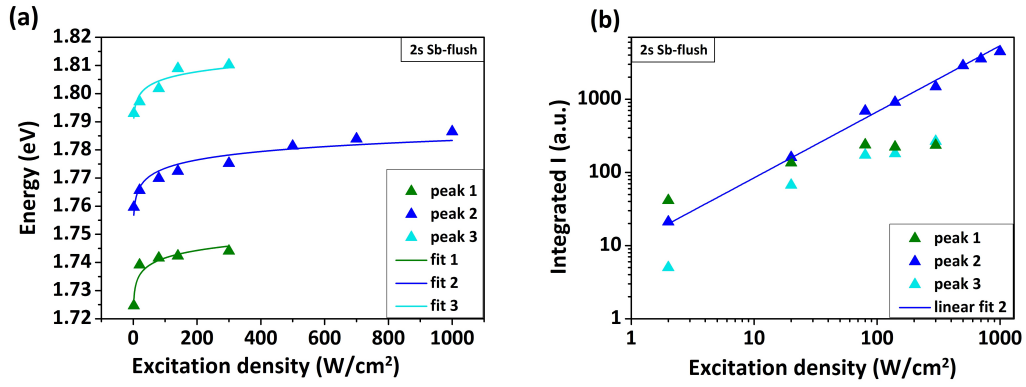

Figure 5.20: QD emission energies **(a)** and total integrated intensity **(b)** as a function of the excitation density, for QDs without Sb-flush (double logarithmic plot).

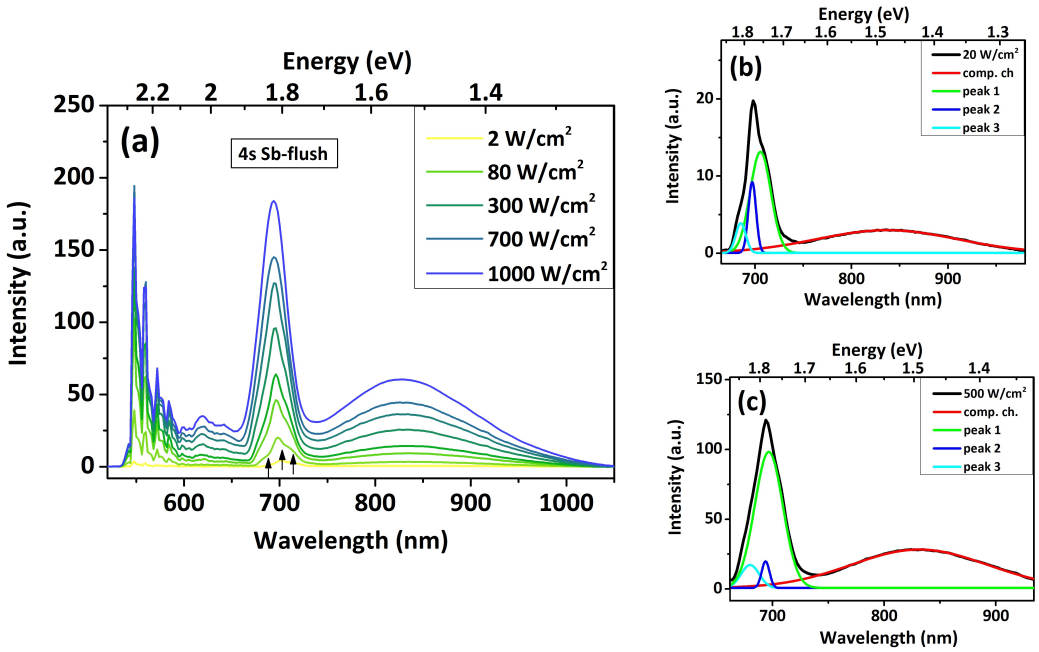

Figure 5.21: **(a)** PL measurements at T = 10 K of QD samples with 0.51 ML InGaSb QDs, 2s Sb-flush, 1s GRI, with varying excitation density from 2 to 1000 W·cm^{-2}. The arrows indicate the splitting of the QD emission in three peaks. **(b)** - **(c)** Examples of line-shape fits for 20 and 500 W·cm^{-2}.

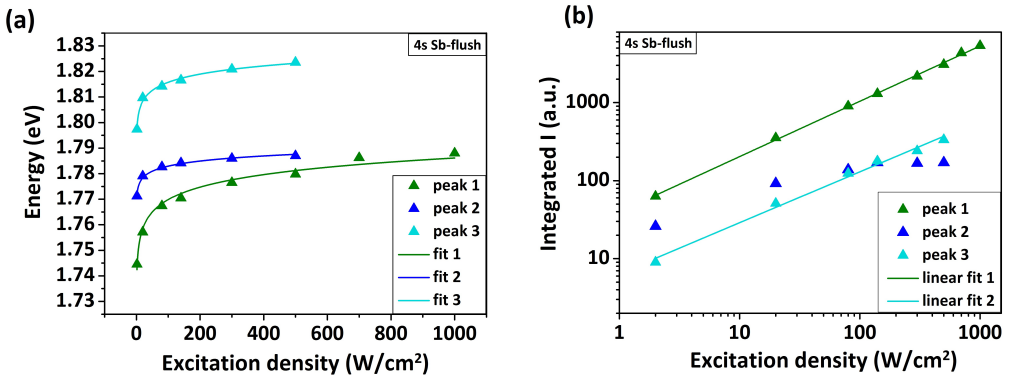

Figure 5.22: QD emission energies **(a)** and total integrated intensity **(b)** as a function of the excitation density, for QDs with 4s Sb-flush (double logarithmic plot).

In figs. 5.18 - 5.20 - 5.22 **(b)** the integrated emissions I is displayed towards the excitation density P, for each *peak* separately. For $t_{Sb} = 0$ s every emission intensity increases linearly, while for $t_{Sb} = 2$ s (*peaks* 1 and 3) and 4 s (*peak* 2) a saturation is observed, starting from $P \geq 80$ W·cm^{-2}. Such saturation is ascribed to state-filling, i.e. population of hole excited states at high excitation power [169]. This is in contrast to what usually found in type-I QDs, as for InAs/GaAs, where the occupancy of the discrete energy states is clearly distinguishable from the PL spectra by formation of characteristic "shoulders" [168]. Since type-II QDs show only hole confinement, the higher energy transitions cannot be resolved. Additionally, assuming highly populated QDs at elevated P (here for $P \geq 700$ W·cm^{-2}), many-particle effects will contribute to the smearing out of the emission spectra as distinctive behavior of type-II QDs [25].
However, a more detailed intepretation of these preliminary investigations demands theoretical calculations of multiexcitonic states of InGaSb/GaAs/GaP QDs considering their realistic physical properties, which are beyond the purpose of the present study.

5.12 Time-resolved photoluminescence investigations

Time-resolved PL transients referring to QDs grown with (blue) and without Sb-flush (black) recorded at the QD emission energy of ∼1.78 eV are presented in fig. 5.23.

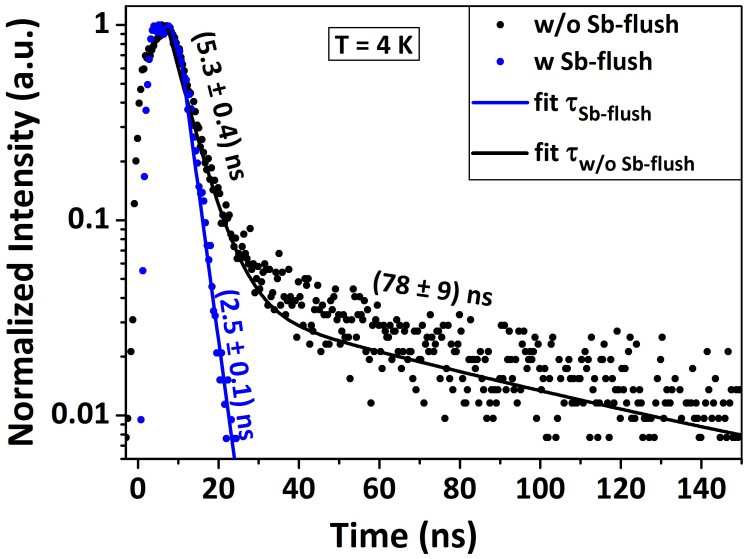

Figure 5.23: TRPL spectra (logarithmic scale) at T = 4 K of buried 0.51 ML InGaSb QDs, grown with (2 s) and without Sb-flush, corresponding to the QD emission energy of ∼1.78 eV. The solid lines display mono and biexponential fits.

Generally, the total time-dependent emission intensity I for a given number i of emission processes can be expressed as the sum of the single contributions to the emission[170]:

$$I(t) = \sum_{i=1}^{n} A_i e^{\frac{-t}{\tau_i}} \tag{5.7}$$

where A_i and τ_i are the emission rates and transition lifetimes, respectively. Following this equation, the decay spectra shown in fig. 5.23 can be fitted with exponentials to extract the respective transition lifetimes. The spectrum for the sample containing QDs without Sb-flush is fitted with a biexponential curve, which reveals two main decay processes, with associated decay time constants of $\tau_1 = (5 \pm 0.4)$ ns and $\tau_2 = (78 \pm 9)$ ns. The double decay times detected here implies the existence of two concurrent processes and can be interpreted as follows: the short component represents short-range transitions between the

hole confined in the QDs and an additional localization of electrons in the QD vicinity. Here, the thin GaAs interlayer (as QW) and/or the GaP X states at the QD/matrix interface can provide additional electron localization (see also fig. 5.24 of the next section). Initially, the electric field generated by the positively charged QDs (due to hole confinement) strongly attracts the already localized electrons, so that the carriers can recombine continuously. As the electron reservoir is reduced with time, the e-h WF overlap is also diminished, and the decay time becomes slower, reaching a more stable value. A very similar behavior was reported for GaSb/GaAs QDs by Hatami *et al.* in [171] (where the electrons were localized in the AlGaAs barriers at the QD neighborhood the QD).
Conversely, the QDs with Sb-flush show only one time constant, amounting to (2.5 ± 0.1) ns, similar to that usually found in type-I QD structures. Comparatively, the usual lifetime of InAs/GaAs QDs amounts to $\sim$2 ns [156] and reflects the high electron-hole WF overlap (assumed to be $\sim 100\%$), which determines the high transition probability. For the present case, also an enhanced e-h overlap can be deduced from the fast lifetime and can be attributed to the reduced QD size when the Sb-flush is used during QD growth (as seen in chapter 3). It is indeed well-known that the hole WF for QDs with smaller size is much more spread across the QD body [23], such that the e-h WF overlap is enhanced, and so is the recombination probability. This leads to shorter decay times, close to what one would expect from typical type-I QDs.
A further interpretation of this phenomenon can be provided by considering that every single decay process consists of contributions of both *radiative* and *non-radiative* recombination events, all occurring at the same time, such as

$$\frac{1}{\tau_{tot}} = \frac{1}{\tau_r} + \frac{1}{\tau_{nr}} \tag{5.8}$$

The single contributions of radiative and non-radiative transitions cannot be distinguished, but affect the total decay time: for instance, an increased contribution of the non-radiative recombination channel $\frac{1}{\tau_{nr}}$ would increase the overall transition rate $\frac{1}{\tau_{tot}}$, resulting in a diminished τ_{tot}. Hence, the reduction of the decay time for QDs grown with Sb-flush could be also ascribed to an increased non-radiative contribution to the transition. However, an increased non-radiative recombination would manifest itself also as reduced intensity in static PL spectra. This has not been observed so that such effect can be excluded.

5.13 Electronic configuration of InGaSb/GaAs/GaP QDs

The experimental investigations carried out so far have confirmed a strong As/Sb intermixing in the InGaSb QDs reducing the actual Sb content. In particular, the PL investigations of the present chapter have shown that the optical transition of InGaSb/GaP QDs lies around 1.8 eV, a similar spectral range of $In_{0.5}Ga_{0.5}As$/GaP QDs investigated by Stracke *et al.* in [40], i.e. $\sim$1.7 eV. Furthermore, the results of the DLTS measurements (chapter 4) concerning the hole localization energy represent an additional confirmation of a considerable part of As incorporated into QDs. Therefore, the electronic configuration of InGaSb/GaP QDs is expected to be quite close to that of $In_{0.5}Ga_{0.5}As$/GaP QDs, which has been presented in sec. 1.1.1.1. Such modeling will be considered here as a guide for the proposal of a band edge configuration of InGaSb/GaP QDs studied in this work. As already mentioned in sec. 1.1.1.1, tight-binding (TB) calculations of $In_{0.5}Ga_{0.5}As$/GaP QDs having lateral size of $\sim$20 nm and heigth of $\sim$3 nm have determined the position of the QD levels, i.e. the X states lie below the Γ states [40],[147]. This has been found to be mostly driven by strain[4], but the quantization effects provided by the QD amplify such phenomenon. Furthermore, since the GaP matrix possesses an indirect bandgap in X, the strain splits the X states at the QD/matrix interface, causing the formation of a QW where electrons can localize. A similar scenario is expected also for InGaSb/GaP QDs, since the mismatch between QDs and matrix material is even greater than that between $In_{0.5}Ga_{0.5}As$ and GaP (see also discussion in chapter 3). The splitting of the X states at the QD/matrix interface is depicted in fig. 5.24, displaying a proposal of band edge configuration of the InGaSb/GaAs/GaP QDs. The localization of electrons in such QW can explain, on one hand, the observation of the decay time discussed in the previous section, where the additional localization of electrons provided by such QW can lead to an initial increased e-h WF overlap, and on the other, deviations in the blueshift magnitude of the QD emission energy from the expected $P^{\frac{1}{3}}$. In fact, it is important to point out that this QW generated by strain and quantum confinement effects is not given by the Coulomb interaction between spatially separated charge carriers. However, the impact of the Coulomb interaction should be considered for a more precise modeling.

Finally, assuming a given amount of Sb incorporated into QDs, the valence-band discontinuity becomes larger than that of $In_{0.5}Ga_{0.5}As$/GaP QDs, and thus the Γ and X states of the QD are expected to lie at higher energies in the conduction band. The energy transition may become therefore indirect in both real and reciprocal space, occurring thus between electrons in the X states and holes localized in the QD. The hole localization energy amounts to $\sim$ 400 meV, according to the DLTS measurements (also displayed in fig. 5.24).

[4] The strain generated by the lattice mismatch is tensile in GaP, while compressive in the QD.

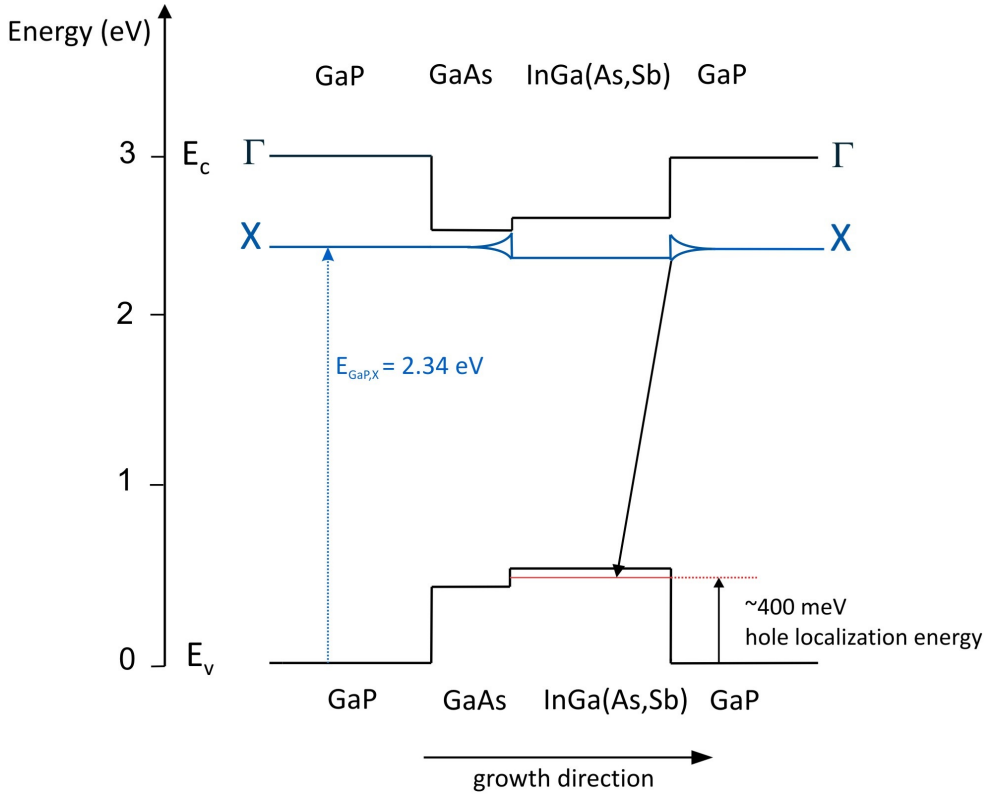

Figure 5.24: Schematic depiction of the proposed band edge configuration for a InGaSb/GaAs/GaP QD at **k**=0. $E_{GaP,X}$ represents the indirect bandgap of GaP in X. The energy transition between electrons in the X states and QD hole states is also displayed.

Summary

- The optical properties of the InGaSb/GaAs/GaP QDs have been studied in detail. TEM-CL investigations confirm the emission from the QD layer, which is detected around 1.8 eV at T = 15 K. Introducing GRI and Sb-flush has been found to remarkably improve the QD luminescence.

- Static temperature-dependent investigations reveal unusual properties of such QDs, such as two distinctive carrier delocalization processes for the temperature range of 10 - 60 K and 150 K - 300 K. Such mechanisms are not observed in type-I QDs and are attributed to the particular QD configuration (high density and type-II indirect QDs).

- Excitation density dependent PL studies show a blueshift of the QD emission energies. The observed shift is reduced compared to that usually expected for type-II QDs, and not depending on the third root of the excitation density. However, variations from such behavior have been recently also observed for other type-II QD heterostructures, and can be due to the complex band edge configuration and the specific QD physical properties.

- TRPL measurements show different carrier dynamics for QDs grown with and without Sb-flush. The use of Sb-flush leads to smaller and more homogeneous QDs (as already shown in chapter 3), and has a strong impact on the carrier radiative lifetimes, by means of an increased e-h WF overlap. This leads to shorter decay times, comparable to those found in type-I QDs.

- PL investigations have confirmed a noticeable As/Sb intermixing in InGaSb/GaP QDs, as previously suggested by the structural and the DLTS investigations on such QDs. Therefore, an electronic structure close to that of $In_{0.5}Ga_{0.5}As$/GaP QDs is expected. Finally, a proposal of a band edge configuration has been derived from the experimental results carried out in this work.

Chapter 6

Summary and comparison with $In_{0.5}Ga_{0.5}As$/GaAs QDs on GaP

" Basically, I like research because research is like to solve the quiz, you know. Always there is a problem, and I have to solve the problem. So I like those patterns. It's almost like research is sort of a quiz. "

S. Nakamura

The growth of InGaSb QDs on GaP has been enabled by using a thin GaAs insertion, also called *interlayer*, with thickness of 5 ML. The lattice mismatch between nominal $In_{0.5}Ga_{0.5}Sb$ and GaP amounts to $\sim 13\%$, which represents a challenging value for enabling a Stranski-Krastanow defect-free QD formation. The strain energy accumulated in the GaAs interlayer grown on bare GaP contributes to the total energy required for 3D island formation, such that the following deposition a sub-ML amount of highly-mismatched InGaSb abruptly induces the 2D/3D phase-transition. Conversely, the lattice mismatch between $In_{0.5}Ga_{0.5}As$ and GaP is $\sim 6.9\%$, theoretically enabling the QD formation without any pretreatments of the GaP surface. However, a thin GaAs interlayer was used also for that material combination, but its thickness was $\sim$2 ML [40]: it served solely to modify the GaP surface energetics, by means of modification of the surface termination from P- to As-. The critical coverage of $In_{0.5}Ga_{0.5}As$ for QD formation on 2.2 ML GaAs/GaP was $\sim$0.52 ML, and QDs had a density of $\sim 5{\cdot}10^7$ cm^{-2}, whereas for InGaSb QDs on 5 ML GaAs/GaP the critical thickness amounts to $\sim$0.21 ML. QDs of both heterostructures show comparable dimensions but for InGaSb a much higher QD density is detected: here, a greater accumulation of elastic energy due to the thicker interlayer and highly-mismatched InGaSb leads to the formation of two orders of magnitude more QDs. The relatively thick

interlayer results in a significant intermixing between GaAs and QDs, as deduced from the dependence of the GaAs interlayer thickness and QD density (and aspect ratio), together with the TEM investigations carried out on buried QDs. In fact, an homogeneously closed GaAs layer beneath the QDs cannot be identified. Hence, the partial incorporation of GaAs into QDs apparently leads to formation of islands at the GaAs interface, resulting in ML-fluctuations. This finds also evidence in the photoluminescence spectra of QDs, where the luminescence detected between 1.9 and 2 eV can be related to emission of such ML-fluctuations. Luminescence from the QD-layer is confirmed by TEM-CL investigations: the spectral position of the InGaSb QD emission is detected between 1.74 and 1.88 eV, similarly to what was found for $In_{0.5}Ga_{0.5}As$, i.e. $\sim$ 1.7 eV [40], additionally supporting incorporation of large parts of As into QDs.
DLTS investigations aiming to determine the hole localization energy and capture cross-section at room temperature have been carried out on different dedicated n^+-*p*-samples. In particular, by *charge-selective* DLTS on "*only-QDs*" the highest localization energy of QDs was measured to (0.370 $\pm$ 0.008) eV. This value is less than the predicted 0.6 eV for the VBO between QDs of nominal $In_{0.5}Ga_{0.5}Sb$ and GaP matrix and lies in between the prediction for $In_{0.5}Ga_{0.5}As$ and $In_{0.5}Ga_{0.5}Sb$, i.e. between 0.3 and 0.6 eV. This deviation confirms again a strong intermixing between As and Sb in QDs. DLTS investigations on InGaSb QDs with an additional AlP barrier, i.e "*QD-barr*", has yielded a localization energy E_{loc} = (1.15 $\pm$ 0.02) eV, which is comparable to that of $In_{0.5}Ga_{0.5}As$/AlP/GaP QDs, amounting to (1.14 $\pm$ 0.04) eV [107]. On the other hand, the associated QD capture cross-section for InGaSb/AlP/GaP has been decreased by one order of magnitude, namely from (8 $\pm$ 5) $\cdot 10^{-10}$ to (9 $\pm$ 5) $\cdot 10^{-11}$ cm^2. Thereby, an improvement of the storage time of $In_{0.5}Ga_{0.5}As$/AlP/GaP QDs of (230 $\pm$ 60) s of one order to magnitude to (3200 $\pm$ 300) s is obtained. This has been ascribed to the use of Sb instead of As in QD growth, which has affected the hole capture processes into QDs.
The use of an Sb-flush before the QD deposition has been found to strongly affect the QD formation: QDs become on average smaller and more homogeneous if Sb is supplied before depositing the InGaSb material. Simultaneously, the defect formation is suppressed. Such behavior is typical of surfactants, surface-active species usually employed in epitaxial growth in order to modify the surface energetics.
Through the employment of a growth interruption (GRI) after the InGaSb QD formation, a ripening occurs. In particular, for prolonged GRIs (800 s), the material transfer between the 3D islands is vanishing. This is due to two reasons: the rather low V/III ratio ($\sim$0.3) and the use of Sb during QD growth. In comparison, $In_{0.5}Ga_{0.5}As$/GaP QDs [40] grown at a much higher V/III ratio of $\sim$ 5 show a different behavior: there, the QDs exhibited defects already after a GRI of 400 s, which means a larger material transfer between the 3D islands. Hence, utilizing a lower V/III ratio together with Sb during the InGaSb QD growth suppresses defect formation during the ripening time, thereby leading to a more

stable QD configuration. Additionally, adjusting these two growth parameters, namely employing an Sb-flush and an extended GRI during QD growth, has led to a remarkable improvement of the overall QD luminescence.
Static temperature-dependent investigations reveal peculiar properties of InGaSb QDs, such as two delocalization processes, resulting in an initial blueshift in the temperature range of 10 - 60 K and a weaker temperature dependence of the bandgap shrinkage for 150 $\leq T \leq$ 300 K, compared to the common Varshni trend. Excitation density dependent PL studies exhibit a diminished blueshift of the QD emission energy, i.e. not depending on the third root of the excitation density, usually expected for type-II QDs, as for GaSb/GaAs. Finally, dynamic PL investigations by means of TRPL show different carrier dynamics for QDs grown with and without Sb-flush. The reduction of the average QD size due to the Sb-flush has apparently led to an increased e-h WF overlap, resulting in faster decay times. These PL investigations suggest a rather complex electronic structure of InGaSb/GaAs/GaP QDs, which should stimulate further theoretical simulations, taking into account the QD physical properties as chemical composition, size and strain effects.

Outlook

"Es ist des Lernens kein Ende."

"There is no end in learning."

R. Schumann

This work exploited MOVPE-growth to realize Sb-based QDs in GaP matrix, and to extend the storage time of holes trapped into such QDs for their use in nanoscale memory applications, namely the QD-Flash. Employing Sb instead of As in QD growth has improved the storage time up to one hour at room temperature, reaching the record for MOVPE-grown QDs so far. This is primarily due to the QD capture cross-section, reduced by one order of magnitude through the use of Sb during QD growth. A further understanding of this process requires on one hand a more detailed chemical analysis of the QD composition, and on the other hand a theoretical modeling of capture processes of holes into QDs. Then, decisive steps towards non-volatility would be possible by engineering of the capture cross-section through variation of the QD properties. In fact, once such methods are available, the measured localization energy E_{loc}= (1.15 $\pm$ 0.02) eV for InGaSb/AlP/GaP QDs would already meet the requirements for non-volatility, provided that the capture cross-section be reduced to $\sigma_\infty = 10^{-14}$ cm^2. In MOVPE, efforts should be made towards the reduction of the As/Sb intermixing in QDs, possibly enabling growth of rather pure $In_{0.5}Ga_{0.5}Sb$ QDs. This would enhance the localization energy for $In_{0.5}Ga_{0.5}Sb$/AlP/GaP QDs by an additional $\sim$ 0.3 eV, according to theoretical predictions, thus reaching E_{loc} = 1.45 eV, additionally making non-volatility feasible. The GRI and the Sb-flush have been found to be two essential factors remarkably affecting the structural and optical properties of QDs: they might be therefore employed to control the capture cross-section of QDs in the future.
In conclusion, the material combination InGaSb/AlP/GaP studied in this work represents a promising candidate for the future QD-Flash. Certainly, non-volatility can also be achieved by using other material combinations for QDs and matrix, as for GaSb QDs embedded in $Al_{0.51}In_{0.49}P$, where the localization energy of sole QDs is estimated to be $\sim$1.25 eV [12].

Appendix A

GaP substrate preparation before epitaxial growth: wet chemical treatments

The GaP substrates used for the growth experiments carried out in this work were declared by the vendor as *epi-ready*. This should ensure good epitaxial outcomes without any other additional surface pre-treatments. Each GaP substrate batch has been tested before fabricating any kind of epitaxial structure. The tests have been carried out by growing GaP:un epilayers employing the growth conditions usually used for the buffer layers, i.e. growth temperature T_g = 750 °C, V/III $\sim$ 175 and growth rate 2 μm/h. Unfortunately, such growth on GaP without pre-treatment yielded poor surface morphologies, namely increased surface roughness and defects. To overcome this issue, a wet chemical pre-treatment of the GaP wafers has been exploited, before starting with the growth. The etching procedure consists of dipping the substrates in different chemical solutions and rinsing in deionized water between each step, as listed in table A.1. Every etching procedure has been carried out on one single wafer at a time. Firstly, the wafer is put in a degreasing solution consisting of solely sulfuric acid (H_2SO_4) for 10 minutes (step **1**). Thereafter, it is rinsed in purified water for more than 10 mins (step **2**). In the meantime, the second chemical solution is prepared, i.e. diluted *aqua regia*, as indicated by the steps nr. **3** - **4**: 4 parts of hydrochloric (HCl) and nitric acid (HNO_3) are mixed for 8 min. The purpose of using such diluted solution is to keep the etch rate low. Generally, the etching process achieved by *aqua regia* consists of oxidation and dissolution. Both chlorine (Cl^-) and nitrate (NO_3^-) ions oxidize the GaP surface atoms [172]. As a result, a passive oxide film is formed, which is found to be particularly soluble: phosphorous and gallium oxides can be therefore easily attack by Cl^- and dissolved within the solution. The detailed description of the etching mechanism of GaP by using *aqua regia* can be found in [172].

Step	Chemical solution	Duration (min)
1	H_2SO_4 (96%)	10
2	H_2O	$\geq$10
3	4 HCl (37%) : 4 HNO_3 (69.5%)	8
4	4 HCl (37%) : 4 HNO_3 (69.5%) : 5 H_2O	5
5	H_2O	$\geq$10

Table A.1: Etching recipe used for the wet chemical treatment of GaP wafers before the usual epitaxial growth. The chemical solutions and durations of each step are also indicated.

The general reaction leading to the formation of *aqua regia* is the following [173]:

$$HNO_3 + 3HCl \rightarrow NOCl + Cl_2 + 2H_2O \quad \text{(A.1)}$$

Here, 4 parts of HCl and HNO_3 are mixed and the balanced reaction can thus be written as:

$$4HNO_3 + 12HCl \rightarrow 4NOCl + 4Cl_2 + 8H_2O \quad \text{(A.2)}$$

This solution is then diluted with 5 parts of water to reduce its concentration, leading to:

$$4HNO_3 + 12HCl + 5H_2O \rightarrow 4NOCl + 4Cl_2 + 13H_2O \quad \text{(A.3)}$$

The sample is then put in such mixture for 5 minutes (step **4**). This chemical solution is used to prepare a clean surface, thereby removing possible adsorbed metallic impurities and surface microroughnesses. The treatment ends with rinsing in water for more than 10 min (step **5**), to remove any chemical residuals from the surface. Finally, the wafers are dried with nitrogen. After employing this etching procedure, the GaP MOVPE growth has been tested. In fig. A.2, the surface of 1 μm GaP:un deposited on a pre-treated wafer is presented: it appears mirror-like without any surface roughness.

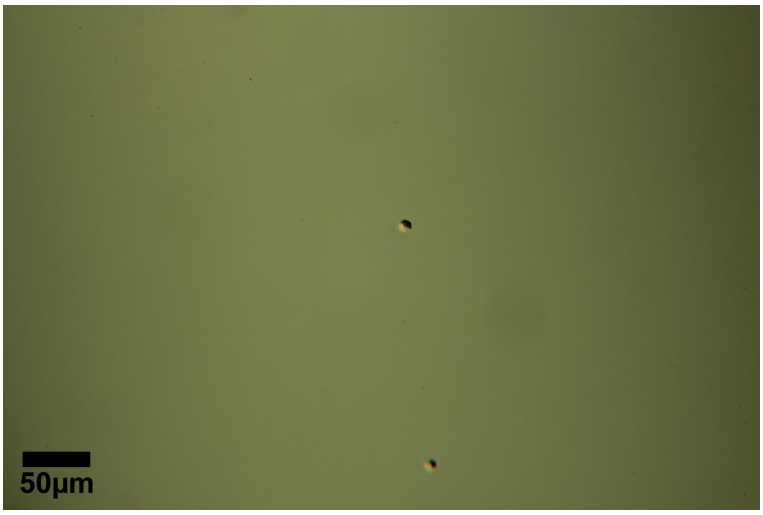

Figure A.1: Nomarski micrograph of a 1 μm GaP:un epilayer grown after the chemical pre-treatment.

This successful chemical pre-treatment has been therefore employed for every wafer before carrying out the MOVPE growth. On the surface some defects with a characteristic hexagonal shape can be detected, having a density of $\sim 10^3$ cm^{-2}. They lie in the range of the EPD[1] declared by the wafer supplier, which varies between $\sim 10^3$ and $\sim 10^5$ cm^{-2}.

[1]EPD stands for *etch pits density* and usually defines the quality of a semiconductor wafer. In correspondence of crystal dislocations, the etching rate is enhanced, so that through the application of special etching solutions, defects or *pits* are formed. In this way, the density of such crystal defects can be easily determined.

Bibliography

[1] G. Moore, *Cramming more components onto integrated circuits*, Electronics **8**, 114 (1965).

[2] *Overall Technology Roadmap Characteristics*, International Technology Roadmap for Semiconductors (2010).

[3] H. Iwai, *CMOS downsizing toward sub-10 nm*, Solid-State Electronics **48**, 497 (2004).

[4] B. Doris, M. Ieong, T. Kanarsky, R. A. Roy, O. Dokumaci, Z. Ren, F.-F. Jamin, L. Shi, W. Natzle, H.-J. Huang, J. Mezzapelle, A. Mocuta, S. Womack, M. Gribelyuk, E. C. Jones, R. J. Miller, H.-S. P. Wong, and W. Haensch, *Extreme scaling with ultra-thin Si channel MOSFETs*, in IEDM Tech. Dig., 267 (2002).

[5] N. Chatterjee, M. Shevgoor, R. Balasubramonian, A. Davis, Z. Fang, R. Illikkal und R. Iyer, *Leveraging Heterogeneity in DRAM Main Memories to Accelerate Critical Word Access*, Proc. of the 45th Annual IEEE/ACM International Symposium on Microarchitecture, 13-24 (2012).

[6] V. Cuppu, B. Jacob, B. Davis and T. Mudge, *A performance comparison of contemporary DRAM architectures*, Proc. of the 26th International Symposium on Computer Architecture, 222-233 (1999).

[7] A. Marent and D. Bimberg, *Speicherzelle*, German Patent N. 10 2011 006 7825 (2012).

[8] D. Bimberg, M. Geller, A. Marent, and T. Nowozin, *Memory*, U.S. Patent N. 8331142 B2 (2012).

[9] A. Marent, T. Nowozin, M. Geller and D. Bimberg, *The QD-Flash: a quantum dot-based memory device*, Semicond. Sci. Technol. **26**, 14026 (2011).

[10] A. Marent, T. Nowozin, J. Gelze, F. Luckert, and D. Bimberg, *Hole-based memory operation in an InAs/GaAs quantum dot heterostructure*, Appl. Phys. Lett. **95**, 242114 (2009).

[11] I. N. Stranski and L. Krastanow, *Zur Theorie der orientierten Ausscheidung von Ionenkristallen aufeinander*, Abhandlungen der Mathematisch-Naturwissenschaftlichen Klasse IIb. Akademie der Wisseschaften Wien **146**, 797 (1938).

[12] D. Bimberg, A. Marent, T. Nowozin, and A. Schliwa, *Antimony-based quantum dots memory*, Proc. of SPIE **7947**, 79470L-1 (2011).

[13] I. Vurgaftman, J. R. Meyer and L. R. Ram-Mohan, *Band parameters for III-V compound semiconductors and their alloys*, J. Appl. Phys. **89**, 5815 (2001).

[14] T. J. Grassman, J. A. Carlin, B. Galiana, L.-M. Yang, F. Yang, M. J. Mills, and S. A. Ringel, *Nucleation-related defect-free GaP/Si(100) heteroepitaxy via metal-organic chemical vapor deposition*, Appl. Phys. Lett. **102**, 142102 (2013).

[15] A. Beyer, J. Ohlmann, S. Liebich, H. Heim, G. Witte, W. Stolz, and K. Volz, *GaP heteroepitaxy on Si(001): Correlation of Si-surface structure, GaP growth conditions, and Si-III/V interface structure*, J. Appl. Phys. **111**, 083534 (2012).

[16] M. Geller, E. Stock, C. Kapteyn, R. L. Sellin, and D. Bimberg, *Tunneling emission from self-organized In(Ga)As/GaAs quantum dots observed via time-resolved capacitance measurements*, Phys. Rev. B **73**, 205331 (2006).

[17] M. A. Kastner, *Artificial atoms*, Phys. Today, **43**, 24 (1993).

[18] A. I. Ekimov and A. A. Onushchenko, *Quantum size effect in three-dimensional microscopic semiconductor crystals*, JETP Lett. **34**, 345 (1981).

[19] M. Grundmann, O. Stier and D. Bimberg, *InAs/GaAs pyramidal quantum dots: Strain distribution, optical phonons, and electronic structure*, Phys. Rev. B **52**, 11969 (1995).

[20] U. Woggon, *Optical properties of semiconductor quantum dots*. Springer-Verlag GmbH (1997). ISBN: 978- 3540609063.

[21] R. Bratschitschand and A. Leitenstorfer, *Quantum dots: Artificial atoms for quantum optics*, Nat. Mater. **5**, 855-856 (2006).

[22] M. Reed, J. Randall, R. Aggarwal, R. Matyi, T. Moore and A. Wetsel, *Observation of descrete electronic states in a zero-dimensional semiconductor nanostructure*, Phys. Rev. Lett. **60**, 535 (1988).

[23] O. Stier, M. Grundmann, and D. Bimberg, *Electronic and optical properties of strained quantum dots modeled by 8-band* $\mathbf{k}\cdot\mathbf{p}$ *theory*, Phys. Rev. B **59**, 5688 (1999).

[24] A. J. Williamson, A. Franceschetti, H. Fu, L. W. Wang, and A. Zunger, *Indirect band gaps in quantum dots made from direct-gap bulk materials*, J. Electr. Mat. **28**, 5 (1999).

[25] L. Müller-Kirsch, R. Heitz, A. Schliwa, O.Stier, D. Bimberg, H. Kirmse, and W. Neumann, *Many-particle effects in type-II quantum dots*, Appl. Phys. Lett. **78**, 1418 (2001).

[26] U. E. H. Laheld, F. B. Pedersen, and P. C. Hemmer, *Excitons in type-II quantum dots: Finite offsets*, Phys. Rev. B **52**, 2697 (1995).

[27] P. Klenovský, V. Křapek, D. Munzar, and J. Humlíček, *Electronic structure of InAs quantum dots with GaAsSb strain reducing layer: Localization of holes and its effect on the optical properties*, Appl. Phys. Lett. **97**, 203107 (2010).

[28] K. Nishikawa, Y. Takeda, K. Yamanaka, T. Motohiro, D. Sato, J. Ota, N. Miyashita, and Y. Okada, *Over 100 ns intrinsic radiative recombination lifetime in type II InAs/GaAs$_{1-x}$Sb$_x$ quantum dots* J. Appl. Phys. **111**, 044325 (2012).

[29] J. He, C. J. Reyner, B. L. Liang, K. Nunna, D. L. Huffaker, N. Pavarelli, K. Gradkowski, T. J. Ochalski, G. Huyet, V. G. Dorogan, Yu. I. Mazur, and G. J. Salamo, *Band Alignment Tailoring of InAs$_{1-x}$Sb$_x$/GaAs Quantum Dots: Control of Type I to Type II Transition*, Nano Lett. **10**, 3052 (2010).

[30] S. Muto, *On a Possibility of Wavelength-Domain- Multiplication Memory Using Quantum Boxes*, Jpn. J. Appl. Phys., **34**, L210 (1995).

[31] M. C. Bödefeld, R. J. Warburton, K. Kanai, J. P. Kotthaus, G. Medeiros-Ribeiro, and P. M. Petroff, *Storage of electrons and holes in self-assembled InAs quantum dots*,Appl. Phys. Lett. **74**, 1839 (1999).

[32] T. Nowozin, L. Bonato, A. Högner, A. Wiengarten, D. Bimberg, Wei-Hsun Lin, Shih-Yen Lin, C. J. Reyner, Baolai L. Liang, and D. L. Huffaker, *800 meV localization energy in GaSb/GaAs/Al$_{0.3}$Ga$_{0.7}$As quantum dots*, Appl. Phys. Lett. **102**, 052115 (2013).

[33] H. Kroemer and G. Griffiths, *Staggered-lineup heterojunctions as sources of tunable below-gap radiation: Operating principle and semiconductor selection*, IEEE Elec. Dev. Lett. **4**, 20 (1983).

[34] H. K. Choi, G. W. Turner, and H. Q. Le, *InAsSb strained quantum-well lasers emitting in the 4-μm band*, Proc. of the Quantum Electronics and Laser Science Conference, Optical Society of America (1995).

[35] D. W. Stokes, L. J. Olafsen, W. W. Bewley, I. Vurgaftman, C. L. Felix, E. H. Aifer, J. R. Meyer, and M. J. Yang, *Type-II quantum-well "W" lasers emitting at λ = 5.4 – 7.3 μm*, J. Appl. Phys. **86**, 4729 (1999).

[36] R. B. Laghumavarapu, A. Moscho, A. Khoshakhlagh, M. El-Emawy, L. F. Lester, and D. L. Huffaker, *GaSb/GaAs type II quantum dot solar cells for enhanced infrared spectral response*, Appl. Phys. Lett. **90**, 173125 (2007).

[37] J. M. Llorens, L. Wewior, E. R. Cardozo de Oliveira, J. M. Ulloa, A. D. Utrilla, A. Guzmán, A. Hierro, and B. Alén, *Type-II InAs/GaAsSb quantum dots: highly tunable exciton geometry and topology*, Appl. Phys. Lett. **107**, 183101 (2015).

[38] G. Burkard, D. Loss, D. P. Di Vincenzo, *Coupled quantum dots as quantum gates*, Phys. Rev. B **59**, 3 (1999).

[39] P. Klenovský, V. Křapek, and J. Humlíček, *Type-II InAs/GaAsSb/GaAs quantum dots as artificial quantum dot molecules*, Acta Physica Polonica A, **129**, 62 (2016).

[40] G. Stracke, E. M. Sala, S. Selve, T. Niermann, A. Schliwa, A. Strittmatter, and D. Bimberg, *Indirect and direct optical transitions in $In_{0.5}Ga_{0.5}As/GaP$ quantum dots*, Appl. Phys. Lett. **104**, 123107 (2014).

[41] A. Schliwa, M. Winkelnkemper and D. Bimberg, *Impact of size, shape, and composition on piezoelectric effects and electronic properties of In(Ga)As/GaAs quantum dots*, Phys. Rev. B **76**, 205324 (2007).

[42] C. Robert, C. Cornet, P. Turban, T. N. Thanh, M. O. Nestoklon, J. Even, J. M. Jancu, M. Perrin, H. Folliot, T. Rohel, S. Tricot, A. Balocchi, D. Lagarde, X. Marie, N. Bertru, O. Durand, and A. Le Corre, *Electronic, optical, and structural properties of (In,Ga)As/GaP quantum dots*, Phys. Rev. B **86**, 205316 (2012).

[43] J.-M. Jancu, R. Scholz, F. Beltram, and F. Bassani, *Empirical spds* tight-binding calculation for cubic semiconductors: General method and material parameters*, Phys. Rev. B **57**, 6493 (1998).

[44] J. Chelikowsky and M. Cohen, *Nonlocal pseudopotential calculations for the electronic structure of eleven diamond and zinc-blende semiconductors*, Phys. Rev. B **14**, 556 (1976).

[45] F. C. Frank and J. H. Van der Merwe. *One-dimensional dislocations. I. Static theory*, Proc. R. Soc. London, Ser. A, **198**, 205 (1949).

[46] M. Volmer and A. Weber, *Keimbildung in übersättigten Gebilden*, Z. phys. Chem. **119**, 277 (1926).

[47] P. Kratzer, Q. K. K. Liu, P. Acosta-Diaz, C. Manzano, G. Costantini, R. Songmuang, A. Rastelli, O. G. Schmidt, and K. Kern, *Shape transition during epitaxial growth of InAs quantum dots on GaAs(001): Theory and experiment.* Phys. Rev. B **40**, 205347 (2006).

[48] F. Heinrichsdorff, A. Krost, D. Bimberg, A. O. Kosogov, P. Werner, *Self organized defect free InAs/GaAs and InAs/InGaAs/GaAs quantum dots with high lateral density grown by MOCVD*, Appl. Surf. Sci. **123**, 725 (1998).

[49] C. Ratcliff, T. J. Grassman, J. A. Carlin, and S. A. Ringel, *High temperature step-flow growth of gallium phosphide by molecular beam epitaxy and metalorganic chemical vapor deposition*, Appl. Phys. Lett. **99**, 141905 (2011).

[50] M. V. Maximov, L. V. Asryan, Yu. M. Shernyakov, A. F. Tsatsul'nikov, I. N. Kaiander, V. V. Nikolaev, A. R. Kovsh, S. S. Mikhrin, V. M. Ustinov, A. E. Zhukov, Zh. I. Alferov, N. N. Ledentsov, and D. Bimberg, *Gain and threshold charcteristics of long wavelength lasers based on InAs/GaAs quantum dots formed by activated alloy phase separation*, IEEE J. Quantum Electron. **37**, 676 (2001).

[51] M. Grundmann and D. Bimberg, *Gain and threshold of quantum dot lasers: theory and comparison to experiments*, Jpn. J. Appl. Phys. **36**, 4181 (1997).

[52] N. N. Ledenstov, F. Hopfer, and D. Bimberg, *High-speed quantum-dot vertical-cavity surface-emitting lasers*, IEEE J. Sel. Top. Quantum Electron, **95**, 1741 (2007).

[53] F. Hopfer, A. Mutig, M. Kuntz, G. Fiol, and D. Bimberg, *Single-mode submonolayer quantum dot vertical-cavity surface-emitting lasers with high modulation bandwidth*, Appl. Phys. Lett. **89**, 141106 (2006).

[54] P. Borri, S. Schneider, W. Langbein and D. Bimberg, *Ultrafast carrier dynamics in InGaAs quantum dot material and devices*, J. Opt. A **8**, 33 (2006).

[55] S. Dommers, V. V. Temnov, and U. Woggon, *Complete ground state gain recovery after ultra-short double pulses in quantum dot based semiconductor optical amplifier*, Appl. Phys. Lett. **90**, 033508 (2007).

[56] V. Popescu, G. Bester, M. C. Hanna, A. G. Norman, and A. Zunger, *Theoretical and experimental examination of the intermediate-band concept for strain-balanced (In,Ga)As/Ga(As,P) quantum dot solar cells*, Phys. Rev. B **78**, 205321 (2008).

[57] M. Geller, A. Marent and D. Bimberg, in *Handbook of Nanophysics: Nanoelectronics and Nanophotonics*, edited by K. D. Sattler (CRC Press, Boca Raton, FL, 2010), Sect. 2.1.

[58] M. Geller, A. Marent, and D. Bimberg, *Nanomemories Using Self-Organized Quantum Dots*, in Handbook of Nanophysics, Vol. 6: Nanoelectronics and Nanophotonics, Sec. **2**-I, Edited by Klaus D. Sattler, CRC Press (2010).

[59] A. Schliwa, M. Winkelnkemper, and D. Bimberg, *Few-particle energies versus geometry and composition of $In_xGa_{1-x}As/GaAs$ self-organized quantum dots*, Phys. Rev. B **79**, 075443 (2009).

[60] M. Geller, A. Marent, E. Stock, D. Bimberg, V. I. Zubkov, I. S. Shulgunova und A. V. Solomonov, *Hole capture into self-organized InGaAs quantum dots*, Appl. Phys. Lett. **89**, 232105 (2006).

[61] M. Geller, A. Marent, T. Nowozin, D. Bimberg, N. Akcay and N. Öncan, *A write time of 6 ns for quantum dot-based memory structures*, Appl. Phys. Lett. **92**, 92108 (2008).

[62] T. Nowozin, A. Beckel, D. Bimberg, A. Lorke und M. Geller, *3 ns single-shot read-out in a quantum dot-based memory structure*, Appl. Phys. Lett. **104**, 053111 (2014).

[63] T. Nowozin, A. Marent, M. Geller, D. Bimberg, N. Akcay, and N. Oncan, *Temperature and electric field dependence of the carrier emission processes in a quantum dot-based memory structure*, Appl. Phys. Lett. **94**, 042108 (2009).

[64] T. Nowozin, *Self-Organized Quantum Dots for Memories, Electronic Properties and Carrier Dynamics*, Springer Berlin (2014), ISBN 978-3-319-01969-7.

[65] D. V. Lang, *Deep-level transient spectroscopy: A new method to characterize traps in semiconductors*, J. Appl. Phys. **45**, 3023 (1974).

[66] A. Marent, M. Geller, and D. Bimberg, *A novel nonvolatile memory based on self-organized quantum dots*, Microelectron. J. **40**, 492 (2009).

[67] H. M. Manasevit and W. I. Simpson, *The Use of Metal–Organic in the Preparation of Semiconductor Materials: I. Epitaxial Gallium Compounds*, J. Electrochem. Soc. **116**, 1725 (1969).

[68] G. B. Stringfellow, *Organometallic vapor-phase epitaxy: theory and practice*, Academic Press (1999), ISBN 978-0-12-673842-1.

[69] P. M. Petroff and S. P. DenBaars, *MBE and MOCVD growth and properties of self-assembling quantum dots arrays in III-V semiconductor structures*, Superlattices and Microstructures **15**, 1 (1994).

[70] T. Fukui, S. Ando, Y. Tokura, and T. Toriyama, *GaAs tetrahedral quantum dot structures fabricated using selective area metalorganic chemical vapor deposition*, Appl. Phys. Lett. **58**, 2018 (1991).

[71] R. M. Biefeld, *The preparation of device quality Gallium Phosphide by metal organic chemical vapor deposition*, J. Cryst. Growth **56**, 382—388 (1982).

[72] G. B. Stringfellow, *A critical appraisal of growth mechanisms in MOVPE*, J. Cryst. Growth **68**, 111 (1984).

[73] G. Binnig, C.F. Quate and Ch. Gerber, *Atomic Force Microscope*, Phys. Rev. Lett. **56**, 930 (1986).

[74] N. Yu and A. A. Polycarpou, *Adhesive contact based on the Lennard-Jones potential: a correction to the value of the equilibrium distance as used in the potential*, J. Colloid Interface Sci. **278**, 428 (2004).

[75] F. J. Giessibl, *Advances in atomic force microscopy*, Rev. Mod. Phys. **75**, 949 (2003).

[76] E. Ruska, *The development of the electron microscope and of electron microscopy*, Rev. Mod. Phys. **59**, 3 (1987).

[77] J. Christen, M. Grundmann and D. Bimberg, *Scanning cathodoluminescence microscopy: A unique approach to atomic-scale characterization of heterointerfaces and imaging of semiconductor inhomogeneities*, J. Vac. Sci. Technol., B **9**, 2358 (1991).

[78] E. M. Sala, G. Stracke, S. Selve, T. Niermann, M. Lehmann, S. Schlichting, F. Nippert, G. Callsen, A. Strittmatter, and D. Bimberg, *Growth and structure of $In_{0.5}Ga_{0.5}Sb$ quantum dots on GaP(001)*, Appl. Phys. Lett. **109**, 102102 (2016).

[79] D. S. Abramkin, V. T. Shamirzaev, M. A. Putyato, A. K. Gutakovskii, and T. S. Shamirzaev, *Coexistence of Type-I and Type-II Band Alignment in Ga(Sb, P)/GaP Heterostructures with Pseudomorphic Self-Assembled Quantum Dots*, JETP Lett. **99**, 76 (2014).

[80] D. S. Abramkin, E. A. Emelyanov, M. A. Putyato, A. K. Gutakovskii, A. S. Kozhukhov, B. R. Semyagin, V. V. Preobrazhenskii, and T. S. Shamirzaev, *Formation and Crystal Structure of GaSb/GaP Quantum Dots*, Bulletin of the Russian Academy of Sciences. Physics, Vol. **80**, 17 (2016).

[81] L. Desplanque, C. Coinon, D. Troadec, P. Ruterana, G. Patriarche, L. Bonato, D. Bimberg, and X. Wallart, *Morphology and valence band offset of GaSb quantum dots grown on GaP(001) and their evolution upon capping*, Nanotechnology **28**, 225601 (2017).

[82] L. Bonato, I. F. Arikan, L. Desplanque, C. Coinon, X. Wallart, Y. Wang, P. Ruterana, and D. Bimberg, *Hole localization energy of 1.18 eV in GaSb quantum dots embedded in GaP*, Phys. Stat. Sol. B, 1 (2016).

[83] M. T. Otten, *High-angle annular dark-field imaging on a tem/stem system*, J. Elec. Micr. Tech. **17**, 221 (1991).

[84] G. Stracke, A. Glacki, T. Nowozin, L. Bonato, S. Rodt, C. Prohl, A. Lenz, H. Eisele, A. Schliwa, A. Strittmatter, U. W. Pohl, and D. Bimberg, *Growth of $In_{0.25}Ga_{0.75}As$ quantum dots on GaP utilizing a GaAs interlayer*, Appl. Phys. Lett. **101**, 223110 (2012).

[85] F. Heinrichsdorff, A. Krost, M. Grundmann, D. Bimberg, F. Bertram, J. Christen, A. Kosogov, and P. Werner, *Self organization phenomena of InGaAs/GaAs quantum dots grown by metalorganic chemical vapour deposition*, J. Cryst. Growth **170**, 568 (1997).

[86] K. Pötschke, L.Müller-Kirsch, R. Heitz, R.L. Sellin, U.W. Pohl, D. Bimberg, N. Zakharov, and P. Werner, *Ripening of self-organized InAs quantum dots*, Physica E **21**, 606-610 (2004).

[87] F. Heinrichsdorff, A. Krost, D. Bimberg, A. O. Kosogov, and P. Werner, *Self organized defect free InAs/GaAs and InAs/InGaAs/GaAs quantum dots with high lateral density grown by MOCVD*, Appl. Surf. Sci. **725**, 123 (1998).

[88] S. Dadgostar, J. Schmidtbauer, T. Boeck, A. Torres, O. Martinez, J. Jimenez, J. W. Tomm, A. Mogilatenko, W. T. Masselink, and F. Hatami, *GaAs/GaP quantum dots: Ensemble of direct and indirect heterostructures with room temperature optical emission*, Appl. Phys. Lett. **108**, 102103 (2016).

[89] M. Rosini, P. Kratzer, and R. Magri, *In adatom diffusion on $In_xGa_{1-x}As$/GaAs(001): effects of strain, reconstruction and composition*, J. Phys.: Condens. Matter **21**, 355007 (2009).

[90] Y. Q. Wang, Z. L. Wang, T. Brown, A. Brown, and G. May, *Thermodynamic analysis of anion exchange during heteroepitaxy*, J. Cryst. Growth **242**, 5 (2002).

[91] N. Kakuda, S. Tsukamoto, A. Ishii, K. Fujiwara, T. Ebisuzaki, K. Yamaguchi, and Y. Arakawa, *Surface reconstructions on Sb-irradiated GaAs(001) formed by molecular beam epitaxy*, Microel. J. **38**, 620 (2007).

[92] D. Leonard, K. Pond, and P. M. Petroff, *Critical layer thickness for self-assembled InAs islands on GaAs*, Phys. Rev. B **50**, 11687 (1994).

[93] W. A. Jesser and D. Kuhlmann-Wilsdorf, *On the interfacial energy and elastic strain of epitaxial overgrowth in parallel alignment on single crystal substrates*, Phys. Stat. Sol. B **19**, 95 (1967).

[94] A. Madhukar, Q. Xie, P. Chen, and A. Konkar, *Nature of strained InAs three dimensional island formation and distribution on GaAs(100)*, Appl. Phys. Lett. **64**, 2727 (1994).

[95] M. Copel, M. C. Reuter, E. Kaxiras, and R. M. Tromp, *Surfactants in epitaxial growth*, Phys. Rev. Lett. **63**, 6 (1989).

[96] C. M. Fetzer, R. T. Lee, J. K. Schurtleff, G. B. Stringfellow, S. M. Lee, and T. Y. Seong, *The use of a surfactant (Sb) to induce triple period ordering in GaInP*, Appl. Phys. Lett. **76**, 1440 (2000).

[97] P. Blood and J. W. Orton, *The Electrical Characterization of Semiconductors: Majority Carriers and Electron States*, Academic London (1992).

[98] D. Guimard, S. Tsukamoto, M. Nishioka, and Y. Arakawa, *1.55 μm emission from InAs/GaAs quantum dots grown by metal organic chemical vapor deposition via antimony incorporation*, Appl. Phys. Lett. **89**, 083116 (2006).

[99] Y. I. Mazur, V. G. Dorogan, G. J. Salamo, G. G. Tarasov, B. L. Liang, C. J. Reyner, K. Nunna, and D. L. Huffaker, *Coexistence of type-I and type-II band alignments in antimony-incorporated InAsSb quantum dot nanostructures*, Appl. Phys. Lett. **100**, 033102 (2012).

[100] D. Guimard, M. Nishioka, S. Tsukamoto, and Y. Arakawa, *Effect of antimony on the density of InAs/Sb:GaAs(100) quantum dots grown by metal-organic chemical-vapor deposition*, J. Cryst. Growth. **298**, 548 (2007).

[101] A. Portavoce, I. Berbezier, and A. Ronda, *Sb-surfactant-mediated growth of Si and Ge nanostructures*, Phys. Rev. B **69**, 155416 (2004).

[102] Y. Sun, S.F. Cheng, G. Chen, R.L. Woo, and R.F. Hicks, *The effect of antimony in the growth of indium arsenide quantum dots in gallium arsenide (001)*, J. Appl. Phys. **97**, 053503 (2005).

[103] K. Yamaguchi and T. Kanto, *Self-assembled InAs quantum dots on GaSb/GaAs(001) layers by molecular beam epitaxy*, J. Cryst. Growth **275**, 2269 (2005).

[104] A. Lenz, R.Timm, H. Eisele, C.Hennig, S. K. Becker, R. L. Sellin, U. W. Pohl, D. Bimberg, and M. Dähne, *Reversed truncated cone composition distribution of $In_{0.8}Ga_{0.2}As$ quantum dots overgrown by an $In_{0.1}Ga_{0.9}As$ layer in a GaAs matrix*, Appl. Phys. Lett. **81**, 5150 (2002).

[105] A. Marent, M. Geller, A. Schliwa, D. Feise, K. Pötschke, D. Bimberg, N. Akcay, and N. Oncan, *10^6 years extrapolated hole storage time in GaSb/AlAs quantum dots*, Appl. Phys. Lett. **91**, 242109 (2007).

[106] M. Di Ventra, M. Peressi, and A. Baldereschi, *Chemical and structural contributions to the valence-band offset at GaP/GaAs heterojunctions*, Phys. Rev. B **54**, 5691 (1996).

[107] L. Bonato, E. M. Sala, G. Stracke, T. Nowozin, A. Strittmatter, M. N. Ajour, K. Daqrouq, and D. Bimberg, *230 s room-temperature storage time and 1.14 eV hole localization energy in $In_{0.5}Ga_{0.5}As$ quantum dots on a GaAs interlayer in GaP with an AlP barrier*, Appl. Phys. Lett. **106**, 042102 (2015).

[108] T. Nowozin, D. Bimberg, K. Daqrouq, M. N. Ajour and M. Awedh, *Materials for Future Quantum Dot-Based Memories*, J. Nanomat. **2013**, 1 (2013).

[109] T. Nowozin, D. Bimberg, K. Daqrouq, M. N. Ajour, and M. Awedh, *Materials for future quantum dot-based memories*, J. Nanomat., ID 215613, Hindawi Publishing Corporation (2013).

[110] J. Starkiewicz and J. W. Allen, *Injection electroluminescence at p-n junctions in Zinc-doped Gallium Phosphide*, J. Phys. Chem. Solids, **23**, 881-884 (1962).

[111] L. L. Chang and G. L. Pearson, *Diffusion Mechanism of Zn in GaAs and GaP Based on Isoconcentration Diffusion Experiments*, J. Appl. Phys. **35**, 6 (1964).

[112] H. W. Allison, *Solubility and Diffusion of Zinc in Gallium Phosphide*, J. Appl. Phys. **34**, 1 (1963).

[113] X.-L. Wang, A. Wakahara, A. Sakaki, *Si and Zn doping of GaP grown by OMVPE using tertiarybutylphosphine*, J. Cryst. Growth, **158**, 49 (1996).

[114] K. Kaneko, M. Dosen and N. Watanabe, *Efficient Red LEDs of GaP by Vapor Phase Doping of Zinc*, Jpn. J. Appl. Phys. **12**, 1732 (1973).

[115] K. A. Bertness, S. R. Kurtz, D. J. Friedman, A. E. Kibbler, C. Kramer, and J. M. Olson, *29.5 %-efficient GaInP/GaAs tandem solar cells*, Appl. Phys. Lett. **65**, 989 (1994).

[116] H. Bracht and S. Brotzmann, *Zinc diffusion in gallium arsenide and the properties of gallium interstitials*, Phys. Rev. B **71**, 115216 (2005).

[117] K. A. Bertness, S. R. Kurtz, D. J. Friedman, A. E. Kibbler, C. Kramer, and J. M. Olson, *29.5 %-efficient GaInP/GaAs tandem solar cells*, Appl. Phys. Lett. **65**, 989 (1994).

[118] S. G. Ayling, A. C. Bryce, I. Gontijo, J. H. Marsh and J. S. Roberts, *A comparison of carbon and zinc doping in GaAs/AlGaAs lasers bandgap-tuned by impurity-free vacancy disordering*, Semicond. Sci. Technol. **9**, 2149 (1994).

[119] C. L. Yicheng, T. S. Kalkur, and C. A. Paz de Araujo, *Rapid thermal diffusion of zinc into GaAs.*, J. Elec. Mat. **19**, 1 (1990).

[120] O. Madelung, U. Rössler, and M. Schulz, *Gallium Phosphide (GaP), energies and capture cross sections of hole traps*, in: Landolt-Börnstein - Group III Condensed Matter. Vol. 41D. Springer Materials (2016).

[121] T. F. Kuech, M. A. Tischler, P.-J. Wang, G. Scilla, R. Potemski, and F. Cardone, *Controlled carbon doping of GaAs by metalorganic vapor phase epitaxy*, Appl. Phys. Lett. **53**, 1317 (1988).

[122] N. Kobayashi, T. Makimoto, and Y. Horikoshi, *Abrupt p-type doping profile of carbon atomic layer doped GaAs grown by flow-rate modulation epitaxy*, Appl. Phys. Lett. **50**, 1435 (1987).

[123] B. T. Cunningham, L. J. Guido, J. E. Baker, J. S. Major, N. Holonyak, and G. E. Stillman, *Carbon diffusion in undoped, n-type, and p-type GaAs*, Appl. Phys. Lett. **55**, 687 (1989).

[124] D. P. Bortfeld, B. J. Curtis, and H. Meier, *Electrical Properties of carbon-Doped Gallium Phosphide*, J. Appl. Phys. **43**, 3 (1972).

[125] S. Bhunia, K. Uchida, S. Nozaki, N. Sugiyama, M. Furiya, and H. Morisak, *Metal organic vapor phase epitaxial growth of heavily carbon-doped GaAs using a dopant source of CCl_3Br and quantitative analysis of the compensation mechanism in the epilayers*, J. Appl. Phys. **93**, 1613 (2003).

[126] K. Uchida, S. Bhunia, N. Sugiyama, M. Furiya, M. Katoh, S. Katoh, S. Nozaki, H. Morisaki, *Heavy carbon doping of GaAs by MOVPE using a new dopant source $CBrCl_3$ and characterization of the epilayers*, J. Cryst. Growth **248**, 248 (2003).

[127] K. Tateno, Y. Kohama, and C. Amano, *Carbon doping and etching effects of CBr_4 during metalorganic chemical vapor deposition of GaAs and AlAs*, J. Cryst. Growth **172**, 5 (1997).

[128] P. M. Enquist, *p-type doping limit of carbon in organometallic vapor phase epitaxial growth of GaAs using carbon tetrachloride*, Appl. Phys. Lett. **57**, 2348 (1990).

[129] J.-S. Lee, I. Kim, B.-D. Choe, and W. G. Jeong, *Carbon doping and growth rate reduction by CCl_4 during metalorganic chemical- vapor deposition of GaAs*, J. Appl. Phys. **76**, 5079 (1994).

[130] L. J. van der Pauw, *A method of measuring specific resistivity and Hall effect of discs of arbitrary shape*, in Phil. Tech. Rev., **20**, 220 (1958).

[131] E. Conwell and V. F. Weisskopf, *Theory of impurity scattering in semiconductors*, Phys. Rev. **77**, 388 (1950).

[132] T. Iizuka, *Investigation of Microprecipitates in Highly Te- Doped GaAs Crystals*, Jpn. J. Appl. Phys. **7**, 490 (1968).

[133] T. Iizuka, *Etching Studies of Impurity Precipitates in Pulled GaP Crystals*, J. Electrochem. Soc. **118**, 1190 (1971).

[134] J. Bourgoin and M. Lanoo, *Point defects in semiconductors II - Experimental aspects*, published from M. Cardona, P. Fulde, and H.-J. Quisser, Berlin, Heidelberg, New York: Springer, 1983, ISBN: 3-540-11515-3.

[135] P. Omling, L. Samuelson, and H. G. Grimmeis, *Deep-level transient spectroscopy evaluation of nonexponential transients in semiconductor alloys*, J. Appl. Phys. **54**, 5117 (1983).

[136] D. S. Day, M. Y. Tsai, B. G. Streetman, and D. v. Lang, *Deep level transient spectroscopy: System effects and data analysis*, J. Appl. Phys. **50**, 5093 (1979).

[137] S. M. Sze, K. K. Ng, *Physics of Semiconductors Devices*, 3rd edn. Wiley, New York (2006).

[138] M. Geller, C. Kapteyn, L. Müller-Kirsch, R. Heitz, and D. Bimberg, *450 meV hole localization in GaSb/GaAs quantum dots*, Appl. Phys. Lett. **82**, 2706 (2003).

[139] W. Mönch, *On the band-structure lineup at Schottky contacts and semiconductor heterostructures*, Mater. Sci. Semicond. Processing **28**, 2 (2014).

[140] W. Mönch, *Electronic Properties of Semiconductor Interfaces*, Springer, Berlin (2004). Sec. **5.6** and **6.2**.

[141] S. J. Xu, X. C. Wang, S. J. Chua, C. H. Wang, W. J. Fan, J. Jiang, and X. G. Xie, *Effects of rapid thermal annealing on structure and luminescence of self-assembled InAs/GaAs quantum dots*, Appl. Phys. Lett. **72**, 25 (1998).

[142] S. Malik, C. Roberts, and R. Murray, *Tuning self-assembled InAs quantum dots by rapid thermal annealing*, Appl. Phys. Lett. **71**, 1987 (1997).

[143] D. R. Wight, *Intrinsic and extrinsic edge luminescence in epitaxial GaP*, J. Phys. C (Proc. Phys. Soc.) **1**, 1759 (1968).

[144] P. J. Dean, C. H. Henry, and C. J. Frosch, *Infrared Donor-Acceptor Pair Spectra Involving the Deep Oxigen Donor in Gallium Phosphide*, Phys. Rev. **168**, 3 (1968).

[145] M. A. Herman, D. Bimberg, and J. Christen, *Heterointerfaces in quantum wells and epitaxial growth processes: Evaluation by luminescence techniques*, J. Appl. Phys. **70**, R1 (1991).

[146] J. A. Prieto, G. Armelles, M.-E. Pistol, P. Castrillo, J. P. Silveira, and F. Briones, *Optical studies of GaAs quantum wells strained to GaP*, Appl. Phys. Lett. **70**, 25 (1997).

[147] C. Robert, M. O. Nestoklon, K. Pereira da Silva, L. Pedesseau, C. Cornet, M. I. Alonso, A. R. Goñi, P. Turban, J.- M. Jancu, J. Even, and O. Durand, *Strain-induced fundamental optical transition in (In,Ga)As/GaP quantum dots*, Appl. Phys. Lett. **104**, 011908 (2014).

[148] L. Brusaferri, S. Sanguinetti, E. Grilli, M. Guzzi, A. Bignazzi, F. Bogani, L. Carraresi, M. Colocci, A. Bosacchi, P. Frigeri, and S. Franchi, *Thermally activated carrier transfer and luminescence line shape in self-organized InAs quantum dots* Appl. Phys. Lett. **69**, 3354 (1996).

[149] R. Heitz, I. Mukhametzhanov, A. Hoffmann, and D. Bimberg, *Temperature Dependent Optical Properties of Self-Organized InAs/GaAs Quantum Dots*, J. Electron. Mater. **28**, 520 (1999).

[150] F. Hatami, N. N. Ledentsov, M. Grundmann, J. Böhrer, F. Heinrichsdorff, M. Beer, D. Bimberg, S. S. Ruvimov, P. Werner, U. Gösele, J. Heydenreich, S. V. Ivanov, B. Ya Meltser, P.S. Kop'ev, and Zh. I. Alferov, *Radiative recombination in type-II GaSb/GaAs quantum dots*, Appl. Phys. Lett. **67**, 31 (1995).

[151] Y. Varshni, *Temperature dependence of the energy gap in semiconductors*, Physica **34**, 149 (1967).

[152] S. Sanguinetti, M. Henini, M. Grassi Alessi, M. Capizzi, P. Frigeri and S. Franchi, *Carrier thermal escape and retrapping in self-assembled quantum dots*, Phys. Rev. B **60**, 11 (1999).

[153] R. Zimmermann and E. Runge, *Excitons in narrow quantum wells: disorder localization and luminescence kinetics*, Phys. Stat. Sol. (a), **164**, 511 (1997).

[154] L. Müller-Kirsch, *Metallorganische Gasphasenepitaxie und Charakterisierung von antimonhaltige Quantenpunkten*, Berlin Studies in Solid State Physics (2002), ISBN 3-89685-398-8.

[155] O. G. Lyublinskaya, V. A. Solov'ev, A. N. Semenov, B. Ya. Meltser, Ya. V. Terent'ev, L. A. Prokopova, A. A. Toropov, A. A. Sitnikova, O. V. Rykhova, S. V. Ivanov, K. Thonke, and R. Sauer, *Temperature-dependent photoluminescence from type-II InSb/InAs quantum dots*, J. Appl. Phys. **99**, 093517 (2006).

[156] R. Heitz, M. Veit, N. N. Ledenstov, A. Hoffmann, D. Bimberg, V. M. Ustinov, P. S. Kop'ev, and Zh. Alferov, *Energy relaxation by multiphonon processes in InAs/GaAs quantum dots*, Phys. Rev. B **56**, 16 (1997).

[157] J. H. Davies, *The Physics of Low-Dimensional Semiconductors*, Cambridge University Press (2006), ISBN 0-521-48148-1.

[158] N. N. Ledentsov, J. Böhrer, M. Beer, F. Heinrichsdorff, M. Grundmann, D. Bimberg, S. V. Ivanov, B. Ya. Meltser, S. V. Shaposhnikov, I- N. Yassievich, N. N. Faleev, P. S. Kop'ev, and Zh. I. Alferov, *Radiative states in type-II GaSb/GaAs quantum wells*, Phys. Rev. B **52**, 14058 (1995).

[159] K. Suzuki, R. A. Hogg, and Y. Arakawa, *Structural and optical properties of type II GaSb/GaAs self-assembled quantum dots grown by molecular beam epitaxy*, J. Appl. Phys. **85**, 12 (1999).

[160] J. He, C. J. Reyner, B. L. Liang. K. Nunna, D. L. Huffaker, N. Pavarelli, K. Gradkowski, T. J. Ochalski, G. Huyet, V. G. Dorogan, Yu. I. Mazur, and G. J. Salamo, *Band Alignment Tailoring of $InAs_{1-x}Sb_x$/GaAs Quantum Dots: Control of Type I to Type II Transition*, Nano Lett. **10**, 3052 (2010).

[161] P. D. Hodgson, R. J. Young, M. Ahmad Kamarudin, P. J. Carrington, A. Krier, Q. D. Zhuang, E. P. Smakman, P. M. Koenraad, and M. Hayne, *Blueshifts of the emission energy in type-II quantum dot and quantum ring nanostructures*, J. Appl. Phys. **114**, 073519 (2013).

[162] D. A. Álvarez, B. Alén, J. M. García, and J. M. Ripalda, *Optical investigation of type II self-assembled quantum dots*, Appl. Phys. Lett. **91**, 263103 (2007).

[163] E. F. Schubert, *Light-Emitting Diodes*, Cambridge University Press (2018), ISBN 978-0-9863826-6-6.

[164] K. Gradkowski, T. J. Ochalski, N. Pavarelli, H. Y. Liu, J. Tatebayashi, D. P.Williams, D. J. Mowbray, G. Huyet, and D. L. Huffaker, *Coulomb-induced emission dynamics and self-consistent calculations of type-II Sb-containing quantum dot systems*, Phys. Rev. B **85**, 035432 (2012).

[165] P. Klenovský, P. Steindl, and D. Geffroy, *Excitonic structure and pumping power dependent emission blue-shift of type-II quantum dots*, Sci. Rep. **7**, 45568 (2017).

[166] M. Hayne, O. Razinkova, S. Bersier, R. Heitz, L. Muller-Kirsch, M. Geller, D. Bimberg, and V. V. Moshchalkov, *Optically induced charging effects in self-assembled GaSb/GaAs quantum dots*, Phys. Rev. B **70**, 081302 (2004).

[167] K. Gradkowski, T. J. Ochalski, D. P. Williams, S. B. Healy, J. Tatebayashi, G. Balakrishnan, E. P. O'Reilly, G. Huyet, and D. L. Huffaker, *Coulomb effects in type-II Ga(As)Sb quantum dots*, Phys. Status Solidi B **246**, 752 (2009).

[168] M. Grundmann, N. N. Ledentsov, O. Stier, D. Bimberg, V. M. Ustinov, P. S. Kop'ev, and Zh. I. Alferov, *Excited states in self-organized InAs/GaAs quantum dots: Theory and experiment*, Appl. Phys. Lett. **68**, 979 (1996).

[169] L. Müller-Kirsch, A. Schliwa, O. Stier, R. Heitz, H. Kirmse, W. Neumann, and D. Bimberg, *State Filling in Type II Qauntum Dots*, Phys. Stat. Sol. B **224**, 349 (2001).

[170] W. Heitler, *The Quantum Theory of Radiation*, Oxford Univ. Press (1954).

[171] F. Hatami, M. Grundmann, N. N. Ledentsov, F. Heinrichsdorff, R. Heitz, J. Böhrer, D. Bimberg, S. S. Ruvimov, P. Werner, V. M. Ustinov, P. S. Kop'ev, and Zh. I. Alferov, *Carrier dynamics in type-II GaSb/GaAs quantum dots*, Phys. Rev. B **57**, 4635 (1998).

[172] K. L. Chang, C. K. Lee, J. W. Hsu, H. F. Hsieh and H.C. Shih, *The etching behavior of GaP in aqua regia solutions*, J. Appl. Electrochem. **35**, 77 (2005).

[173] T. Ohmi, T. Imaoka, I. Sugiyama, T. Kezuka, *Metallic Impurities Segregation at the Interface Between Si Wafer and Liquid during Wet Cleaning*, J. Electr. Soc. **139**, 3317 (1992).

Acknowledgments

First and foremost I would like to express my deep gratitude to Prof. Dr. Dieter Bimberg, my thesis supervisor, for giving me the possibility to work in his research group at the TU Berlin, and for playing an important role in my professional growth.

Also, I would like to thank the other members of the dissertation commitee: Prof. Dr. Xavier Wallart for reviewing my thesis and Prof. Dr. Holger Stark for heading the commitee.

My special thanks are for Prof. Dr. André Strittmatter and Dr. Gernot Stracke for introducing me to the MOCVD growth technique, and for providing me a fundamental guidance throughout the years of my PhD.

I am grateful to the laboratory technicians Kathrin Schatke and René Linke for the valuable assistance during the laboratory maintenance. I would like to extend my thank to all members of the AG Bimberg for their cooperation and good work environment, in particular to Dr. Gunter Larisch for the very pleasant atmosphere in the office. Moreover, many thanks to Dr. Leo Bonato and Firat Arikan for the scientific collaboration, fruitful conversations and mutual support. I also wish to acknowledge the help provided by the secretary Roswitha Koskinas with all the bureaucratic procedures.

I thank the group of Prof. Dr. Jürgen Christen of the University of Magdeburg for carrying out TEM-CL investigations on InGaSb/GaP QD samples. Moreover, I am very thankful to Dr. Felix Nippert, Dr. Gordon Callsen, and Dr. Thomas Kure (AG Hoffmann, TU Berlin) for TRPL measurements and to Sören Selve and Dr. Tore Niermann (AG Lehmann, Institute of Optic and Atomic Physics, TU Berlin) for the TEM investigations.

I am also thankful to Dr. Petr Klenovský and Petr Steindl for stimulating discussions about the InGaSb/GaP QDs and the welcoming atmosphere during my short stay in Brno.

Last but not least, I would like to thank my family for having given me roots to know where home is and wings to fly away.